1-1-2012

Experimental And Numerical Study Of Single And Multiple Imapcts Of Angular particles On Ductile Metals

Mahdi Takaffoli
Ryerson University

EXPERIMENTAL AND NUMERICAL STUDY OF SINGLE AND MULTIPLE IMPACTS OF ANGULAR PARTICLES ON DUCTILE METALS

by

Mahdi Takaffoli

MSc, 2007, Tehran University, Iran

BSc, 2005, Iran University of Science and Technology, Iran

A dissertation

presented to Ryerson University

in partial fulfillment of the

requirements for the degree of

Doctor of Philosophy

in the program of

Mechanical and Industrial Engineering

Toronto, Ontario, Canada, 2012

I hereby declare that I am the sole author of this dissertation. This is a true copy of the dissertation, including any required final revisions, as accepted by my examiners.

I authorize Ryerson University to lend this dissertation to other institutions or individuals for the purpose of scholarly research.

I further authorize Ryerson University to reproduce this dissertation by photocopying or by other means, in total or in part, at the request of other institutions or individuals for the purpose of scholarly research.

I understand that my dissertation may be made electronically available to the public.

EXPERIMENTAL AND NUMERICAL STUDY OF SINGLE AND MULTIPLE IMPACTS OF ANGULAR PARTICLES ON DUCTILE METALS

Mahdi Takaffoli

2012

Ph.D.

Department of Mechanical and Industrial Engineering
Ryerson University

Abstract

Solid particle erosion occurs when small high speed particles impact surfaces. It can be either destructive such as in the erosion of oil pipelines by corrosion byproducts, or constructive such as in abrasive jet machining processes.

Two dimensional finite element (FE) models of single rhomboid particles impact on a copper target were developed using two different techniques to deal with the problem of element distortion: (i) element deletion, and (ii) remeshing. It was found that the chip formation and the material pile-up, two phenomena that cannot be simulated using a previously developed rigid-plastic model, could be simulated using the FE models, resulting in a good agreement with experiments performed using a gas gun. However, remeshing in conjunction with a failure model caused numerical instabilities. The element deletion approach also induced errors in mass loss due to the removal of distorted elements.

To address the limitations of the FE approach, smoothed particle hydrodynamics (SPH) which can better accommodate large deformations, was used in the simulation of the impact of single rhomboid particles on an aluminum alloy target. With appropriate constitutive and failure parameters, SPH was demonstrated to be suitable for simulating all of the relevant damage phenomena observed during impact experiments.

A new methodology was developed for generating realistic three dimensional particle geometries based on measurements of the size and shape parameter distributions for a sample of

150 μm nominal diameter angular aluminum oxide powder. The FE models of these generated particles were implemented in a SPH/FE model to simulate non-overlapping particle impacts. It was shown that the simulated particles produced distributions of crater and crater lip dimensions that agreed well with those measured from particle blasting experiments.

Finally, a numerical model for simulating overlapping impacts of angular particles was developed and compared to experimental multi-particle erosion tests, with good agreement. An investigation of the simulated trajectory of the impacting particles revealed various erosion mechanisms such as the micromachining of chips, the ploughing of craters, and the formation, forging and knocking off crater lips which were consistent with previously noted ductile solid particle erosion mechanisms in the literature.

Acknowledgements

I would like to express my very great appreciation to my supervisor, Professor Marcello Papini whose guidance, expertise and encouragement was greatly helpful to me throughout my PhD research. All the meetings and discussions I had with you left me with passion and great ideas to address the challenges of my dissertation. I will forever be thankful to you for what I have learned in the past five years.

I would also like to thank my supervisory committee, Dr. Daolun Chen and Dr. Donatus Oguamanam, for their suggestions during my Ph.D. candidacy exam. My grateful thanks are also extended to Professor Khaled Sennah and Professor William Altenhof for agreeing to be on my examination committee.

I also wish to acknowledge the technical staff of our department, Misters Joseph Amankrah, Alan Machin, Devin Ostrom, Qiang Li and Chao Ma whose support and assistance were greatly helpful to me throughout my dissertation.

Very special thanks to the Natural Sciences and Engineering Council of Canada (NSERC), the Canada Research Chairs Program, the Ontario Ministry of Training, Colleges and Universities, the Ryerson University School of Graduate Studies and the Department of Mechanical and Industrial Engineering for their financial support.

Finally my warmest gratitude to my mother, father and three sisters for all the caring and support provided to me over the phone or in person when I visited home during the time of my PhD. This dissertation is dedicated to them.

Table of Contents

Nomenclature

Area	In-plane area of a particle
A	Particle angularity (**Fig. 2-1**)
B	Constant in Eq. 2-1
BHN	Brinell hardness number
c	Constant in Eq. 2-1
C_p	Specific heat
CV	Crater volume
D	Constant in Eq. 3-9
D_1-D_5	Constants in Eq. 3-11
D_{circular}	Circular diameter of a particle
d_{max}	Maximum depth (**Fig. 2-8**)
E	Modulus of elasticity
F	Damage parameter in Eq. 3-10
FS	Tensile failure strain
f	Field function
$< f >$	Integral approximation of f
G	Shear modulus
Hv	Vickers hardness number
h	Particle length (**Fig. 2-1**)
h_{lip}	Lip height (**Fig. 2-8**)
K	Bulk modulus
$2l$	Radius of influence domain in Eq. 3-1
M	Constant in Eq. 2-1
m_j	Mass of SPH particle j
N	Number of particles in the influence domain in Eq. 3-2
n	Constant in Eq. 2-1
P	Constant in Eq. 3-9
Perimeter	Perimeter of a particle
p	hydrostatic pressure

p_d	Dynamic hardness
R	Roundness of a particle
S_1	Slope of the shock velocity versus material velocity curve
T	Temperature
T_{inst}	Instantaneous temperature
T_{melt}	Melting temperature
T_{ref}	Reference temperature in Eq. 2-3
v_i	Incident velocity
v_r	Rebound velocity
v_{ij}	Component of relative velocity between SPH particle *i* and *j* in Eq. 3-5
v_{sound}	Bulk speed of sound in the material
$\mathbf{x}'$	Position vector of the points in the influence domain in Eq. 3-1
$\mathbf{x}$	Coordinates of a location in the influence domain in Eq. 3-1
W	Smoothing kernel function
Wp	Plastic work
w	Particle thickness (**Fig. 2-1)**

α_i	Angle of incidence
α_r	Angle of rebound
ε_{eff}^{P}	Effective plastic strain
$\dot{\varepsilon}_{eff}^{P}$	Effective plastic strain rate
$\dot{\varepsilon}_0$	Reference strain rate in Eq. 2-2
$\dot{\varepsilon}^*$	Nondimensional strain rate in Eq. 2-2
$\dot{\varepsilon}_{eff}$	Effective total strain rate
ε^{f}	Failure strain
γ_0	Gruneisen constant
Ω	Domain of integration in Eq. 3-1
μ	Rate of density change in Eqs 3-7 and 3-8

ν	Poisson's ratio
θ_i	Particle orientation (**Fig. 2-1**)
ρ	Density
ρ_i	Initial density in Eqs 3-7 and 3-8
ρ_{inst}	Instantaneous density in Eqs 3-7 and 3-8
σ_0	Constant in Eq. 2-1
σ_Y	Flow strength
σ_{static}	Static yield stress
σ_i	Components of stress tensor for SPH particle *i* in Eqs. 3-4 and 3-5
σ_{eff}	Effective stress

List of Tables

List of Figures

List of Appendices

Chapter 1 Introduction

This chapter presents an introduction to solid particle erosion phenomena, a critical review of the literature regarding erosion modeling, and the objectives of the dissertation.

1.1 Background and motivation

Solid particle erosion has been defined as “an abrasive wear process in which the repeated impact of small particles entrained in a moving fluid against a surface results in the removal of material from that surface” [1]. Solid particle erosion can cause significant damage to surfaces which are exposed to high velocity particles, usually entrained in a fluid flow. Such situations arise in various industries such as the oil and gas production industry, aeronautical, power station, etc. [2–11]. It has been estimated that in power stations, solid particle erosion costs American utilities over $150 million annually due to reduction of efficiency, heat loss and maintenance and repair costs [12].

The industrial significance of the study of solid particle erosion phenomena is not limited to its destructive effects. Material removal due to solid particle impact can also be desirable, as in, for example, blast cleaning [13], [14], abrasive water jet machining [15] and abrasive jet machining [16], [17]. Abrasive jet micromachining, in particular has been of recent interest as a non-traditional microfabrication platform to micromachine features in various materials used, for example, in microfluidics and micro-electro-mechanical-systems (MEMS) [18], [19]. In this process, small solid aluminum oxide particles are accelerated to high speeds by an air jet, and made to impact masked target materials such as glass, silicon, and polymers. A significant effort has thus been expended towards the development of predictive equations capable of determining the erosion rate of materials, as a function of process and material parameters. In these equations, the erosion rate, i.e. the mass or volume of target material removed per mass of particles impacting the surface, is correlated with process parameters such as particle impact angle, velocity, shape, size and hardness, and target variables such as hardness, tensile strength or yield strength. Generally, predictive equations are developed for two types of solid particle erosion: brittle erosion and ductile erosion. In brittle erosion, the material is removed by crack formation and chipping mechanisms, whereas in ductile erosion, cutting and ploughing due to plastic deformation are responsible for the material loss. The difference between these two erosion behaviors can be recognized from the variation of erosion rate with impact angle. For ductile materials, the maximum target weight loss occurs when the jet is inclined to the surface, while for brittle materials it occurs at perpendicular impact [20]. This dissertation focused on the modeling of ductile erosion phenomena.

Although solid particle erosion phenomena are present in many different industries, many aspects remain poorly understood due to the complexity of the erosion process. For this reason analytical and computational models for erosion are favorable, since they can be used to study the effect of each parameter in erosion separately. However, as will be seen in the literature review in **Section 1.3**, existing ductile erosion models that have been presented in the literature suffer from a number of shortcomings which can be summarized as follows:

a. Most existing solid particle erosion models are highly simplified, neglecting the pile-up of material at the edge of the individual impact craters, and the effects of strain rate, strain hardening, particle shape, and thermal softening on the erosive response of the material.

b. Previous models were mostly developed for spherical particles. However, practical applications of solid particle erosion mostly involve highly irregularly shaped powders.

c. Particles with uniform size and shape have usually been implemented in existing models and the variations of size and shape in a sample of particles has generally been ignored.

d. Previous finite element simulations of multi-particle impacts have used idealized particles, and the ability of the models to reproduce common experimentally observed material removal mechanisms has not been discussed.

1.2 Objectives

In order to overcome the shortcomings of previous models, and identify the fundamental mechanisms of material removal, this dissertation focused on modeling ductile erosive systems using computational methods. The main objective of the research was to develop a three-dimensional computational model for the prediction of the solid particle erosion of ductile materials impacted by a jet of angular particles.

The following secondary objectives were identified to build towards the main:

(i) Evaluation of existing numerical techniques for the simulation of the large scale deformation events such as those occurring in solid particle erosion. Particular attention was paid to methods that avoid element distortion and tangling.

(ii) Development of numerical models for the single impact of two-dimensional idealized rhomboid particles and identification of suitable constitutive target models.

(iii) Development of a methodology for generating modeled samples of alumina particles which match measured size and shape distribution of actual erodent powders, and that, when implemented in numerical models, result in crater dimension distributions that match those that were measured.

(iv) Development of models for studying the cooperative effect of multiple overlapping impacts on the resulting material removal from the surface.

1.3 Literature review

In this section, a brief literature review of particle impact modeling is presented. First, single particle impact modeling is reviewed in **Section 1.3.1**. Then, studies of the dependency of erosion on particle shape, and previous attempts to generate representative models of irregularly shape particles are reviewed in **Section 1.3.2**. In **Section 1.3.3**, numerical models of particle erosion are reviewed, and finally, in **Section 1.3.4**, previously hypothesized mechanisms of material removal are described.

1.3.1 Modeling single particle impact of angular particles

Although most solid particle erosion phenomena involve the repeated impacts of a jet of small particles, the study of the impact of a single particle can be useful for understanding the mechanisms of material deformation and removal, e.g. ploughing, cutting, cracking, etc., and their dependency on impact parameters such as impact velocity, impact angle and particle shape [1], [21–23]. A single particle impact analysis can also provide an initial validation of the applicability, robustness and accuracy of the material models and numerical techniques that can be used [24] to analyze erosion due to jets of particles.

Despite the presence of granular particles in most practical solid particle erosion processes, relatively few experimental and analytical studies involving well controlled single angular particle impacts exist. Experiments by Hutchings with square particles on low-carbon steel identified two classes of impacts, resulting from different combinations of the impact angle and initial orientation of the particle with respect to the target [25]. The most probable impact involved forward rotation of the particle during impact, and resulted in target material extruded to the rim of the impact crater but no material removal. A backwards rotation of the particle with a pure machining and removal of a chip of material was also observed, but much less often [25]. These observations were also confirmed by Papini and Dhar [26], who also reported another type of material removal when conducting experiments with much sharper particles. The leading edge of these sharp particles were sometimes found to tunnel below the surface, leading to the prying off a chip of material before completion of the cutting process, forming a crater with a jagged edge.

The difficulty in independently controlling the abundance of parameters affecting solid particle erosion using experiments necessitates the development of numerical erosion models. However, this is challenging for the following reasons:

(a) Particle impact occurs in a short period of time, resulting in high strain rate deformation of the target under an adiabatic process.

(b) The target material is highly strained by the impacting particle.

(c) Depending on the shape of the particle and its initial orientation with respect to the target, different impact and material removal mechanisms are expected to occur.

Overcoming these challenges requires the implementation of material models which can account for the strain rate and temperature dependencies, and the implementing an appropriate failure criterion. In addition, the large target material deformations resulting from impact loading impose nonlinearity to the problem, thus requiring a careful consideration of the numerical discretization technique and solution algorithm to be used.

The most commonly used single particle erosion model for ductile erosive systems is based on rigid-plastic theory, which assumes a rigid particle impacting a perfectly plastic target. The size of the impact crater is evaluated based on the particle trajectory during impact process calculated by solving the equations of motion of the particle. In the pioneering analytical work of Finnie [27], the impacting particle was assumed not to rotate significantly during the impact. The force vector resisting the particle penetration was assumed to be concentrated at the tip of the particle and have a constant direction. In this case, the equations of motion could be integrated analytically. In Finnie's model, changes in particle shape could be accounted for by changing the direction of the resisting force, but the effect of particle orientation on the resulting material removal was not considered.

Hutchings [1], [25] improved Finnie's model by considering square particles which could rotate freely during the erosion process. In this case, the resisting force was distributed over the surface of the particle, with its direction changing instantaneously during impact. The resulting equations of motion were solved numerically. The model was capable of predicting a ploughing damage mechanism in addition to the machining or cutting mechanism observed in the Finnie's model. Papini and co-workers [26], [28–30] generalized Hutchings' rigid-plastic theory, so that particles of any shape with any initial orientations impacting targets of arbitrary dynamic hardness and dynamic friction coefficient could be analyzed. A catapult apparatus was used to launch the particles in the velocity range of 19-26 m/s. The predictions of the rigid-plastic theory were found to be in good agreement with the experimental measurements of crater size in many cases; however, it was not capable of directly simulating the machining of a chip by backward rotating particles.

Rigid-plastic models do not consider the presence of the material pile-up at the edge of the crater, which can lead to significant errors in predicted particle velocity and rebound angle [23]. Moreover, observations of eroded surfaces have showed that the main mechanism of the material removal is a combination of extrusion and forging. The platelets or lips formed by particle impacts may be pressed, loosened and removed by subsequent impacts [31], mechanisms that single particle rigid-plastic analyses can obviously not consider. It has also been found that the assumption of perfectly plastic behaviour, which neglects elastic spring back, temperature effects, and strain hardening, does not always adequately represent the resistance of materials to erosion [31]. Finally, the use of rigid-plastic theory for modeling the impact of multiple particles is extremely complex, and difficult to implement computationally. Development of a model in which multiple and simultaneous particle impacts can be more easily implemented, with more realistic material models, is thus desirable.

The finite element (FE) method has been used extensively in the modeling of single particle impacts to study residual stresses resulting from impact [32], to evaluate the amount of kinetic energy dissipated due the stress wave propagation and plastic deformation [33] and to predict the depth of a cut developed in the target material in abrasive waterjet machining [34]. In all of these studies, however, the particles were assumed spherical, which is not representative of the granular particles used in applications such as abrasive jet micromachining.

1.3.2 Representative models of erosive particles

While most practical solid particle erosion processes involve granular particles, experimental, analytical and numerical studies of single particle impact have been mostly limited to spherical particles (e.g. [1], [34–37]). Bitter [38] argued that if one assumes that small non-spherical particles have rounded edges, it is likely that only the rounded portion penetrates into the surface. However, other investigators [25], [26] have shown that angular particles can perform pure machining in which a chip of material is removed by a single particle. Although evidence exists that in some cases the same deformation pattern exists on impacted surfaces when angular or spherical particles are used [35], [39] it has also been found that the shape of particles can strongly affect the impact angle dependency of erosion [40]. Experiments using a centrifugal accelerator type erosion tester have also revealed a large difference in measured erosion rate between angular and spherical particles, particularly at low impact angles with respect to the target surface [41]. Moreover, it has also been found that the effect of particle size on erosion rate is different for spherical and angular particles [42], and can result in different erosion mechanisms [43]. The most recent study on this issue by Desale et al. [44] demonstrated the importance of considering particle shape in modeling solid particle erosion. They performed erosion tests on two steel alloys using quartz, alumina and silicon carbide erodent particles, each of which had dissimilar shape. While alumina and silicon carbide particles were angular, the quartz was blockier in shape. The alumina particles were found to be more angular with a higher slenderness ratio than the silicon carbide. Their study showed that the erosion rate of ductile material varied significantly with particle shape, especially at shallower angles of attack. Scanning electron microscopic (SEM) examination of the eroded surfaces revealed that the material removal mechanisms depended on the erodent shape. However, the maximum angle of erosion rate was found to be independent of particle properties, being only controlled by the target properties. This observation has sometimes been used by researchers to verify their numerical models of particle erosion using spherical particles with experiments performed using angular particles. However, the erosion rate and material removal mechanisms from spherical and angular particles cannot be compared, since that requires implementation of the actual particle shapes in the model.

These observations demonstrate that modeling the effect of the shape and angularity of solid particles is crucial to a better understanding of the micro-mechanisms responsible for material removal during solid particle erosion. Despite this, most previous models of the damage due to particle impact utilize a single representative particle shape with a uniform size. Also, the previous single angular particle impact studies were performed using relatively large-scale well defined 2D particles. To date, no model has been proposed for the study of the much smaller 3D irregularly shaped particles found in practical solid particle erosion applications.

The modeling of such particles is complex, due to the variety of particle shapes in abrasive powders, the difficulty in finding appropriate shape representative parameters, the limitations associated with shape measurements, and the lack of appropriate techniques to classify particle shapes [45]. Lin and Miller [45] used X-ray microtomography (XMT) for the 3D analysis of particle shape to simulate and reconstruct irregularly shaped particles in particulate separation processes. They applied this technique for the shape analysis of particles with a minimum volume of 0.2567 mm^3. However, the particles involved in solid particle erosion phenomenon are usually much smaller; e.g. 150 μm alumina particles have an average volume of 1.547×10^{-3} mm^3. Therefore, it is doubtful that an XMT analysis which requires individual scanning of each particle can be utilized for such small particles. Pellegrin and Stachowiak [46] developed a method to simulate abrasive particles with random polyhedrons. These polyhedrons were generated by cutting a cube with planes whose direction and position distribution were randomly chosen. The simulated particles were numerically and visually similar to actual particles, but the particle generation strategy was not used to obtain a sample of simulated particles whose distribution of size and shape parameters matched the attributes of a specific powder sample. None of the previously described particle models was verified by comparing the simulated damage done to the surface with that resulting from actual particle impacts.

1.3.3 Numerical modeling of solid particle erosion of ductile metals

Given the complexities of solid particle erosion phenomena, a number of investigators have attempted to understand material removal mechanisms using numerical models. Such models allow the tracking of individual particle impacts, and can be beneficial in analyzing the cooperative effects of multiple impacts on the resulting erosion, in addition to allowing the study of individual process parameters separately. In contrast to analytical models which suffer from simplified assumptions and require tuning certain parameters, computer models can be developed based on a more sophisticated and realistic modeling of the target and particles, and the interaction between them. Until now, such models have been limited to either co-incident (i.e., impacting at a single location) or non-coincident impacts of identically shaped and sized spheres. For example, Aquaro [47] developed an erosion criterion for ductile materials and implemented it in a finite element model in which eight 50 μm spherical particles impacted coincidently on a stainless steel target at oblique incidence. An erosion model based on the work of Bitter [48] was used to identify those elements that were damaged. When the damage criterion was calibrated with measured erosion rate data, the erosion rate predicted by the FE model compared fairly well with experimental results.

Wang and Yang developed a coupled finite element and smoothed particle hydrodynamics (SPH) model [49] to study five coincident impacts of 500 μm spheres on Ti-6Al-4V. Johnson-Cook constitutive and damage models were assigned to the target. Although no comparison was made to experimental data, the dependence of the simulated erosion rate due to the five coincident impacts was found to follow the same trend as Bitter's model [48]. ElTobgy and Elbestawi [50] also developed a Lagrangian finite element model utilizing an element deletion criterion for the simulation of the erosion of Ti-6Al-4V using the coincident impacts of four spherical particles. The model prediction for the angle corresponding to maximum erosion was consistent with that predicted by the models of Bitter [14] and Neilson and Gilchrist [51]. It is not clear, however, whether either of the numerical models in [49] and [50] can simulate the formation of shear bands, which are known to be a contributing phenomenon to material loss from Ti-6Al-4V [52] and other hard metals [53]. While the previously described coincident impact models established the feasibility of the numerical modeling of erosion phenomena, they are incapable of simulating the interaction between the impacting particles and raised crater lips, which may play an important role in the erosion of ductile materials [31]. Woytowitz and Richman [54] developed a 3D Lagrangian finite element model of multiple, non-overlapping stochastically located impacts of spherical particles on a copper target at perpendicular incidence. An element damage model based on a relationship between number of cycles to failure and plastic work per cycle was utilized to predict the material loss. However, the model suffered from problems associated with excessively damaged elements in a given surface layer not being eliminated from the model, thus hindering the simulation of failure progression to beneath the surface. Therefore, the model was only applicable for simulating the impact of a limited number of spherical particles, and it over predicted the measured erosion rates.

Wang and Yang [55] developed a 3D Lagrangian finite element model for non-coincident impacts of 100 spherical particles on Ti-6Al-4V alloy. A Johnson-Cook constitutive equation and failure model were utilized to define the target material flow behavior and the criteria for element deletion. The predicted dependency of erosion rate on impact velocity, i.e. the velocity exponent, was in the range found in the literature for ductile metals, and the predicted angle at which the maximum erosion rate occurred agreed with experiments [56] involving angular silicon carbide particles. This use of idealized spherical particles to simulate experiments with angular particles was motivated by the observations of Desale et al. in [44], who claimed that the maximum angle of erosion rate did not depend on particle properties. However, there is a wealth of data in the literature that clearly shows that the magnitude of the erosion rate, and the associated material removal mechanisms, both depend strongly on particle shape [41], [43], [44].

Besides these numerical attempts to model solid particle erosion, there are a number of works on modeling manufacturing processes such as orthogonal cutting and machining which provide useful background for the modeling of solid particle erosion. These manufacturing processes, like erosion, involve the large deformation of material, the selection of appropriate constitutive and strain rate dependency equations, and the implementation of material failure modeling. For example, Guo and Yen [57] utilized the Arbitrary Lagrangian Eulerian (ALE) adaptive meshing in ABAQUS/Explicit to simulate discontinuous chip formation during high speed machining of a hard steel alloy (AISI 4340) using a Johnson-Cook constitutive and damage model. An Eulerian finite element model of copper subjected to orthogonal cutting was also developed by Raczy et al. [58] to investigate the deformation zone ahead of the cutting tool and the continuous chip geometry. The present author also attempted to use an Eulerian approach to solid particle erosion which was unsuccessful due to numerical instabilities such as nodal “out-of-range-velocities” when a Johnson-cook damage model was implemented.

Researchers have also applied SPH formulations to simulating metal cutting process [59–61]. Akarca et al. [59] compared the Eulerian and SPH techniques in modeling Al1100 during machining using LS-DYNA. The flow behaviour of aluminum alloy was defined using two different models, an exponential and a Johnson-Cook constitutive equation. Since a continuous chip was simulated, no damage model was utilized. Their investigations showed that the Eulerian model was the most appropriate model to represent experimental observations. However, when the computational time was considered, the SPH model was a more suitable choice with a relatively good accuracy.

Although these previous studies showed the promise of numerical modeling of erosion phenomena, as mentioned previously, they were limited to impacts of uniformly sized idealized spherical particles. The models were not utilized to identify actual material removal mechanisms. Most particle erosion processes involve the impact of irregularly shaped particles of various sizes, a much more complex situation that may involve any number of different erosion micro-mechanisms.

1.3.4 Material removal mechanisms in ductile metals

For ductile erosive processes, there is a general agreement that extensive plastic deformation is necessary before metal is removed from surface; however, researchers have proposed different mechanisms for specifying how the plastic deformation leads to material loss.

Finnie's pioneering work [27] proposed a micromachining mechanism for erosion of ductile materials that, however predicted a zero erosion rate at normal impact which did not agree with experiments. Later, more detailed single particle impact studies [29], [62] demonstrated that such a pure machining mechanism by angular particles is only probable for a very narrow range of impact angles and orientations. Neilson and Gilchrist [51] and Bitter [48] suggested that the erosion at normal incidence was due to the formation of an embrittled thin surface layer which then fractured. Christman and Shewmon [53] conducted a detailed experimental study on the interaction of successive overlapping impacts of spherical particles on a strong aluminum alloy and found that significant metal loss was only observed when overlapping of craters occurred [63]. Hutchings [36] developed a model for overlapping impacts based on a critical strain at which the material was expected to be removed from the surface after a number of plastic deformation cycles. Levy [64] observed that a combined extrusion-forging mechanism was responsible for material loss at all particle impact angles. Through this mechanism, raised or extruded material from craters might be forged, then loosened and knocked off by subsequent impacts. This was supported by the similarity in deformation patterns for normal and oblique impact when eroded surfaces of aluminum, copper, and iron were studied using SEM [63].

Identifying material removal mechanisms through numerical modeling of multiple particle impact has been mostly neglected in the previous studies. This can be attributed to the complexity of the erosion process which involves the interaction of the impacting particles with the features generated on the surface by the preceding particles. A numerical model of particle impact cannot exhibit material removal mechanisms unless it is capable of handling this complicated deformation state. Development of such a model forms the main objective of this dissertation.

1.4 Dissertation outline

In **Chapter 2**, the gas gun apparatus which was utilized to perform single impact experiments is described, along with the development of a Lagrangian FE model to study single impacts of rhomboid particles. **Chapter 3** describes an SPH model for single impacts of rhomboid particles on a ductile metal that does not suffer from the shortcomings of the Lagrangian FE technique used in Chapter 2. This model is utilized to identify impact mechanisms in angular particle impact. **Chapter 4** describes a methodology for generating 3D models of irregular shape particles based on the size and shape parameters of measured samples of actual alumina powder. These modeled particles were used in an SPH based simulation in **Chapter 5** to simulate non-coincident impacts on an aluminum alloy target. The model was extended for multiple overlapping impacts in **Chapter 6**, where material removal mechanisms in particle erosion of ductile metals were also identified and compared with experimental interpretations. Finally, a summary of the major findings and conclusions of the dissertation is presented in **Chapter 7** as well as some suggestions for future research.

Chapter 2 Lagrangian Finite Element Modeling of Single Particle Impacts

2.1 Introduction

As discussed in **Chapter 1,** the study of single particle impacts can be beneficial to understanding the fundamental mechanisms of solid particle erosion. However, there has not yet been a study of single angular particles impact that considers the effect of temperature and strain rate on the target material, and has the ability to model surface features such as the formation of piled up material at the crater edge.

This chapter presents a comparison of finite element techniques for studying the behaviour of ductile materials due to the impacts of single two dimensional idealized rhomboid particles (**Fig. 2-1**) at different particle orientations (θ_i) and angles of attack (α_i). A specially built apparatus used to verify these models is also presented. Most of the content of this chapter has been published in [24].

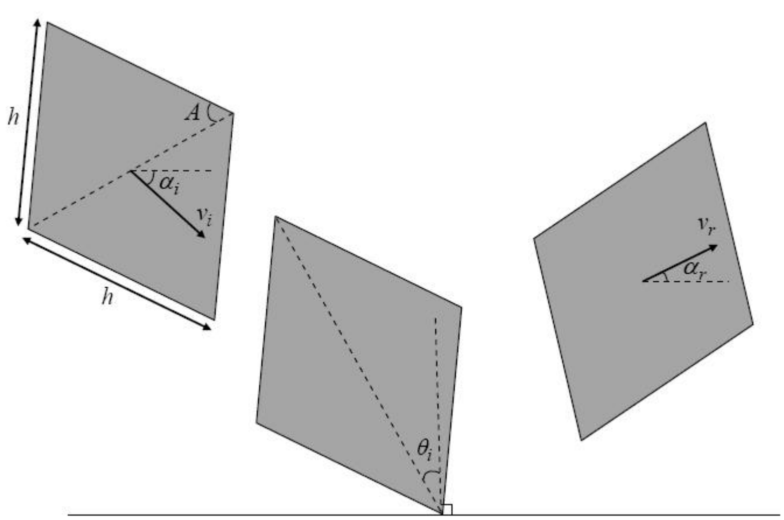

Fig. 2-1. Two-dimensional rhomboid particle parameters. The particle has a uniform thickness, *w*.

2.2 Experiments

A compressed nitrogen gas gun with a rectangular cross-section barrel, shown schematically in **Fig. 2-2**, was designed and built in order to study the two dimensional (i.e. incident velocity vector in the same plane as the flat side of the particle) impact of single rhomboid particles on ductile materials. The gas gun shown in **Fig. 2-3**, which was similar to that developed by Hutchings et al. [65], has a barrel made of two bars of mild steel AISI 1018 each having a 101.6 ×25.4 mm rectangular cross section. A 3.2×31.8 mm slot was milled along the length of one of the bars, along which the sabot containing the particle travels. The two bars were screwed together and sealed using an o-ring. Upstream of the barrel, the rectangular slot is tapered to a cylindrical bore, accommodating a solenoid valve, which acts as a trigger. The two-way solenoid valve (Model 4005049-001, Honeywell International Inc., Morristown, NJ) has a maximum working pressure of 10 MPa, a 6.35-mm orifice, with an opening time of approximately 60 ms.

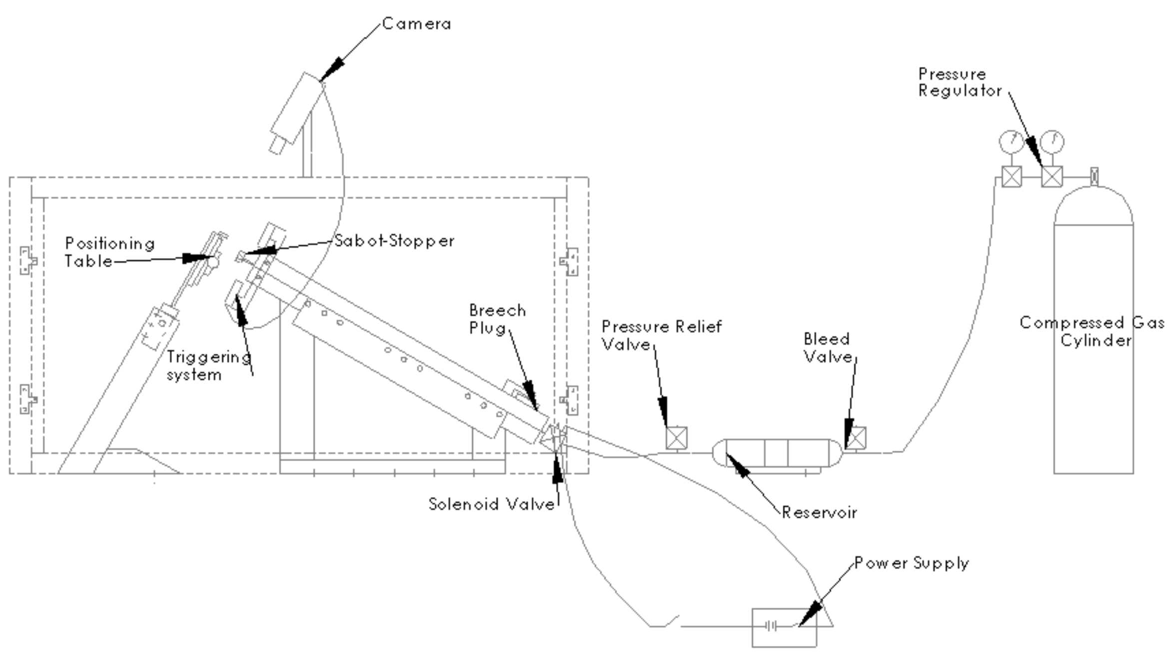

Fig. 2-2. Schematic of experimental setup.

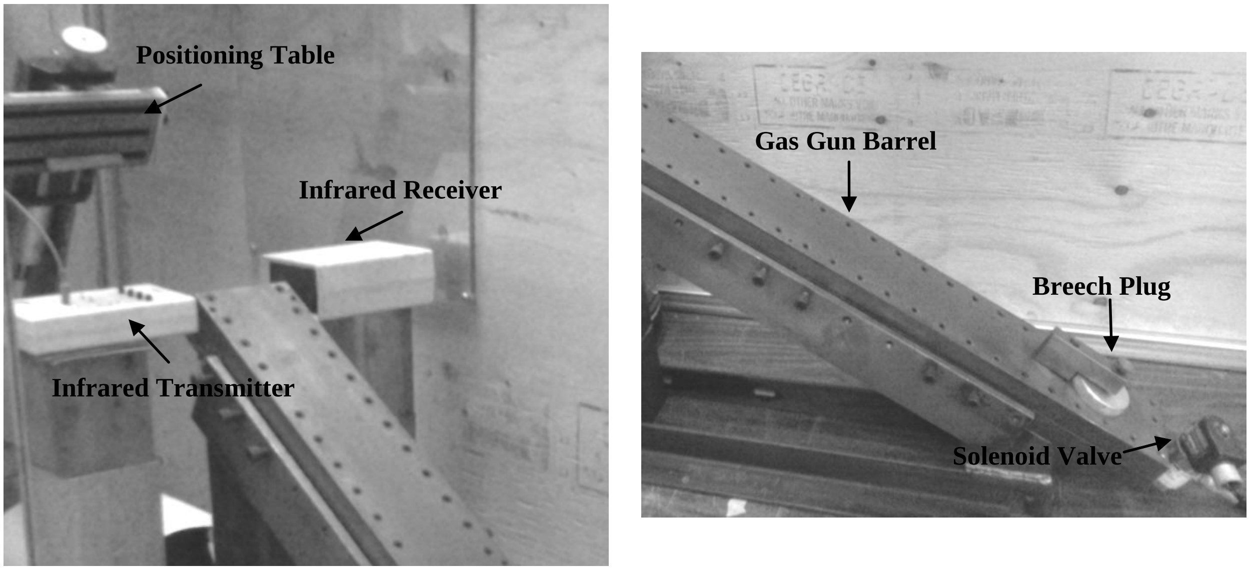

(a) (b)

Fig. 2-3. Photographs of gas gun used to perform single impact tests.

Since the experimental studies involved the use of different particle shapes with different initial orientations, a carrier (sabot) (**Fig. 2-4**) which fits inside the barrel slot was chosen to carry the particle along the barrel. A breech hole was machined at the bottom of the barrel to allow the insertion of the sabot which carries the particle. The traveling distance of the particle along the gas gun barrel is 762 mm. For each particle shape and orientation, carriers with different slots were machined (**Fig. 2-4**).

One of the main challenges in obtaining good repeatability in the gas gun was developing a methodology to reliably stop the sabot, while allowing the particle to separate from the sabot and impact the surface. The concern was to minimize the influence of the stopping process on the particle orientation in the carrier. Different stopper materials were evaluated including metal plates, silicon rubber sheets, and springs. Ultimately, rubber gum (I.R.P. Industrial Rubber Ltd, Mississauga, Ontario) was identified as a suitable material to be used as a sabot stopper. It has a high tearing strength and also it provides good flexibility to absorb impact energy. For the sabot itself, Nylon 6/6 and polyethylene were initially used, but were found to crack after only one or two shots. Plastic foams were found to be not stable enough during the barrel acceleration. Ultimately, polycarbonate (Lexan) was found to be the best sabot material.

After deciding on the sabot material and stopper, repeatability remained a problem, as the particle was found to sometimes hit the surface out of plane, and the impact location was also found to be inconsistent. These issues were traced to a problem with the manufacturing tolerance between the carrier and the gas gun barrel; i.e. the carrier was not completely tight in the barrel while sliding. Increasing the thickness of the sabot by attaching layers of tape on the faces of the sabot has provided a useful temporary fix. This led to repeatable and in-plane impact of particle on the target.

Using compressed nitrogen at 345 and 690 kPa, the gas gun was used to accelerate particles with $A = 60°$, $h = 5.46$ mm and $w = 3.20$ mm (**Fig. 2-1**) to speeds of 50 and 80 m/s, respectively. The particles were CNC machined out of AISI A2 tool steel plates and heat treated to increase their hardness.

The incident angle of attack and incident orientation angle were varied by changing the angle between the target and the gas gun barrel and using sabots with different slots for carrying the particle, as shown in **Figs. 2-4** and **2-5**. The target material was oxygen free high conductivity copper (OHFC C10100) with a Brinell hardness of 26. The static hardness of the particles was measured as Brinell 752, which is sufficiently larger than that of the target to ensure that deformation of the particle during impact was negligible.

A FlashCAM high-speed digital camera (Cooke Corp., Auburn Hills, MI, USA), coupled to a MultiTRIG (Cooke Corp., Auburn Hills, MI, USA) infrared trigger and a video frame grabber were used to take multiple exposure of the particles in flight. Image analysis software was employed to measure the particle incident and rebound angles and velocities. There was an uncertainty in measurements of linear velocities on the order of 2 m/s, and of angular measurements of 3° on the images due to blurring. A non-contact optical profilometer (Nanovea ST400, Micro Photonics Inc., Allentown, PA, USA) was used with an optical pen having a measurement range of 3.5 mm to measure the 3D profile of the craters formed by the particle impacts, from which the volume and maximum depth of crater were extracted. The system had a lateral resolution of 3.5 μm and depth resolution of 10 nm.

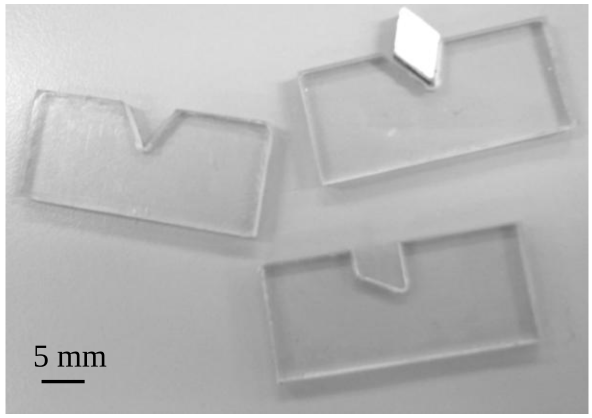

Fig. 2-4. Sabots used to carry particles within gas gun.

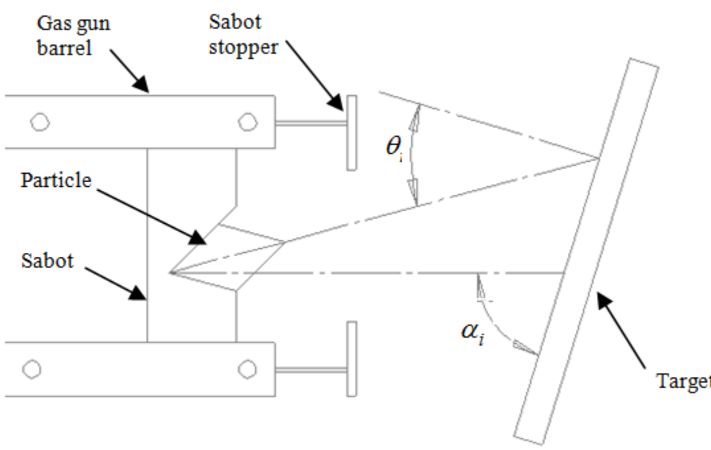

Fig. 2-5. The orientation of the particle in the barrel with respect to the target.

2.3 Finite element modeling

To model the experimental impacts of the particles shown in **Fig. 2-1**, the explicit finite element code LS-DYNA 971 (Livermore Software Technology Corporation, Livermore, CA, USA) was used. **Fig. 2-6** shows the FE model of the single particle impacts described in **Section 2**, which was developed using four-node plane strain elements (ELFORM 13), having one point of integration. The plane strain assumption was justified by the constraint imposed by the material surrounding the impact area in the out-of-plane direction, although this required neglecting the edge effect on the resulting crater dimensions. Also, given that explicit dynamic analyses typically require very small time step sizes in order to preserve solution stability, the use of reduced-integration elements is attractive, in order to minimize the computational cost.

However, under-integrated formulations frequently lead to the development of spurious zero energy (hourglass) modes [66]. In the present work, a stiffness hourglass mode control was utilized, in order to minimize these problems. The target was assigned zero-displacement boundary conditions at its bottom and along the sides, while the particles were assigned initial linear velocities matching those from the experiments. The target width and depth were assigned as 10 and 4 mm, respectively. These dimensions ensured that the boundary conditions did not have an influence on the response of the material.

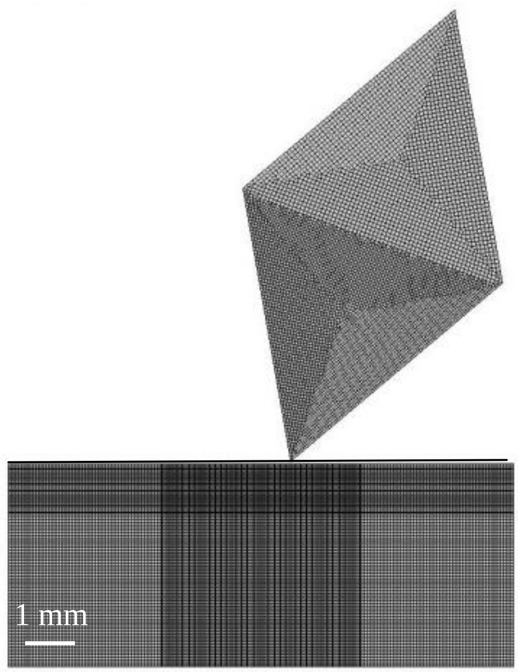

Fig. 2-6. Typical mesh used in finite element modeling of the particle and the target, for θ_i = 20°.

2.3.1 Material model

The particle was assumed to be rigid and nondeforming. However, since a prescription of the elastic material properties was needed for the contact algorithm, the elastic properties of steel (E = 200 GPa, ν = 0.3) in addition to its density (7800 kg/m^3) were used to define the particle material. For the oxygen free high conductivity (OFHC) copper target, the Johnson-Cook elastic-plastic model in LS-DYNA (MAT15) was employed. It describes the flow strength, σ_Y, as a function of the effective plastic strain, ε_{eff}^{p}, the effective plastic strain rate, $\dot{\varepsilon}_{eff}^{p}$, and the temperature, T [67]:

$$\sigma_Y = (\sigma_0 + B(\varepsilon_{eff}^{p})^n)(1 + c\ln\dot{\varepsilon}^*)(1 - T^{*m}) \tag{2-1}$$

where the normalized strain rate and temperature are defined as:

$$\dot{\varepsilon}^* = \frac{\dot{\varepsilon}_{eff}^{p}}{\dot{\varepsilon}_0} \tag{2-2}$$

$$T^* = \frac{T_{\text{inst}} - T_{\text{ref}}}{T_{\text{melt}} - T_{\text{ref}}} \tag{2-3}$$

T_{inst}, T_{melt}, and T_{ref} are the instantaneous, melting, and reference temperatures, respectively. The parameters σ_0, B and n are material parameters that are required to describe the initial yield and strain hardening behaviour of the material at a strain rate of $\dot{\varepsilon}_0$ and a temperature of T_{ref}. The parameters c and m describe the material strain rate and thermal softening sensitivity, respectively. In the present work, $\dot{\varepsilon}_0$ was taken as $1\,\text{s}^{-1}$ and the effect of thermal softening was neglected. A linear polynomial equation of state (EOS) in which the change in material volume (ΔV) is related to the applied pressure (*p)* with the material bulk modulus (*K*) was utilized in the present work:

$$p = K\Delta V \tag{2-4}$$

The material properties of the (OFHC) copper implemented in the finite element model are listed in **Table 2-1**, based on those measured in Ref. [68]. The static stress-strain curve of OFHC in simple tension is also plotted in **Fig. 2-7**.

Table 2-1 Material properties of OFHC copper [68]

Material properties	Symbol	Value
Density	ρ	8960 kg/m^3
Shear modulus	G	46 GPa
Bulk modulus	K	140 GPa
Poisson's ratio	ν	0.34
Tensile failure strain	FS	0.46
J-C yield strength	σ_0	90 MPa
J-C hardening coefficient	B	292 MPa
J-C strain hardening exponent	N	0.31
J-C strain rate constant	C	0.025

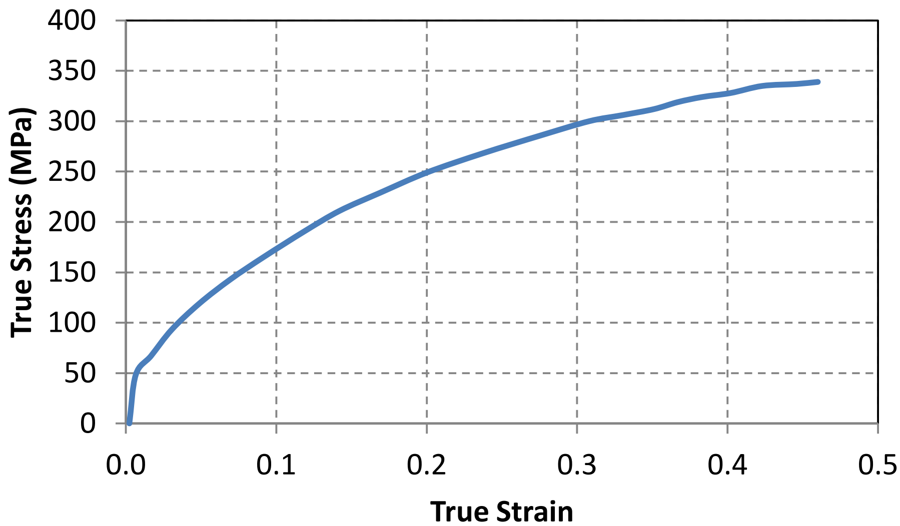

Fig. 2-7. Static true stress vs. true strain in simple tension of OFHC [69].

2.3.2 Contact model

Contact was treated using a penalty approach, using the automatic-single-surface contact algorithm in LS-DYNA. In this scheme, once contact surfaces are determined, an interface restoring force, determined from the properties and geometry of the elements hosting the sliding segment, is imposed on the slave node and distributed across the nodes on the master segment. Dynamic friction coefficients are usually considered to be small in impact problems, and in past finite element investigations, the effect of friction has been neglected (e.g. [70]). In the present work, a friction coefficient of 0.1 was used.

2.3.3 Element deletion and remeshing

Element distortion is a problem that occurs during the modeling of large deformation impact problems in the Lagrangian formulation. Highly distorted elements can result in inaccurate calculation of stresses and strains. Moreover, since finite element solvers often derive the solution time step from the smallest element dimension, highly distorted elements can lead to calculations that take an impractical amount of CPU time.

Different methods have been developed for dealing with the large deformation problem. In the element deletion approach adopted in the present study, when the plastic strain of an element reaches a critical value, that element is removed from the model. The selection of values for critical strain is essentially a trade-off between prolonging an element's life for as long as possible, whilst at the same time, not sacrificing any computational time or accuracy as a result of the increasing distortion. Though useful results can be obtained, their reliability depends on an adequate determination of a non-physical element failure strain. In the present simulations using element deletion, a constant critical plastic strain of 1.5 was defined in the model as a criterion for the material damage, based on a best fit with the experimental results.

Another technique developed for dealing with the large deformation problem is remeshing, in which, at the beginning of pre-defined time intervals, a completely new mesh is generated, so that element distortion is limited to that seen in a single interval. This removes the need for defining a separation criterion when modeling the continuous chip formation typical of, for example, cutting mechanisms. When the breakage of the chip from the surface also needs to be modeled, the use of remeshing in conjunction with element deletion would be desirable, in order to account for both the chip separation, and the distortion of elements. However, due to numerical instabilities, using this approach is not feasible in LS-DYNA [71]. Thus, in the present study, remeshing was not used for the simulation of situations which caused chip separation from the target. The characteristic element size was defined as 20 μm in the present work.

2.4 Rigid-plastic Model

The experimental impacts were also modeled using the rigid-plastic theory of Refs. [26], [28], [29], which assumes that the instantaneous contact force resisting the impact is directly proportional to a constant dynamic hardness, p_d , multiplied by the instantaneous contact area.

The model also allows for the action of friction forces, proportional to a constant friction coefficient multiplied by the instantaneous contact forces. The analysis results in a differential equation of motion of the particle as it moves through the target material, which must be solved numerically in time steps to yield the particle trajectory, crater volume, and particle rebound kinematics. Based on the experimental results from normal impacts (α_i = 90° and θ_i = 0°), and using the techniques described in Ref. [26], best fit values of p_d = 700 MPa and μ = 0.2 were used for the presently considered impacts. The numerical model implemented in MathCad 14 (PTC Corp, Needham, MA, USA) is identical to that used in Ref. [29]. For the impacts simulated in the present work, time steps in the range of 0.05-0.1 ms were sufficiently small to ensure convergence of the solution.

2.5 Results and discussion

The incident conditions used in the experiment, which were simulated using the FE and rigid-plastic models are given in **Tables 2-2** and **2-3**, together with the predictions of the two FE, and the rigid-plastic models. **Fig. 2-8** shows how the maximum depth (d_{max}) and lip height (h_{lip}) for each crater were measured. Also, the crater volume (CV) was calculated by multiplying the area of the cross hatched surface, shown in **Fig. 2-8**, by the thickness of the particle. Depending on the particular combination of incident parameters, the impacting particles typically either tumbled forwards (**Fig. 2-9**), or backwards (**Fig. 2-10**). Forward rotating particles result in target material being pushed to the edge of deep and short triangular craters. This was observed in the measured and predicted crater profiles, shown in **Fig. 2-11a**, corresponding to data point 2 in **Table 2-2**. Two examples of forward rotating cases were considered (data points 2 and 3) in the present work, and the rest were backwards rotating. As noted also by Papini and co-workers [26], [30] an initial backward rotation of the particle does not necessarily lead to the pure machining action which was seen by Hutchings [25], involving the cutting of a smooth crater as the particle sweeps along the surface, with a rebound angle less than 90°. However, in most cases (data points 4, 6, 7 and 9), the initial backward rotation of the particle does involve a pure machining; resulting in the formation of two craters (**Fig. 2-12**). The first crater is formed due to the cutting of material off the target by the leading vertex of the particle. The rotation of the particle causes scratching the surface by the trailing vertex of the particle which forms the second crater, as shown in **Fig. 2-11b**, corresponding to data point 6.

Table 2-2 Predicted and measured rebound parameters. The experimental results for each data point are the average of three measurements. The impact variables refer to **Fig. 2-1**.

	Incident parameters			Rebound parameters							
				Experiment		FE (adaptive remeshing)		FE (element erosion)		Rigid plastic	
Data Point	V_i (m/s)	α_i (deg)	θ_i (deg)	V_r (m/s)	α_r (deg)	V_r (m/s)	α_r (deg)	V_r (m/s)	α_r (deg)	V_r (m/s)	α_r (deg)
1	80	80	20	6	102	8	121	9	116	9	0
2	81	60	20	14	47	12	55	13	49	12	37
3	46	60	20	7	55	3	52	8	48	7	30
4	81	60	40	28	33	-	-	17	31	35	18
5	50	60	40	6	113	4	101	4	92	-	-
6	85	50	50	33	15	-	-	41	20	63	0
7	51	50	50	17	32	-	-	19	25	28	19
8	80	40	40	8	66	16	62	17	61	16	54
9	81	40	50	41	12	-	-	45	14	65	2

Table 2-3 Predicted and measured crater dimensions. The experimental results for each data point are the average of three measurements.

	Experiment			FE (adaptive remeshing)			FE (element erosion)			Rigid plastic		
Data point	CV (mm³)	d_{max} (mm)	h_{lip} (mm)	CV (mm³)	d_{max} (mm)	h_{lip} (mm)	CV (mm³)	d_{max} (mm)	h_{lip} (mm)	CV (mm³)	d_{max} (mm)	h_{lip} (mm)
1	2.23	0.84	0.35	3.04	1.05	0.43	2.33	1.02	0.45	3.01	1.03	-
2	2.47	0.97	0.57	2.56	1.07	0.49	2.78	1.09	0.55	2.83	1.10	-
3	0.68	0.35	0.35	0.87	0.59	0.26	0.95	0.67	0.30	0.92	0.64	-
4	1.28	0.27	-	-	0.47	-	2.64	0.51	-	3.43	0.46	-
5	0.88	0.34	0.71	1.07	0.35	0.52	1.21	0.38	0.77	1.54	0.35	-
6	1.72	0.295	-	-	0.26	-	1.31	0.31	-	2.74	0.25	-
7	0.81	0.16	-	-	0.16	-	1.53	0.20	-	0.66	0.15	-
8	1.65	0.58	0.79	2.69	0.75	1.04	3.33	0.81	0.85	3.67	0.73	-
9	0.75	0.29	-	-	0.23	-	1.28	0.28	-	1.96	0.20	-

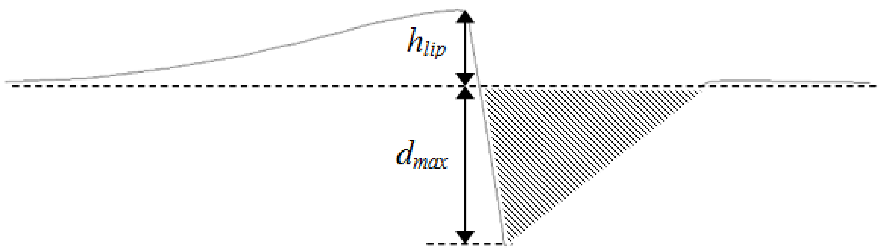

Fig. 2-8. Crater parameter definitions.

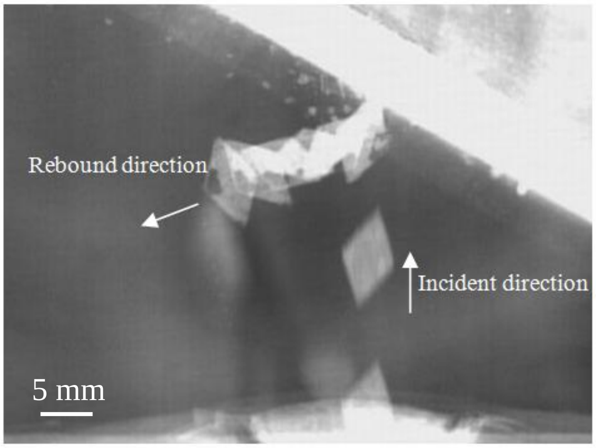

Fig. 2-9. Forward rotation of a particle during impact, corresponding to data point 2 in **Table 2-2**.

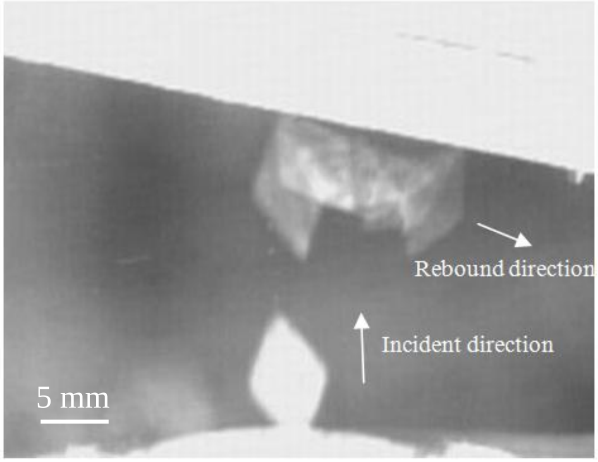

Fig. 2-10. Backward rotation of a particle during impact, corresponding to data point 1 in **Table 2-2**.

In the case of data point 8 (**Fig. 2-13**), the particle leading vertex tunnels under the target while it is rotating backwards, then, just before rebound, a transition to forward rotation occurs. For data points 1 and 5, the particle rebounds from the surface with a rebound angle (α_r) greater than 90° after tunnelling under the target while rotating backwards (e.g. **Fig. 2-10**). For both data points 5 and 8, the particle lost most of its kinetic energy and the particle is close to embedding in the target. Another case has been reported by Dhar et al. [30] in which a particle with angularity of 60° tunnels into the target, and when it has rotated to the point where it is lying on its side, a chip is ejected from the target. The rebound angle of the particle is greater than 90°. Raised material formed at the leading edge due to the particle tunnelling below the surface of the crater distinguishes this type from the pure machining action of backward rotating particles. Such impacts were not observed in the present analysis.

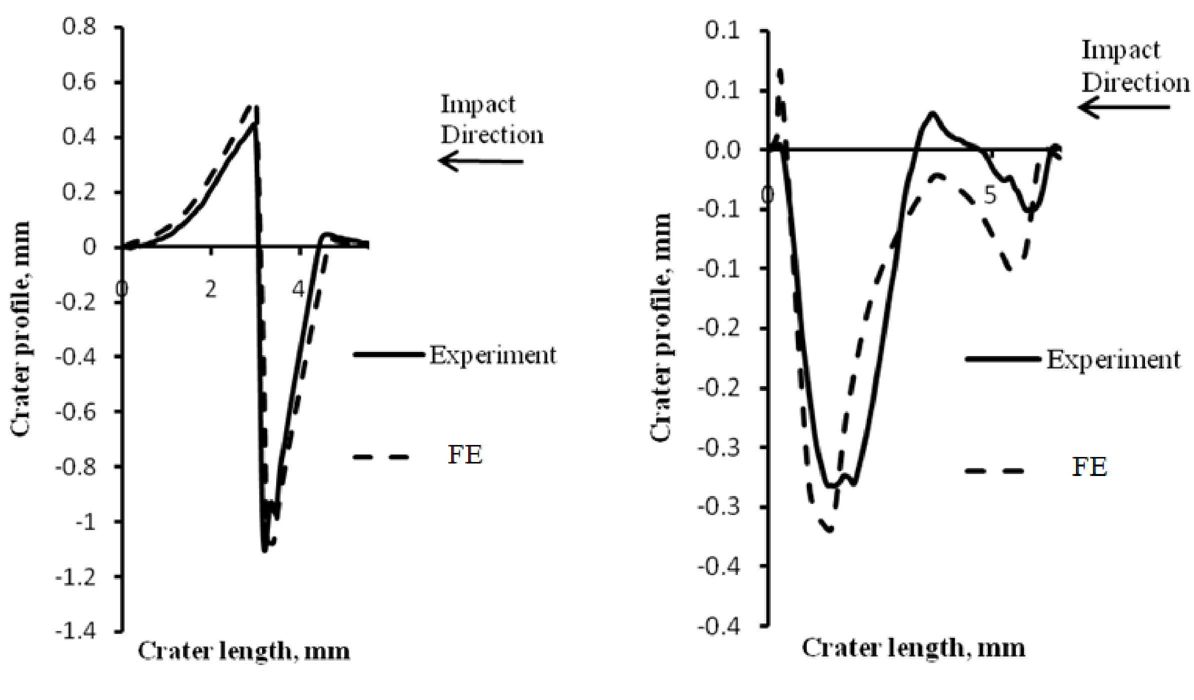

(a) (b)

Fig. 2-11. Measured and FE predicted craters for (a) data point 2 and (b) data point 6 in **Table 2-2**.

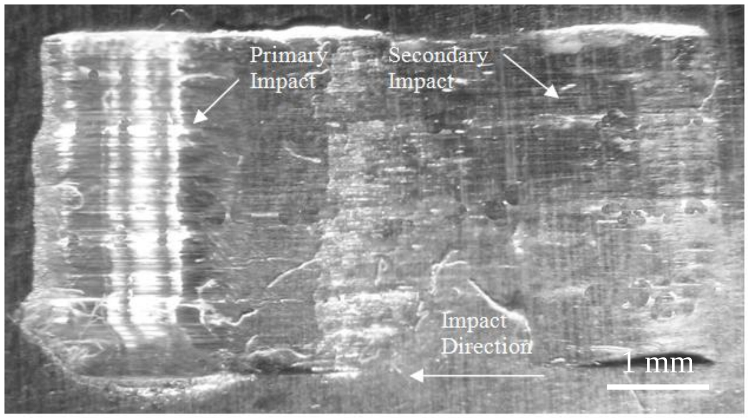

Fig. 2-12. Craters left by backward rotation of the particle corresponding to data point 4 in **Table 2-2**. The larger crater was the primary crater cut by the leading edge followed by the smaller crater cut by the adjacent edge.

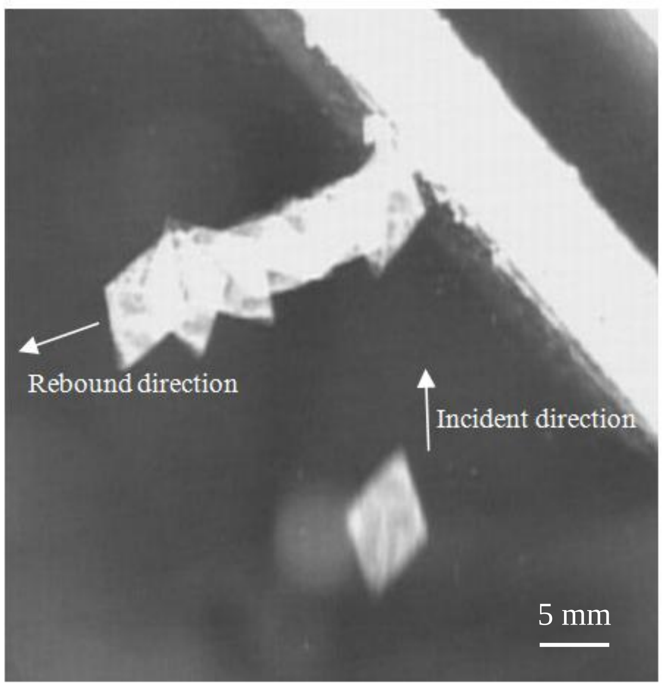

Fig. 2-13 A transition from backward to forward rotation corresponding to data point 8.

Tables 2-2 and **2-3** present the predicted rebound velocity (V_r), rebound angle, crater volume, maximum crater depth and height of the raised material at the leading edge of the particle using the FE model with remeshing, the FE model with element deletion, and the rigid-plastic model, compared to the corresponding measured values. In some cases (data points 4, 6, 7 and 9), multiple collisions with the target occurred during the backward rotation, and the rebound parameters were thus measured and predicted after the secondary hit.

Table 2-2 shows that the FE model with element deletion produced the best fit of predicted with experimental results for both rebound velocity and rebound angle. Of particular importance is the ability to simulate the chip machining and separation seen in data points 4, 6, 7 and 9). Since it was not possible to implement a damage model in the FE model with remeshing, the rebound parameters of the particle for cases involving chip separation could not be predicted by this technique. In all cases, the rebound angles predicted by the rigid-plastic model are lower than the measured values. As noted in previous work [26], the rigid-plastic cannot predict the point of chip separation, and the performance is thus poor in the backward rotating cases. For forward rotating particles, the most likely reasons for the differences between predicted and measured values are the presence of ploughed material ahead of the leading edge, and the elastic spring back of the crater, both of which are not considered in the rigid-plastic analysis [26], [30].

Table 2-3 shows that the FE model with element deletion produced the best fit of predicted with experimental results for crater dimensions and pile-up formed due to the impact. All models overestimated the volume and maximum depth of the crater. For finite element models, especially for the remeshing technique which uses only the flow parameters of the material to simulate the impact process, the strain rate effect could be an important reason for this overestimation of the crater volume. The assumption in the Johnson-Cook model that flow strength is scaled with the logarithm of strain rate is observed at fairly low strain rates. Experiments show that this relationship breaks down at a strain rate of 10^2 s^{-1} [72]. In the present analysis, it was found that the target material undergoes strain rates on the order of 10^6 s^{-1}.

The results obtained from the element deletion approach are encouraging, especially when it is noted that only a constant critical plastic strain has been used. However, the element deletion approach does not necessarily model a physical effect, but rather it imposes an approximation to the simulation. Therefore, the applicability of the method is particular to the specific problem being considered. For example, the simulations of Ref. [70] show that this method is deficient for the simulation of conical projectile impact; however, for blunt and spherical projectiles, reliable results could be obtained. The present analysis show that this is a promising approach for a relatively sharp particle having $A = 60^{\circ}$, however preliminary results (not shown) indicate that for the blunter square particles ($A = 45^{\circ}$), the element deletion method does not perform well.

For the pure machining action of a backward rotating particle (**Fig. 2-14**), the critical plastic strain defined in the element deletion approach carries a physical meaning related to the damage and rupture behaviour of the material. However, in the simulation of cases in which the particles penetrate deeply into the target (**Fig. 2-15**), the critical strain loses its physical meaning somewhat, because the crater formation is due to the gross deformation of material (e.g. plastic flow and extrusion to edges of the crater), rather than actual machining damage. Nevertheless, for the relatively sharp particles studied in this paper, the adjusted failure strain based on the backward situation also results in fairly good predictions for forward rotation. This FE scheme where a nonphysical failure strain is tuned to a particular particle impact condition might benefit future studies of multiple impacts of idealized two dimensional particles. However, for simulations utilizing multiple impacts of more realistically shaped three dimensional particles, a variety of material mechanisms are likely to occur, and a more robust technique that is based on physical rather than nonphysical parameters is likely to be needed.

The remeshing technique, while attractive for simulation of forward rotating impacts because it can eliminate distorted elements without resorting to a damage model, suffers from a number of shortcomings. Firstly, the computational costs are far higher than that involved with element deletion. At each remeshing step, a completely new mesh with uniform element size is generated for the whole model, also increasing the probability of the occurrence of numerical problems. It is likely that a combination of remeshing with an element deletion damage model would provide more promising results for solid particle erosion studies, allowing for the simulation of chip machining and separation. Unfortunately, in the implementation in LS-DYNA, use of a deleting element failure criterion together with remeshing results in numerical instabilities. If some elements are removed during a remeshing step, the adaptive procedure, when creating the new mesh, will still take into account the nodes that have been deleted, creating some elements that can have negative volume. This leads to an error termination of the simulation, as also noted in Ref. [71].

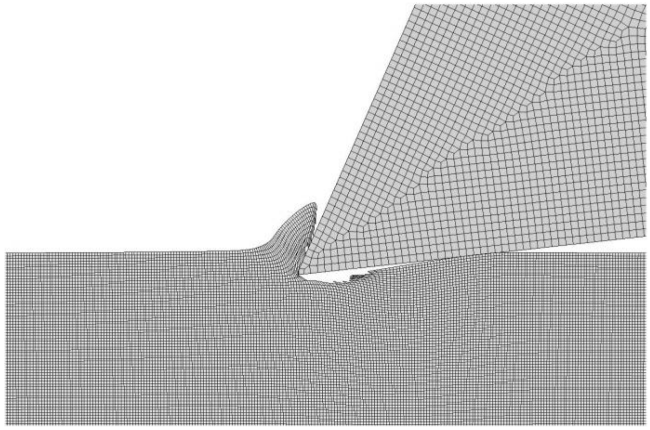

(a)

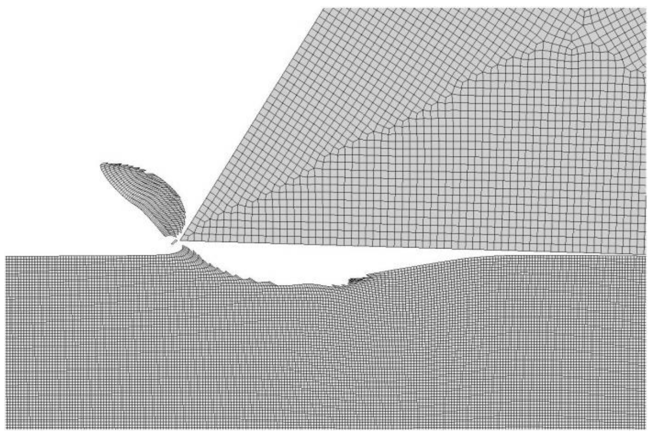

(b)

Fig. 2-14. Simulation of the chip separation using FE with element deletion, during backward impact of the particle corresponding to data point 8 in **Table 2-2**: (a) Initial penetration and tunnelling below surface (b) chip separation after machining.

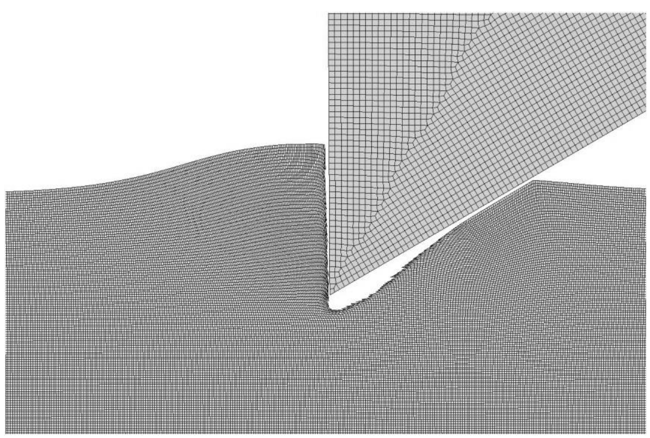

Fig. 2-15. Simulation of the particle impact using FE with element deletion corresponding to data point 1 in **Table 2-2**.

The mesh sensitivity study presented in **Fig. 2-16** shows that for both techniques, the predictions of lip height are very sensitive and the prediction of crater dimensions are relatively insensitive to the element size. Thus accurate predictions of lip height are mitigated by the use of a very fine mesh, at a significant computational cost.

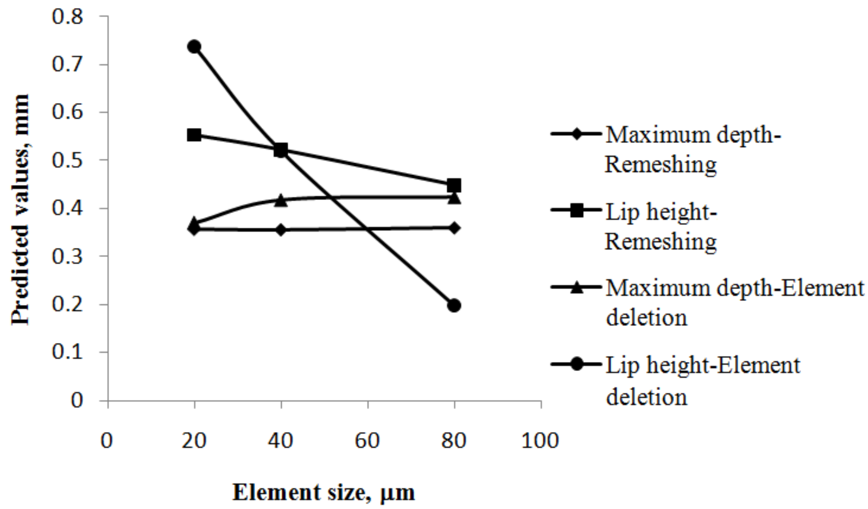

Fig. 2-16. The variation of maximum depth of the crater and the lip height versus element size for both adaptive remeshing and element deletion techniques. Data shown corresponds to data point 5 in **Table 2-2**.

2.6 Summary and conclusions

A comparison of measured particle rebound kinematics and crater volumes with those simulated by finite element methods, for impacts of a rhomboidal particle with an angularity of 60° on copper targets revealed good agreement for both backward and forward rotating particles. The capability of finite element models to predict chip separation and material pile-up make them advantageous over a previous rigid-plastic model. Between the two techniques implemented in the finite element models to deal with the large deformation problem and damage modeling, the element deletion technique matched the experimental results better than the remeshing procedure, for both backward and forward rotating particles. Chip separation was also well simulated using this technique, which also provided a fair prediction of the rebound kinematics of backward rotating particles. Remeshing also proved to be promising for the simulation of forward rotating particles, but it is likely that a damage model needs to be implemented in order for it to enjoy similar success for the simulation backward rotating particles.

The use of finite element modeling with element deletion, allowing for simulation of chip separation and material pile-up can simulate some of the fundamental mechanisms of solid particle erosion of ductile erosive systems by angular particles. However, the dependency of this method on a nonphysical parameter as a criterion for element removal resulted in unsatisfactory results for penetration of blunt particles. Therefore, this method is likely to not be robust enough for the prediction of impacts of more realistic randomly shaped three dimensional particles. To address this, the next chapter, will explore the use of the meshless smoothed particle hydrodynamics (SPH) method that can better accommodate large deformations and that does not rely on any nonphysical parameters.

Chapter 3 Smoothed Particle Hydrodynamics Modeling of Single Particle Impact

3.1 Introduction

The results in **Chapter 2** showed that despite the overall acceptable performance of a Lagrangian FE model based on element deletion to model single particle two-dimensional impacts, this approach still suffers from some deficiencies. The shortcomings are mostly related to modeling the large deformations resulting from high speed impact with ductile materials which can distort the fixed connectivity mesh. Incorporation of element deletion and remeshing can improve the performance; however itnevertheless requires the adjustment a nonphysical parameter as a criterion for element deletion. This likely hinders its application to more general multi-particle modeling of solid particle erosion phenomena that will involve impacts of irregular three dimensional particles.

This chapter investigates the ability of smoothed particle hydrodynamics (SPH), a meshless numerical method, to model the single impacts of angular particles, thus providing a basis for multi-particle simulations of solid particle erosion phenomena. Most of the material in this chapter has been published in [73].

3.2 The smoothed particle hydrodynamics (SPH) method

Meshless particle methods in which the continuum is discretized by only a set of nodal points without any mesh constraints have also been proposed in order to alleviate problems with distorted finite elements. One of the earliest mesh free methods in computational mechanics is the smoothed particle hydrodynamics (SPH). This method was first introduced by Lucy [74] and Gingold and Monaghan [75] to study the formation and evolution of galaxies. Since the movement of these particles resemble a liquid or gas flow, classical Newtonian hydrodynamics can be used to track their movement. Soon after its development, SPH was widely adopted as an efficient and powerful technique to solve applied mechanics problems. Therefore, the term ‘hydrodynamics’ in SPH can more accurately be replaced with mechanics when it is applied to other branches of mechanics rather than hydrodynamics [76]. The SPH particles carry material properties and can move relative to each other according to the governing conservation equations. Thus, the mesh tangling and element distortion problems encountered in large deformation problems with grid-based finite element methods can be avoided.

The SPH formulation relies on the integral approximation or kernel approximation of a field function f with a function $< f >$ given by [77]:

$$\langle f(\mathbf{x}) \rangle = \int_{\Omega} f(\mathbf{x}') W(\mathbf{x} - \mathbf{x}', l) d\mathbf{x}' \tag{3-1}$$

where W is the smoothing kernel function, a centrally peaked function [78], and Ω is the domain of integration. The influence domain for the smoothing function W is a sphere of radius $2l$. The vector $\mathbf{x}'$ defines the position of all the points in the influence domain. Therefore, when the value of the field function is calculated at a specific $\mathbf{x}$, the integration is localized over the influence domain of the smoothing function. The continuous integral representation expressed in equation (1) can be converted to discretized summations over all the arbitrarily distributed particles in the influence domain. This process is often referred to as a ‘particle approximation’ of the field functions. If there are N particles within the influence domain of the smoothing function W for the particle i, located at $\mathbf{x}_i$, the particle approximation for $\langle f(\mathbf{x}) \rangle$ can be written as [77]:

$$\langle f(\mathbf{x}_i) \rangle = \sum_{j=1}^{N} \frac{m_j}{\rho_j} f(\mathbf{x}_i) W(\mathbf{x}_i - \mathbf{x}_j, l) \tag{3-2}$$

where m_j and ρ_j are the mass and density of particle j ($=1, 2, ..., N$), respectively

The particle approximation can be extended for the derivatives and gradient of the field functions. These formulations can be used to develop the discrete form of the conservation equations as follows [77]:

Conservation of mass: $$\frac{\partial \rho_i}{\partial t} = \sum_{j=1}^{N} m_j v_{ij} \frac{\partial W_{ij}}{\partial x_i} \tag{3-3}$$

Conservation of momentum: $\frac{\partial v_i}{\partial t} = \sum_{j=1}^{N} m_j \left(\frac{\sigma_i}{\rho_i^2} + \frac{\sigma_j}{\rho_j^2} \right) \frac{\partial W_{ij}}{\partial x_i}$ (3-4)

Conservation of energy: $\frac{\partial u_i}{\partial t} = \sum_{j=1}^{N} m_j \frac{\sigma_i \sigma_j}{\rho_i \rho_j} v_{ij} \frac{\partial W_{ij}}{\partial x_i}$ (3-5)

where $W_{ij} = W(\mathbf{x}_j - \mathbf{x}_i, l)$, σ_i and σ_j are components of stress tensor for particles i and j, respectively, and v_{ij} is the component of the relative velocity vector between particle i and j. The conservation equations are equivalent to terms expressing the inter-particle forces [78].

The above standard SPH formulations for the conservation equations give incorrect results for particles located at boundaries, due to the lack of neighbours [79]. A renormalization formulation has been proposed to correct this deficiency [80], [81]. This formulation, employed in the present work, improves the SPH method consistency (order 1), giving the exact solution when the field function is linear. Therefore, it provides a better approximation at boundaries and also when the particles are irregularly disturbed.

The SPH formulation can also suffer from instability under tensile loads which may result in the clustering of SPH particles [82]. This may manifest itself as an unexpected fragmentation during a plastic deformation process [82], [83]. The present SPH analyses were performed using LS-DYNA 971 (Livermore Software Technology Corporation, Livermore, CA, USA) which does not provide an advanced solution to the problem of instability [79]. The possible occurrence of tensile instability during the present simulations and their effect on the results are discussed in **Section 3.5.4**.

3.3 Experiments

Single angular particle impact experiments were performed on 3.17 mm thick Al6061-T6 bar, whose properties and static tensile stress-strain curve can be found in **Table 3-1** and **Fig. 3-1**, respectively, in order to identify dominant erosion mechanisms and to verify the SPH numerical model. From this point forward, Al6061-T6 was utilized as the target material instead of OHC copper (**Chapter 2**) because it was found that it exhibited a larger amount of locally strained raised material. Since the knocking off of these raised lips that are extruded adjacent to the impact craters is one of the major mechanisms of solid particle erosion [31] that has not been previously been modeled, it was felt that this was a better candidate material to model. The rhomboid particle geometry proposed by Papini and Spelt [29] and shown in **Fig. 2-1** was used in all experiments. Particles with angularity $A = 45^\circ$ and 60° having h = 4.75 and 5.78 mm, respectively, were fabricated from heat-treated AISI A2 tool steel. The particle's thickness out of the plane of **Fig. 2-1** was 3.20 mm, and their density was 7800 kg/m^3. The hardness of the particles (750 Brinell) was sufficiently higher than Al6061-T6 (90 Brinell), to allow for the assumption of a non-deformable particle. A visual inspection of the impacting particle's shape after the impacts confirmed that there was no permanent deformation.

The specially designed rectangular bore gas gun (**Fig. 2-2**) described in **Section 2.2** was used to launch the particles. The gas gun utilized a rectangular sabot in which the angular particles were kept in a specific orientation while being accelerated, in order to ensure that the impacts occurred in a single plane. The nitrogen gas pressure was varied in the range of 200 to 800 kPa to regulate the incident velocity v_i in the range of 29 to 88 m/s. The angle of target with respect to the gas gun barrel was varied to study the impact at different sets of impact angles (α_i) and initial orientations (θ_i) in the range of $0°$ to 47° and 43° to 90°, respectively, as shown in **Table 3-2**. For all the measurements of crater dimensions and particle velocity, the same procedures explained in **Section 2.2** were followed.

Table 3-1 Material properties of Al6061-T6 [84]

Material properties	Symbol	Value
Density	ρ	2800 kg/m^3
Shear modulus	G	26 GPa
Poisson's ratio	ν	0.33
Tensile failure strain	FS	0.16
Melting temperature	T_m	925 K
Specific heat	C_p	885 J/(kg.K)
Hardness	BHN	90

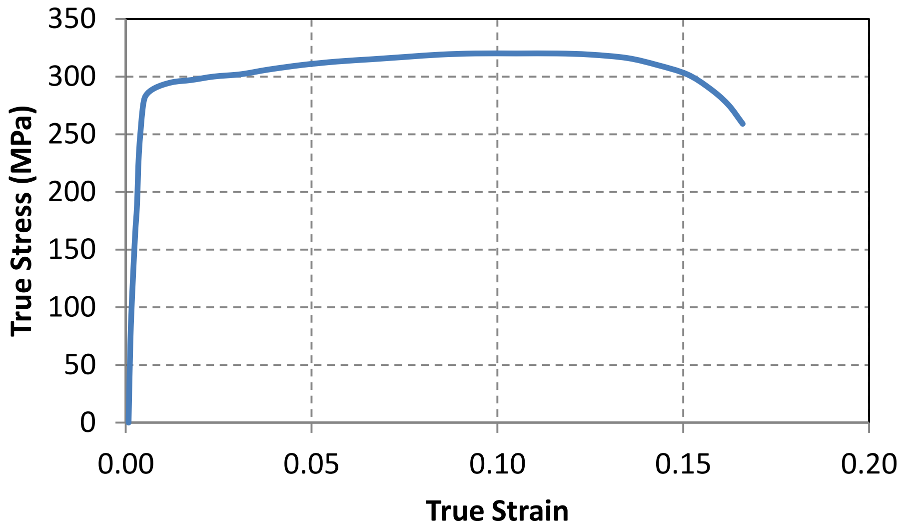

Fig. 3-1. Static engineering stress vs. engineering strain in simple tension of AL6061-T6 [85].

Table 3-2 Incident parameters and resulting measured and predicted crater depths and maximum lip height. Predicted results utilized the Cowper-Symonds strain rate dependency model.

Data Point	Incident Parameters				Measured		SPH Predicted		Deformation Mechanism
	A (deg.)	v_i (m/s)	θ_i (deg.)	α_i (deg.)	d_{max} (μm)	h_{lip} (μm)	d_{max} (μm)	h_{lip} (μm)	
1	45	29	0	90	114	47	142	34	Pile-up formation
2	45	46	0	90	212	83	243	61	Pile-up formation
3	45	57	0	90	257	95	317	87	Pile-up formation
4	45	66	0	90	311	115	355	102	Pile-up formation
5	45	88	0	90	448	163	466	152	Pile-up formation
6	45	45	14	76	215	203	261	136	Pile-up formation
7	45	44	25	75	146	320	191	281	Pile-up formation
8	45	45	39	51	75		123		Chip separation
9	60	24	0	90	187	84	221	55	Pile-up formation
10	60	39	0	90	325	138	395	105	Pile-up formation
11	60	50	0	90	434	183	493	134	Pile-up formation
12	60	61	0	90	539	214	590	177	Pile-up formation
13	60	47	11	79	444	275	459	221	Pile-up formation
14	60	43	20	70	405	350	411	309	Pile-up formation
15	60	31	47	43	103		155		Chip separation
16	60	44	47	43	156		173		Chip separation

3.4 Model description

SPH-based models of the single angular particle impacts described in **Section 3-2** were constructed. These models allowed the simulation of the entire impact event, including the crater formation, the material pile-up at the edge of the crater, and, if it occurred, the machining and separation of a chip of material.

3.4.1 Model Geometry and Boundary Conditions

To reduce the model size and the computation time, a number of simplifying assumptions were made. As shown in **Fig. 3-2**, only the area around the impact site where the large deformation was expected to occur was modeled with SPH particles, and the rest of the model, including the rigid particle, was discretized using eight-node solid hexahedron elements having one point of integration (ELFORM 1). Reduced integration elements were preferred to save computational time. The SPH and FE models were coupled together through the "Contact_Tied_Nodes_to_Surface" command in LS-DYNA. The material pile-up in planes parallel to the wider plane of the particle was neglected. Therefore, a thin slice model with a thickness of 0.3 mm was utilized to model the in-plane single impact, as shown in **Fig. 3-2**. The two sides of this slice were constrained for out-of-plane displacement and rotation. All other boundaries of the target were fully constrained.

The computation time is a nonlinear function of the number of SPH particles in the model [86]. The computation time corresponding to the SPH search algorithm which locates the nearest neighbours of each particle, increases with the number of SPH particles as $N \log N$. Therefore, the number of SPH particles utilized in the model must be carefully chosen to make sure that the computation time is not too large without significantly affecting the accuracy of the model. A sensitivity study was performed to investigate the dependency of the numerical results on the SPH particle spacing for two cases. For particles that penetrate into the surface and displace the material to the edge of the crater and form a pile-up, the predicted crater depth and the lip height only changed 1% and 7%, respectively, when the SPH particle spacing was varied from 20- 60 μm. Therefore, for these cases, a spacing of 60 μm was chosen for SPH particles. This led to a model with 6834 SPH particles and 27848 solid elements. For particles that machine and remove a chip of material, the predicted crater depth was very sensitive to the particle spacing and a change of more than 40% in crater depth was observed when the SPH particle spacing was varied from 20 to 60 μm. However, there was only a change of 5%, when the particle spacing was varied from 20 to 10 μm. Therefore, the distance between the SPH particles and the size of FE elements were chosen as 20 μm for these cases. To ensure convergence of the contact algorithm, the impacting particle's FE mesh was chosen to be coarser than the SPH particle spacing in the target.

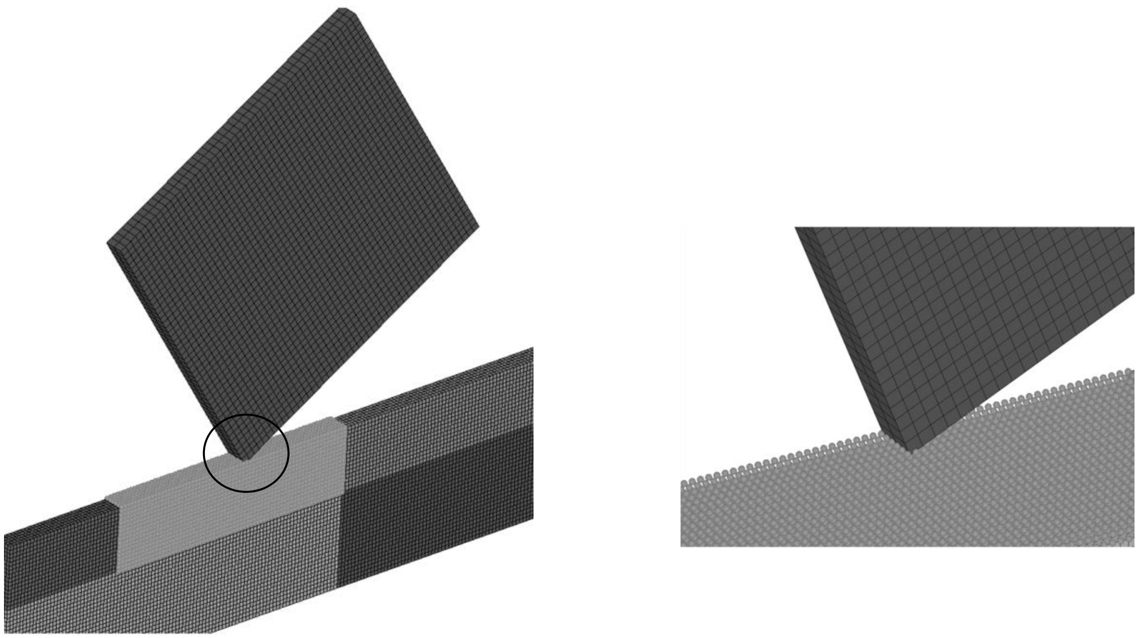

(a) (b)

Fig. 3-2. (a) Coupled FE/SPH model of particle and target, (b) Enlarged view of impacting particle and SPH particles.

3.4.2 Contact definition

The contact between the FE representation of the impacting particle and the SPH target was defined using the Contact_Automatic_Nodes_to_Surface and a Coulomb friction model. Following the approach of previous investigators [87], the friction coefficient was adjusted to 0.1 in order to obtain a good fit between numerical and experimental results.

3.4.3 Constitutive equation

Similar to the FE modeling presented in **Chapter 2**, the target was modeled using a Johnson-Cook constitutive equation [67] (**Equation 2-1**), which can account for strain rate hardening and thermal softening, both of which have been found to affect the erosion behaviour of materials [88], [89]. For high strain rates, it can be assumed that the heat generated due to plastic work causes an increase in the deforming material temperature under an adiabatic heating condition. Most of the mechanical work expended during a plastic deformation process in metals is converted into heat, while the remainder is stored in the material microstructure [90]. LS-DYNA assumes that 90% of the mechanical work is converted into heat which is consistent with what proposed by Dieter in [91].; therefore, the temperature change in **Equation 2-3** becomes:

$$T_{\mathrm{inst}} - T_{\mathrm{ref}} = \frac{0.9W_p}{\rho C_p} \tag{3-6}$$

where W_p is the plastic work, and ρ and C_p are the density and the specific heat of the target material, respectively. Here, T_{ref} was considered to be 296 K.

The LS-DYNA manual was not clear about the possibility of calculating the thermal softening term in the Johnson-Cook material model using a structural only analysis, i.e. without the need for using a coupled structural-thermal analysis. To explore this possibility, a survey of the literature was performed, and some simple structural and coupled structural-thermal LS-DYNA runs were compared. The results, summarized in **Appendix A.3** clearly show that thermal softening can be implemented into the structural analyses, provided adiabatic conditions with no heat conduction are assumed. The temperature history of each element can be requested in the output, and the temperature is updated and applied to the appropriate term in the Johnson-Cook equation as the plastic work is converted to heat. However, it should be noted that in a structural analysis, any assigned nodal temperatures are ignored by LS-DYNA. The initial temperature in a structural analysis that considers thermal softening is the same as the reference temperature in the Johnson-Cook input card itself. In the present case, since the initial temperature was the same as the reference temperature (i.e. room temperature), a structural only analysis is appropriate. For experiments performed at temperatures different than the reference, a coupled analysis would be required.

A number of different Johnson-Cook parameters for Al6061-T6 have been proposed in the literature (**Table 3-3**). The differences between these parameters are likely as a result of experiments performed at different strains, strain rates and temperatures. For the present work, the set of values proposed by Dabboussi and Nemes [92] were used, since they gave the best agreement between experimental and numerical results in the present work. The parameter *C* was set equal to zero, since, as is discussed in **Section 3.4.4**, the Cowper-Symonds strain rate model was used instead.

Although the impact velocities are relatively low in the present study, and changes in density brought about by shock compression are not expected to be significant, the implementation of the Johnson-Cook material model in LS-DYNA nevertheless requires an equation of state (EOS). In the present work, the Gruneisen EOS was used to define the relation between the pressure, *p*, and the rate of density change, $\mu = \frac{\rho_{inst}}{\rho_i} - 1$, where ρ_i and ρ_{inst} are the initial and instantaneous densities, respectively [93]. For compression, the EOS is

$$p = \frac{\rho_i v_{\text{sound}}^2 \mu \left[1 + \left(1 - \frac{\gamma_0}{2}\right)\mu\right]}{\left[1 - \left(S_1 - 2\right)\mu\right]} \tag{3-7}$$

and for tension, the EOS is

$$p = \rho_i v_{\text{sound}}^2 \mu \tag{3-8}$$

where v_{sound} is the bulk speed of sound in the material, S_1 is the slope of the shock velocity versus material velocity curve, and γ_0 is the Gruneisen constant. The Gruneisen EOS parameters used for Al6061-T6, i.e. ρ_0, v_{sound}, S_1 and γ_0 were taken as 2800, 5240 m/s, 1.4 and 1.97, respectively [84].

Table 3-3 Johnson-Cook Parameters for Al6061-T6 from the literature

Johnson-Cook parameters	Split Hopkinson pressure bar (shear) [92]	Taylor impact specimen [94]	Split Hopkinson pressure bar (compression) [95]
σ_0 (MPa)	335	164	324
B (MPa)	85	211	114
c	0.012	0.00197	0.002
n	0.11	0.465	0.42
m	1	1.419	1.34

3.4.4 Strain rate dependency

It has been reported that the strain rate sensitivity of Al6061-T6 increases drastically at strain rates in excess of 10^3 s^{-1} [95]. The Johnson-Cook model, which performs well for low strain rates [96], cannot account for such a dramatic change in the behaviour of Al6061-T6 at high strain rates. Since the angular particle impacts considered in the present study result in strain rates on the order of 10^5 s^{-1}, the Cowper-Symonds equation, which relates the yield stress under a quasi-static condition to the yield stress under a high strain rate dynamic condition, may be more appropriate [97]:

$$\frac{\sigma_{eff}}{\sigma_{\text{static}}} = 1 + \left(\frac{\dot{\varepsilon}_{eff}}{D}\right)^{1/P} \tag{3-9}$$

where σ_{eff} is the effective stress, $\dot{\varepsilon}_{eff}$ is the effective strain rate, σ_{static} is the static uniaxial yield stress, and D and P are constants which must be measured for a given material. For the present work, D = 6500 s^{-1} and P = 4 were assumed, based on the measurements by Cowper and Symonds.

3.4.5 Failure model

In order to model the cases in **Table 3-2** which involved a pure machining action of the particle, with chip separation and ejection, it was necessary to use a failure model. Guo and Yen [57] used a similar approach in their finite element simulations of high-speed machining of AISI

4340 steel. Here, the Johnson-Cook failure model was used which allows the reduction of the SPH particle stress to zero when the parameter F in the following equation equals 1 [68]:

$$F = \frac{\sum \Delta\varepsilon_{eff}^{p}}{\varepsilon^{f}} \tag{3-10}$$

where the failure strain, ε^{f}, is determined from the following equation:

$$\varepsilon^{f} = \left(D_1 + D_2 \exp\left[D_3 \frac{p}{\sigma_{eff}} \right] \right)(1 + D_4 \ln \dot{\varepsilon}_{eff})(1 + D_5 T^{*}) \tag{3-11}$$

in which p is the hydrostatic stress (pressure).

The constants D_i for Al6061-T6 which are taken from measurements performed using split Hopkinson pressure bar by Lesuer et al. are given in **Table 3-4** [95].

Table 3-4 Johnson-Cook failure model parameters for Al6061-T6 [95]

Johnson-Cook Parameters	D_1	D_2	D_3	D_4	D_5
Values	-0.77	1.45	-0.47	0	1.60

3.5 Results and discussion

3.5.1 Effect of impact angle and initial orientation on impact crater

Fig. 3-3 shows typical impacts that occurred using the square particles. It was observed that changes in impact angle and initial orientation changed the direction of particle tumbling, and the resulting deformation mechanism of the target. As has been previously reported in Refs [25], [26], [28–30] and **Chapter 2**, a pure machining resulting in the ejection of a chip of material from the surface is expected at some incident conditions, as shown in **Fig. 3-3**. In this case, the impact crater was relatively shallow with very little pile-up at the edges. In all other cases, target material was displaced to the edge of the much deeper crater in the form of a relatively high pile-up (**Figs. 3-2a** and **3-2b**). A similar behaviour was also observed in the impacts of the $A = 60^{\circ}$ particles (not shown).

The severity of surface displacement is heavily influenced by the strain or work hardening characteristics of the material [1]. Al6061-T6 has a low strain hardening capability, which results in a localization of the plastic deformation to the layers close to the crater surface [92], [98] as demonstrated dramatically in **Fig. 3-3b** which has a crater pile-up height which is almost as large as the penetration depth. Because the piled-up material is susceptible to being removed by subsequent impacts, it has important implications for the solid particle erosion behaviour of materials [21], [99]. For example, the lower pile-up height for the normal incidence impact of **Fig. 3-3a** when compared to the oblique impact in **Fig. 3-3b**, may be a contributing factor to the reported [100] decrease in erosion resistance of ductile materials at higher angles of attack.

3.5.2 Effect of strain rate dependency model

The SPH-predicted maximum penetration depth and pile-up height (**Fig. 2-6**) at various particle velocities (normal incidence) when using the Cowper-Symonds and Johnson-Cook strain rate relations are shown in **Figs. 3-3** and **3-4**, respectively, together with the corresponding measured quantities. The Cowper-Symonds strain rate model was better able to predict the crater depth for both A = 45° and A = 60° particles (3-24% difference between predicted and measured results). The Cowper-Symonds strain rate relation better predicted the pile-up height for A = 45° particle (7-27% difference between predicted and measured results). The prediction of the pile-up height for A = 60° particles was not as good, but was nevertheless acceptable (17-34% difference between predicted and measured results). Therefore, the Cowper-Symonds strain rate dependency was used in all further simulations.

3.5.3 Comparison of SPH model to experiments

Table 3-2 presents the SPH predicted results for crater parameters (using the Cowper-Symonds strain rate dependency) for different incident conditions, together with the experimentally measured quantities. Typical predicted and experimentally measured crater profiles are also shown in **Fig. 3-3**. For the cases in which the particles machined a chip of material to separation, only the predicted maximum crater depths were compared with experiments, since there was no pile-up formed. In all other cases, both the predicted maximum crater depths and pile-up heights were compared to experiments. The average percentage difference between predicted crater depths and pile-up heights were 21% and 20%, respectively. In all cases, the SPH model overestimated the depth of penetration and underestimated the pile-up height.

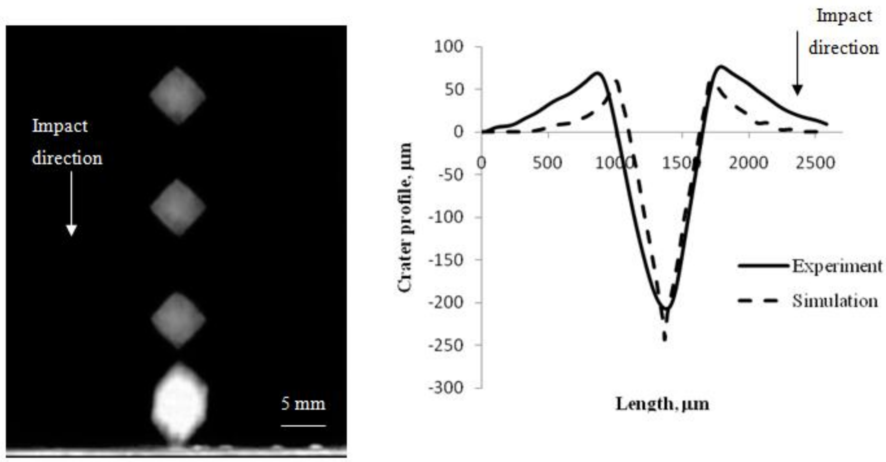

(a)

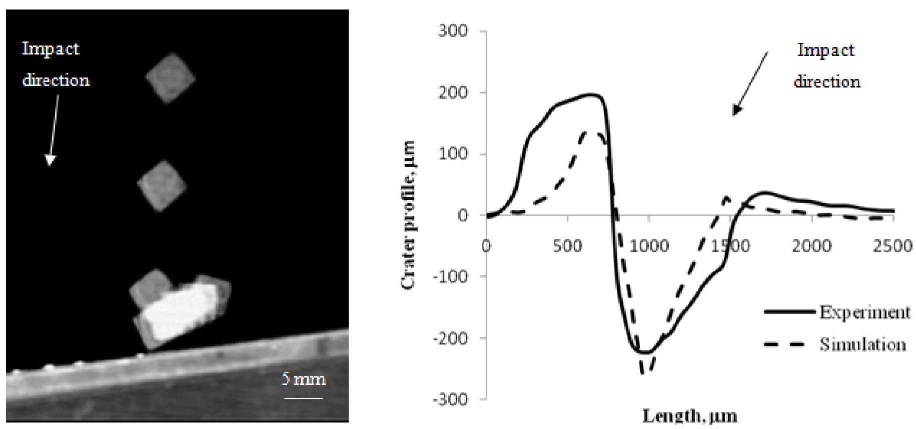

(b)

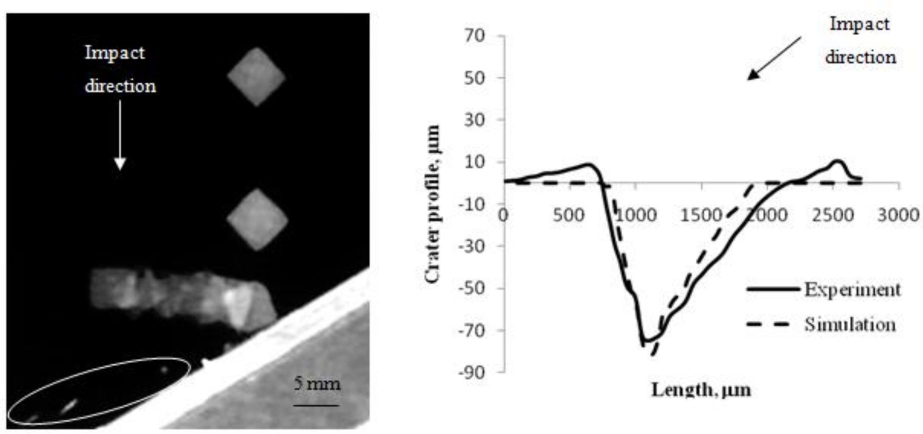

(c)

Fig. 3-3. Multiple exposures (left) and resulting measured and predicted impact craters (right) for the impact of square (A = 45°) particles: (a) data point 2, (b) data point 6 and (c) data point 8 in **Table 3-2**. In (c), multiple exposures of the ejected chip are shown in the white oval. Predicted results utilized the Cowper-Symonds strain rate dependency model.

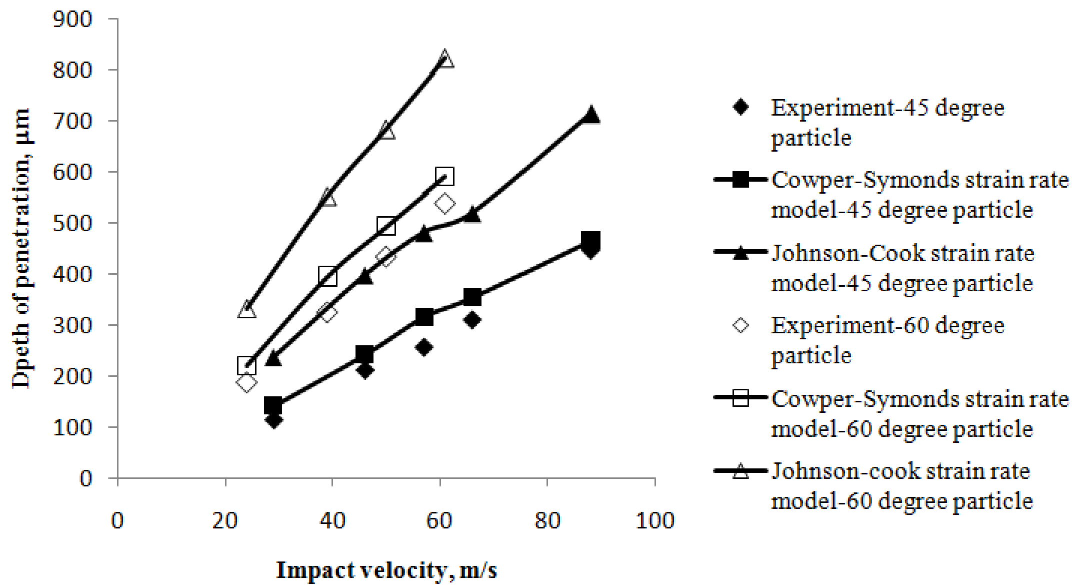

Fig. 3-4. SPH predicted and measured depth of penetration at various impact velocities at normal incidence for A = 45° and 60° particles using two strain rate dependency models.

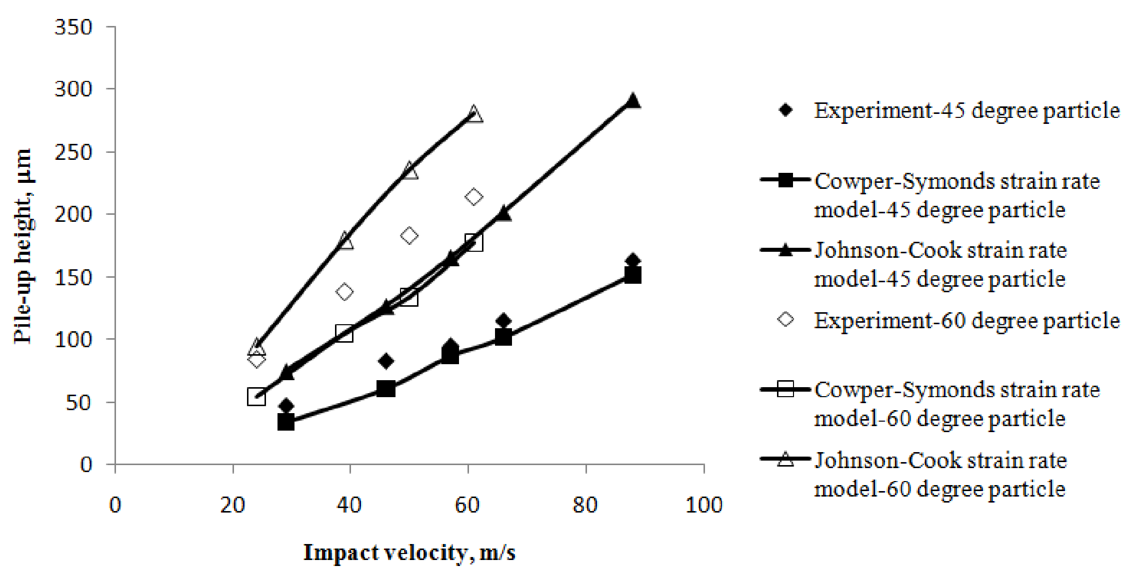

Fig. 3-5. SPH predicted and measured pile-up height at various impact velocities at normal incidence for A = 45° and 60° particles using two strain rate dependency models.

Fig. 3-6 shows that there was a good agreement between the SPH predicted and measured particle rebound velocities. The largest discrepancy was found in the cases when a chip of material was separated and removed from the surface (Data points 8, 15 and 16), i.e. the cases in which a failure model is required. The presently utilized failure model parameters were taken from the literature, and are valid for strain rates which are in the range of 10^{-4} to 10^{3} s^{-1}. It is possible that an optimization of these parameters for the present high strain rate impact (10^{5} s^{-1}) may significantly improve the accuracy.

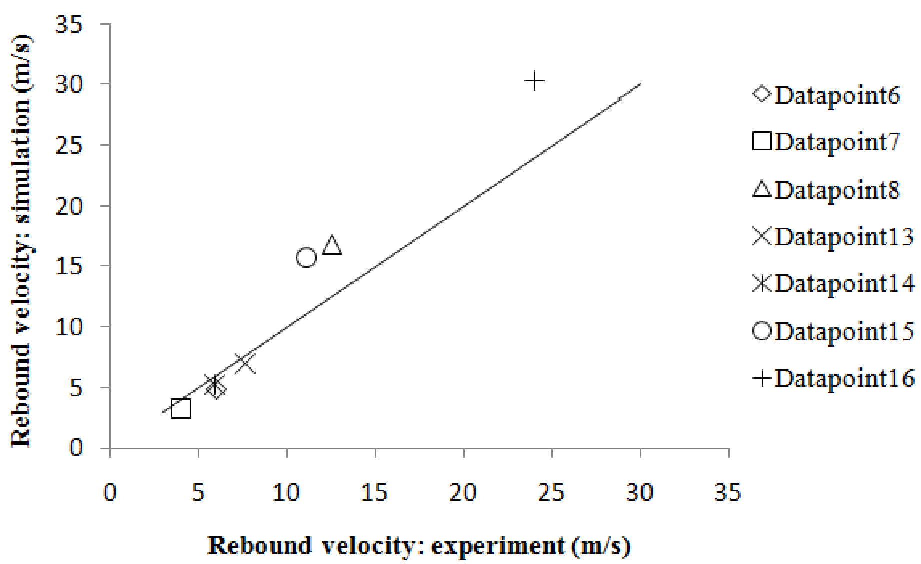

Fig. 3-6. SPH predicted and measured rebound velocity for various data points in **Table 3-2**. The solid line represents a perfect agreement between simulation and experiment.

Fig. 3-7 shows a SPH simulation for a typical impact in which a crater pile-up is formed. In contrast to previously utilized finite element analyses, presented in **Chapter 2** which resulted in the distortion of elements, the relative movement of the SPH particles allowed for the effective simulation of the large deformation and crater pile-up associated with the angular particle impact.

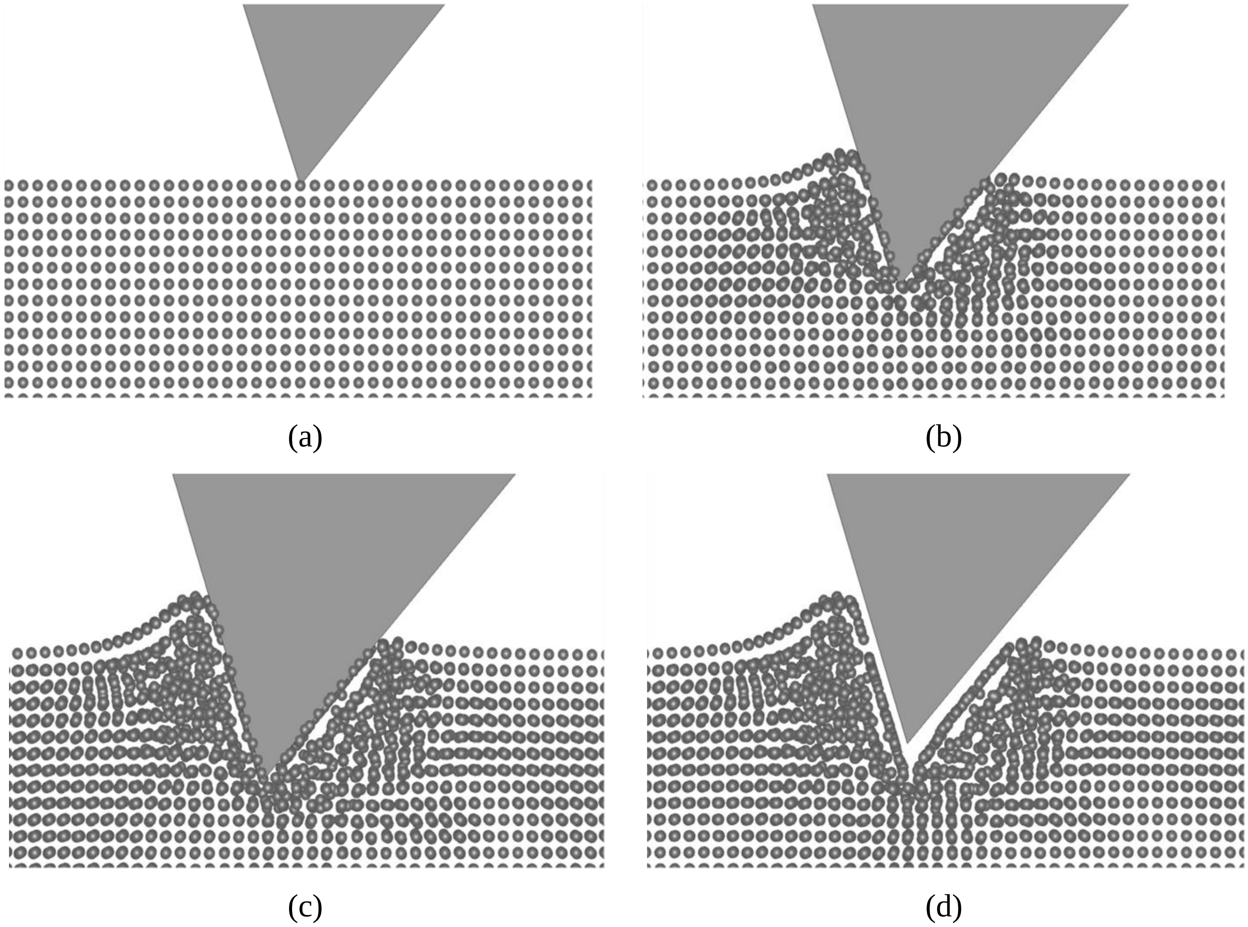

Fig. 3-7. SPH simulation of data point 13 in **Table 3-2**: (a) t = 0 (b) t = 10 μs (c) t = 20 μs (d) t = 40 μs.

Fig. 3-8 shows the simulation of an impacting square particle that resulted in a machined chip detachment. The formation and separation of machined chips in the SPH models are the result of the natural rearrangement of SPH particles and their simulated failure, according to the Johnson-Cook failure model.

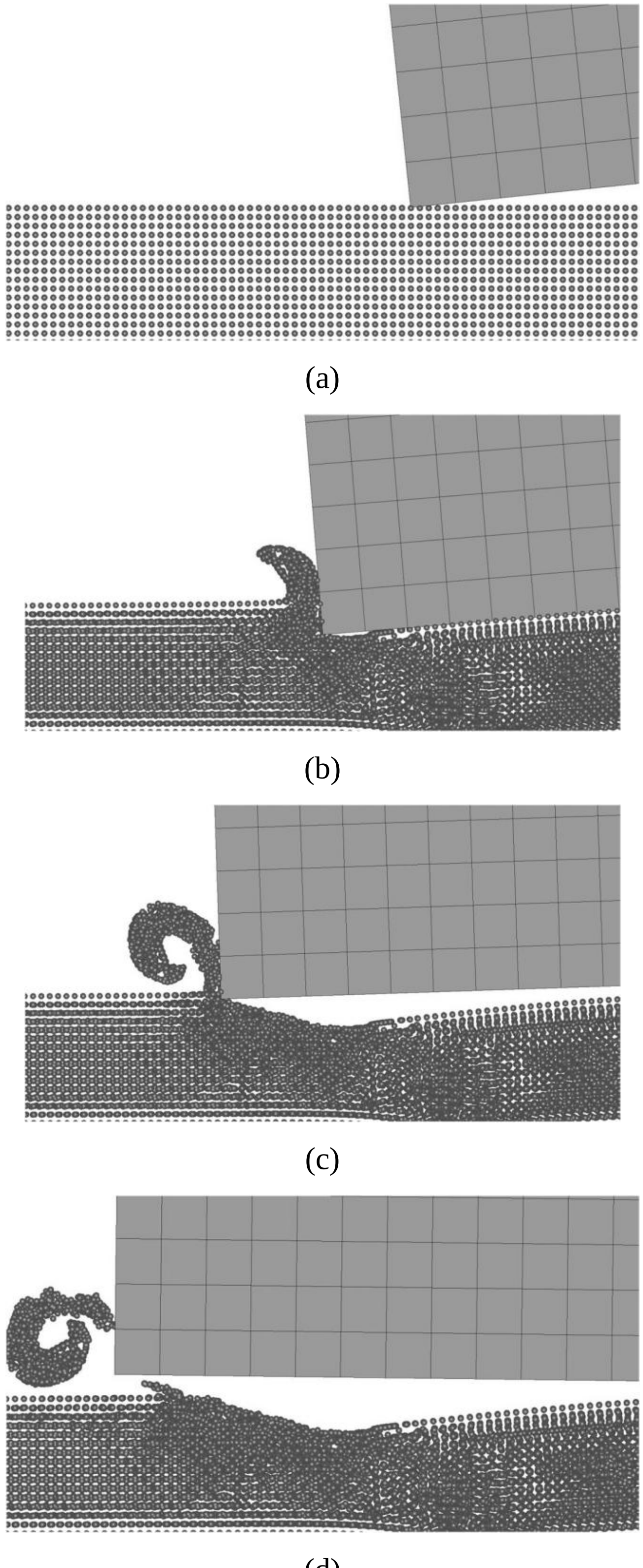

(a)

(b)

(c)

(d)

Fig. 3-8. Simulation of chip detachment from the surface (data point 8 in **Table 3-2**): (a) t=0 (b) t=5 μs (c) t=10 μs (d) t=15 μs.

3.5.4 The effect of tensile instability on the SPH results

As explained in **Section 3.2**, the SPH method sometimes suffers from a tensile instability. Of the two types of impacts occurring in the ductile erosive system presently studied, the ones in which material pile-up occurs (**Fig. 3-7**), are less likely to suffer from such an instability, since the material is mostly under compression with tensile stresses only induced locally around the tip of the particle. The impacts in which chip separation occurs involve a higher degree of tensile stress and are therefore more susceptible to the instability. Tracking the variations of the different types of energies during the simulation can be used to investigate if any artificial energy generated due to such instabilities exists in the simulation [83]. **Fig. 3-9** shows the histories of total, internal, kinetic and sliding contact energies for two typical data points (13 and 15 in **Table 3-2**). The kinetic energy includes both that of the particle and that of the target material. The total energy remained constant during the entire simulation, indicating the absence of any instability. Similar energy analyses were carried out for all the data points in **Table 3-2**, and no problems with instability were identified, regardless of whether the impacts resulted in chip separation or crater pile-up.

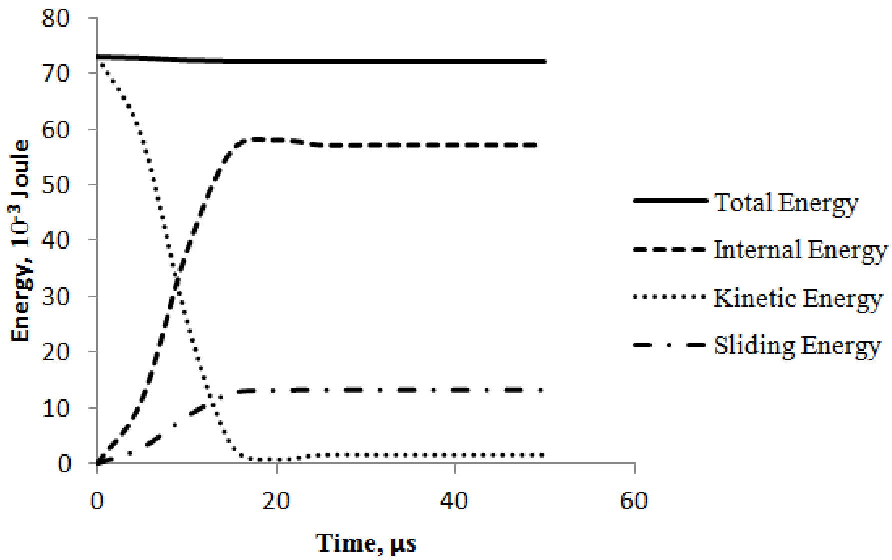

(a)

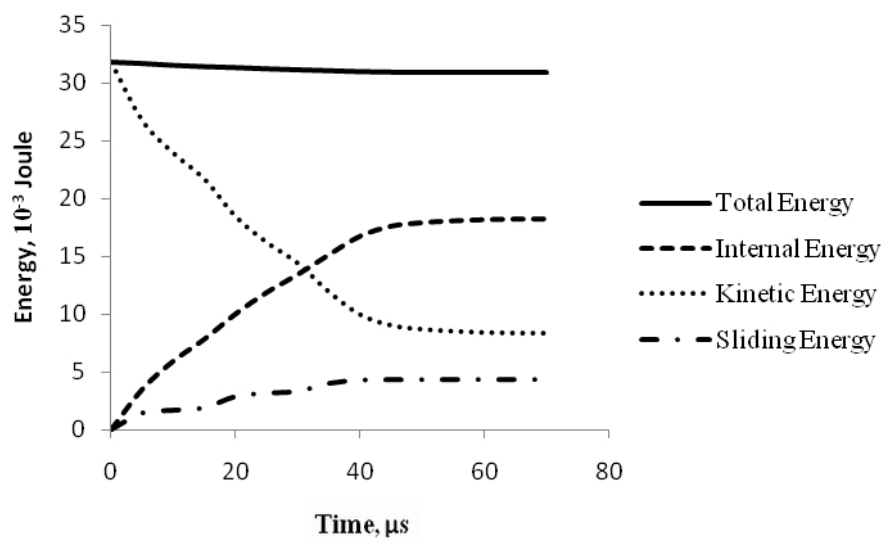

(b)

Fig 3-9. Variations of total, internal, kinetic and sliding energies during the simulation of the impact for (a) data point 13 and (b) data point 15 in **Table 3-2**.

3.6 Summary and conclusions

The behavior of Al6061-T6 under single particle impacts of angular particles was studied experimentally and numerically. In most cases, the target material was displaced to the edge of the craters, forming a pile-up. The large amount of piled-up material can be attributed to the low strain hardening of Al6061-T6, causing the material deformation to be localized around the impact site. Over a narrower range of incident parameters, the particles were observed to perform a pure machining of the surface, resulting in the ejection of a machined chip.

The SPH method was found to be an appropriate technique for simulating angular particle impact on ductile materials such as Al6061-T6. The results of the present study showed that the constitutive equation in the SPH formulation should be carefully selected based on the impact conditions. For the present conditions, the Cowper-Symonds strain rate equation performed much better than the Johnson-Cook. Using this model, the prediction of penetration depth, crater pile-up height and rebound velocity was found to be in good agreement with experimental results. The SPH methodology avoids the difficulties associated with the element distortions and tangling discussed in detail in **Chapter 2**, which are typical of finite element models of very large deformation problems. It also facilitated modeling material separation. This indicates that SPH might be utilized to study the solid particle erosion behaviour of wide variety of ductile materials. In the next chapter, a methodology to generate realistic three-dimensional abrasive particles for implementation into an SPH simulation will be developed. This methodology will be used in **Chapters 5 and 6** to investigate the appropriateness of the SPH technique for the modeling of material removal due to the impact of multiple particles with different angular shapes.

Chapter 4 Three Dimensional Representation of Abrasive Particle Samples for Numerical Modeling

4.1. Introduction

As discussed in **Section 1.3.2,** most previous models for particle impact and erosion were developed for spherical particles. This is despite the fact that in most actual particle impact processes, particles with irregular shape are present. In addition, the assumption of a single size particle in particle erosion modeling neglects the variation of sizes in a sample of particles.

Quantifying the effect of particle shape in erosion modeling has proven difficult. Despite the relative ease of implementing different particle shapes in numerical models such as finite element, a methodology for replicating realistic angular particle shapes in these simulations has remained elusive. These factors, together with the challenges of modeling the much higher target deformations resulting from angular particle impacts, has limited previous numerical investigations to the relatively simple case of erosion due to uniformly sized spherical particles. The results presented in **Chapter 3** showed that SPH is a promising tool to model the large deformation and displacement of the target material, as well as the chip separation from the surface. This chapter describes a novel methodology that allows the generation, for the use in an SPH simulation of erosion, of a sample of 3D irregular particle geometries that matches the size and shape distributions of a sample of actual aluminum oxide erodent powder.

4.2 Particle Shape Characterization

Aluminum oxide powder with a supplier specified nominal diameter of 150 μm was analyzed using an optical particle sizing system (Clemex PSA Research Unit, Clemex Technologies Inc., Longueuil, Quebec, Canada) in order to measure various parameters representing the shape and size of the particles. **Fig. 4-1** shows the measured circular diameter, D_{circular} , in-plane area, *Area,* and roundness, *R*, distributions of a sample containing 1347 particles. The circular diameter of an object, D_{circular}, is defined as:

$$D_{\text{circular}} = 2\sqrt{\frac{Area}{\pi}} \tag{4-1}$$

and the roundness, *R*, is calculated from in-plane measurements of *Area* and *Perimeter* according to:

$$R = \frac{4\pi Area}{Perimeter^2} \tag{4-2}$$

The rounder a particle is, the closer its roundness is to a value of 1, i.e. a circle has a roundness of 1. The measured average values (± standard deviation) of D_{circular}, *Area*, and *R* were 172 (± 55) μm, 29591 (± 12815) μm^2 and 0.61 (± 0.09), respectively. These parameters allow an approximately Gaussian distribution.

Since the optical particle size analyser only provided the information regarding the in-plane shape of the randomly oriented abrasive particles, the thickness (i.e. in the out of plane direction) distribution of the particles was measured using a non-contact profilometer (Nanovea ST400, Micro Photonics Inc., Allentown, PA, USA) and shown in **Fig. 4-1d,** which approximately follows a lognormal distribution. The average thickness of the particles was only 44.0 μm (±24), which was approximately one quarter of the average particle diameter. As can also be seen in **Fig. 4-2**, the particles were thus more of a flake-like shape. As discussed in [44], this feature distinguishes aluminum oxide particles from silicon carbide particles which also have an angular shape. The average mass of each alumina particle was also calculated by measuring the mass of three samples, each having an average of 756 particles, where the number of particles was counted using the optical particle size analyser. The average mass of each alumina particle was found to be 7.87×10^{-3} mg, which agrees reasonably well with the 5.21×10^{-3} mg value calculated using the measured average thickness and in-plane area.

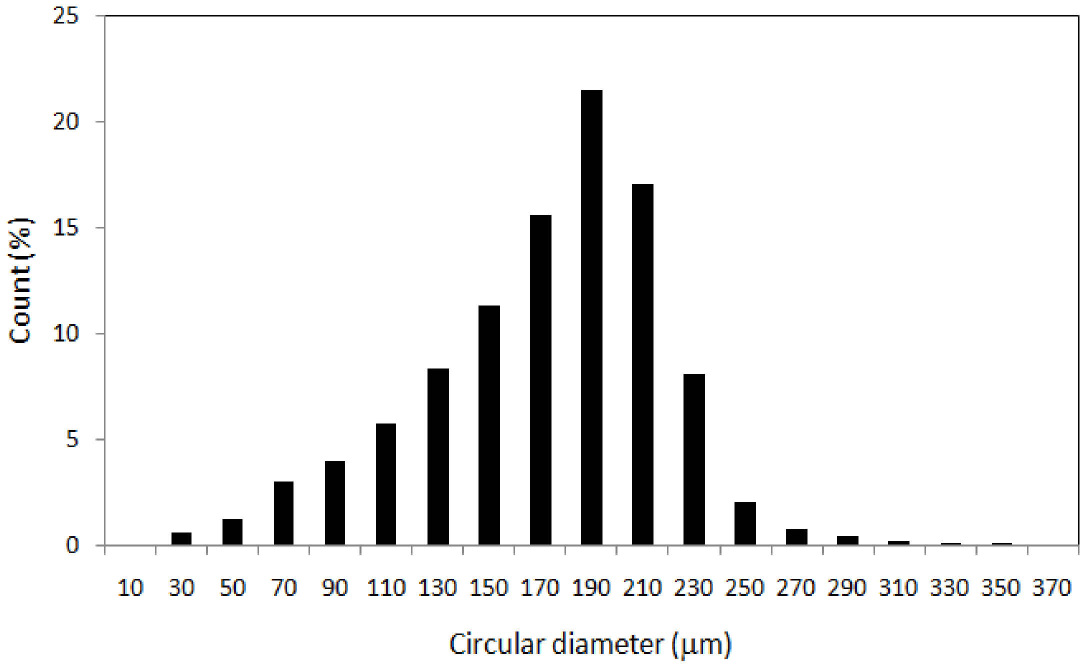

25
20
15
10
5
0
Count (%)
10 30 50 70 90 110 130 150 170 190 210 230 250 270 290 310 330 350 370
Circular diameter (μm)

(a)

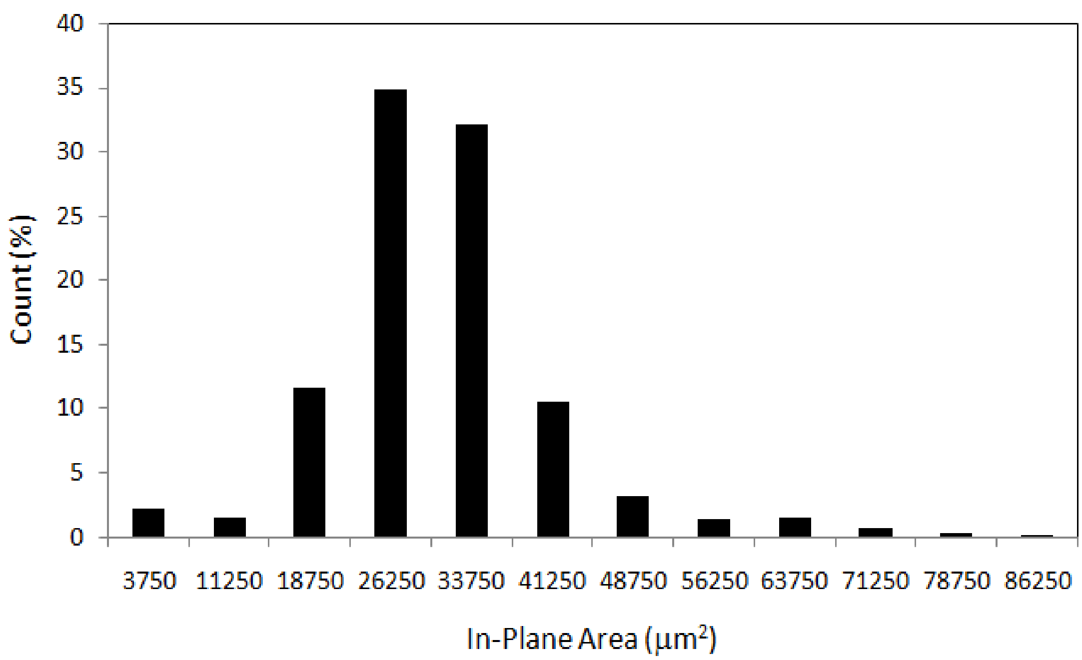

40
35
30
25
20
15
10
5
0
Count (%)
3750 11250 18750 26250 33750 41250 48750 56250 63750 71250 78750 86250
In-Plane Area (μm²)

(b)

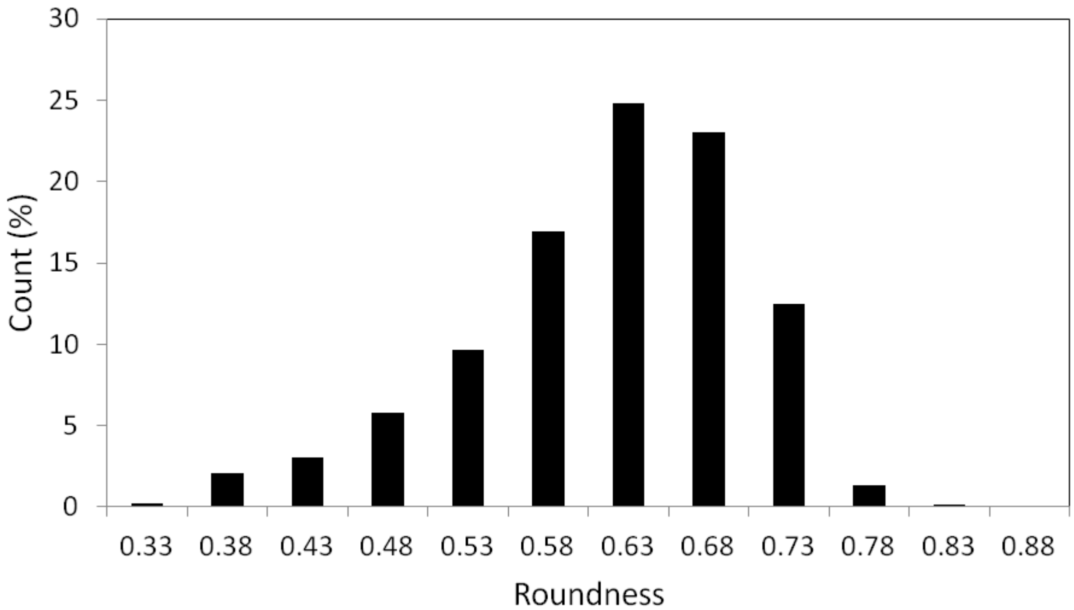

(c)

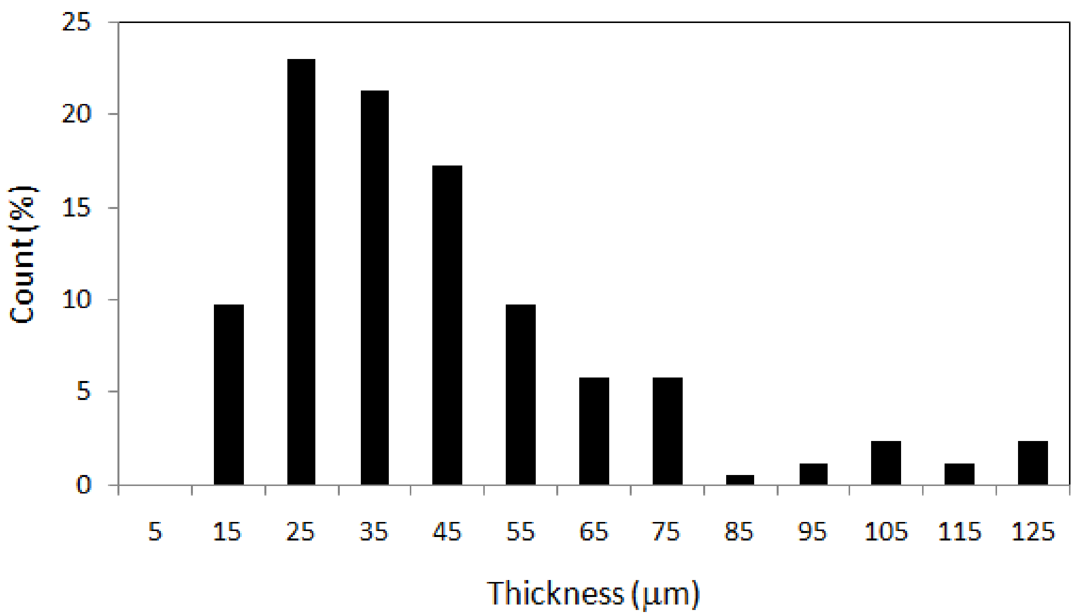

(d)

Fig. 4-1. Particle shape and size characterization: (a) circular diameter distribution, (b) in-plane area distribution, (c) roundness distribution and (d) out of plane thickness distribution.

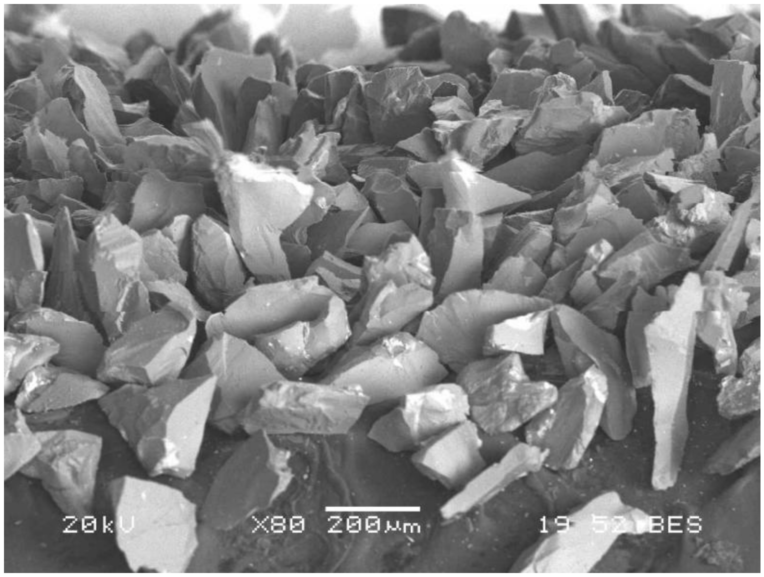

Fig. 4-2. Scanning electron micrograph of a sample of aluminum oxide particles.

4.3 Particle Modeling

The measured particle characteristics described in **Section 4.2** were used to generate a sample of six-faced 3D particles which had the same size and shape distribution as the actual particles. A code was written in MATLAB, presented in **Appendix A.1** which follows the following procedure to generate a modeled sample of particles:

(i) To generate a sample of N particles, N values for the particle in-plane area were chosen to follow the distribution shown in **Fig. 4-1b**.

(ii) A random value for the outer diameter, lying in the range measured by the particle analyser, was chosen. This outer diameter defined the smallest circle into which a given particle could fit completely.

(iii) Four points were used to define the vertices of the in-plane area of the particle. The x and y coordinates of three of them and the x coordinate of the fourth point were chosen at random to lie inside the boundary determined in (ii). The y coordinate of the fourth vertex was calculated such that the area of the resulting quadrilateral was equal to one of the N in-plane areas from (i). The quadrilateral was created by connecting the random points successively, ensuring that there was no intersection between the lines used to create the in-plane area.

(iv) The roundness of the quadrilateral from (iii) was calculated using equation (4-2) and attributed to one of the particle counts expected in the corresponding bin of roundness in **Fig. 1c**. When any of these bins were full, their corresponding particles generated afterwards were discarded.

(v) Steps (ii)-(iv) were repeated until *N* areas were generated that followed the distributions in **Figs. 4-1a**, **4-1b and 4-1c**.

(vi) The analysis of the particles using the optical profilometer (**Section 4.2**) indicated no correlation between the particle in-plane area and its thickness, and that they were roughly flake-shaped (**Fig. 4-2**), having an in plane dimension that was much larger than the thickness. As a first approximation, the particles were thus modeled each having a uniform thickness chosen at random such that the distribution in **Fig. 4-1d** was followed for the *N* particles.

(vii) Under the assumption that incident particles arrive to the surface in random orientations, a random rotation about the *x,y* and *z* axes was assigned to each of the generated 3D particle vertex coordinates. The resulting vertex coordinates of the *N* particles were then used to construct CAD representations of the particles, and implemented in the FE/SPH model.

The 2D projection of a sample of the generated particles is shown in **Fig. 4-3a,** which can be compared with the shape of actual alumina particles observed under the optical microscope (shown in **Fig. 4-3b**). It can be observed that the methodology presented above generated particles which have a very similar shape and size to the actual ones.

4.4 Summary and Conclusions

The proposed methodology was able to generate 3D particles that had similar shape and size distributions as the actual alumina abrasive particles they were meant to represent. In **Chapter 5**, these artificial particles will be implemented in an SPH model of a large number of non-overlapping particle impacts on an aluminum alloy in order to determine whether they will produce impact craters, and thus erosion mechanisms, matching those found in experiments.

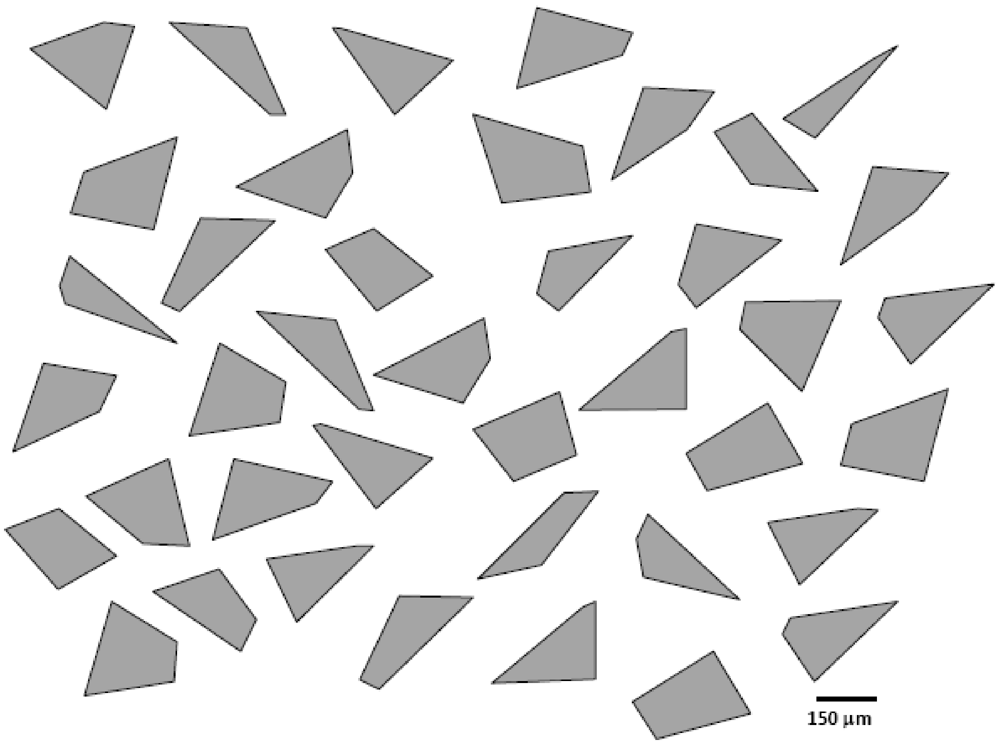

(a)

(b)

Fig. 4-3. Two dimensional geometry of: (a) modeled particles and (b) actual alumina particles.

Chapter 5 Numerical Simulation of Non-Coincident Impacts of 150-μm Alumina Particles on Al6061-T6

5.1 Introduction

It was demonstrated in **Chapter 3** that SPH is a promising tool to model the high speed impact of angular particles on ductile materials. The SPH formulation allows large deformation modeling without resorting to the use of nonphysical parameters such as those used in the Lagrangian FE models presented in **Chapter 2**. Therefore, it can be utilized to develop impact models of actual particles which have irregular shape with angular edges. In this chapter, the methodology presented in **Chapter 4** to generate modeled particles will be implemented into a coupled FE/SPH model of non-overlapping impacts. The distribution of the dimensions of the resulting simulated craters will be compared to those obtained experimentally. Finally, simulated material removal mechanisms will be identified, and compared to those commonly reported in the literature.

5.2 Experiments

5.2.1 Particle Impact Experiments

A commercial micro-blaster (MB 1005 Microblaster, Comco Inc., Burbank, CA, USA) was utilized to blast short bursts of the same150 μm nominal diameter aluminum oxide particles modelled in **Chapter 4** at 3.24 mm thick Al6061-T6 (90 BHN) targets, which were placed 30 mm away from the nozzle. Dry air at 300 kPa entered the micro-blaster, where it was mixed with the particles. The nozzle had an internal diameter of 1.5 mm and a length of 38.3 mm. To ensure that the surface flux was sufficiently low to allow for individual craters to be identified, a programmable shutter was used that allowed only a 0.1 s burst of particles to impact the surface. The mass flow rate of the particles was measured as 1.91 g/min. Prior to the blasting experiments, the target samples were polished to a roughness of Ra = 0.031 μm, so that single craters formed on the surface could be easily distinguished from the surrounding surface. As discussed in [101], the effect of mechanical polishing on the surface is limited to a layer of a few nanometers. Therefore, its effect on particle impact leading to the creation of craters with depth on the order of 3-37 μm is negligible. The blasting experiments were performed at two angles of impact: 90° (normal incidence) and 30°. The samples were sprayed with compressed air after each experiment to remove any dust and particles deposited on the surface.

Due to the diverging particle plume, there was a non-uniform particle flux, and the 4.72 mm diameter erosion scar produced by the 0.1s burst of impacting particles included craters formed by particles travelling at a wide range of velocities. Therefore, only the craters within a 1.5 x 1.5 mm square area centred in the scar where the maximum penetration occurred for normal and oblique incidence were considered in the crater measurements and for the simulations. The velocity and particle flux over this small area could be considered approximately constant, as was confirmed by the shadowgraphic measurements (**Section 5.2.2**). As has been previously noted for similar abrasive jets, there was no correlation between the particle size and the location within the jet [102].

5.2.2 Particle Velocity Measurement

Laser shadowgraphy measurements of particle velocity were performed using a double pulsed laser, which was passed through a high efficiency diffuser (Item No.: 1108417, Lavision GmbH, Goettingen, Germany), and placed directly opposite a high speed CCD camera (Imager Pro PlusX, Lavision GmbH, Goettingen, Germany) with a high magnification zoom lens (Navitar Zoom 12x, Navitar Inc., Rochester, New York, USA). The abrasive jet was incident in a plane parallel to the camera lens. The optics of the camera was such that the depth of focus defined the plane of particles on which the measurements were made. The focal plane was aligned to the centerline of the abrasive jet. The particles in this plane blocked the light incident to the camera, and appeared dark against the light background of the source. The laser was capable of producing two pulses of 1-ns duration as backlight illumination, so that two successive images of the particles in flight could be obtained by the double-frame CCD camera which was synchronized to the laser pulses. The delay between the two pulses was chosen to be 3 μs which assured that the two frames of each particle could be identified on the images. Computer software (Davis software, Lavision GmbH, Goettingen, Germany) was used to process and analyze the images and subsequently evaluate the sizes and velocities of the individual particles. More details of the shadowgraphy system and the measurement procedure can be found in [102]. The velocity of the particles was measured by taking 2000 double-frame images at 30 mm away from the nozzle exit, in the same 1.5×1.5 mm window centered on the center of the jet that was considered in the experiments (**Section 5.2.1**) and simulations (**Section 5.3.2**). The average number of particles detected in these images was approximately 560. The average particle velocity was 117 (± 6) m/s for the 300 kPa blasting pressure.

5.2.4 Blasted Surface Analysis

To characterize the damage done to the surface in the experiments of **Section 5.2.1**, the volume and depth of the impact craters, and the height of raised material adjacent to them were measured using an optical profilometer (Nanovea ST400, Micro Photonics Inc., Allentown, PA, USA) with a 130-μm maximum depth pen, having a depth accuracy of around 20 nm. Accurate measurement of the very small features required careful selection of the measurement pen, appropriate adjustment of the optical profilometer parameters and the correct leveling of the scanned surface. The distance between the pen and the surface, and the frequency rate of emission was adjusted to ensure that enough light intensity was reflected from the surface. The central 1.5 mm $\times$ 1.5 mm area (**Section 5.2.1**) of the blasted scar was scanned with a lateral resolution of 1 μm. The resulting profile was then imported into Professional 3D software (Nanovea ST400, Micro Photonics Inc., Allentown, PA, USA) and leveled before the crater and pile-up dimensions were measured.

Fig. 5-1 shows an optical profilometer scan of a typical surface of a specimen blasted at a particle velocity of 117 m/s and impact angle (with respect to the surface) of 30°. Despite the fact that there were a small number of overlapping impacts, **Fig. 5-1** shows that most of the impacts were sufficiently spaced to allow for individual crater volumes and pile-ups to be measured reliably.

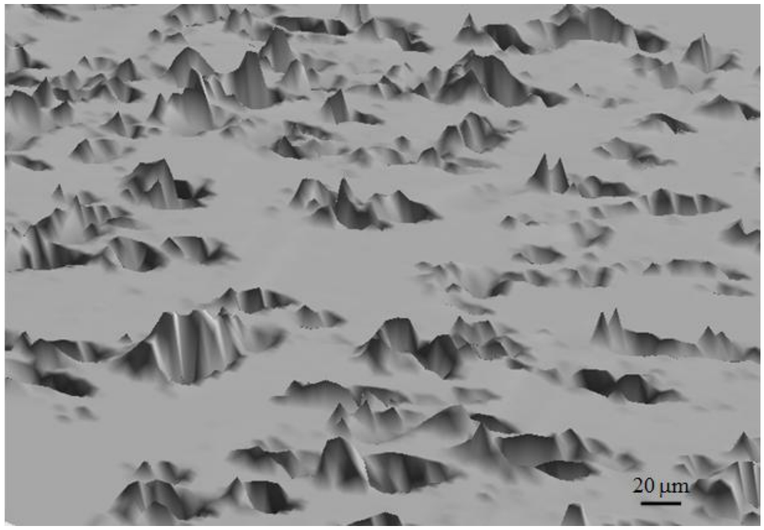

(a)

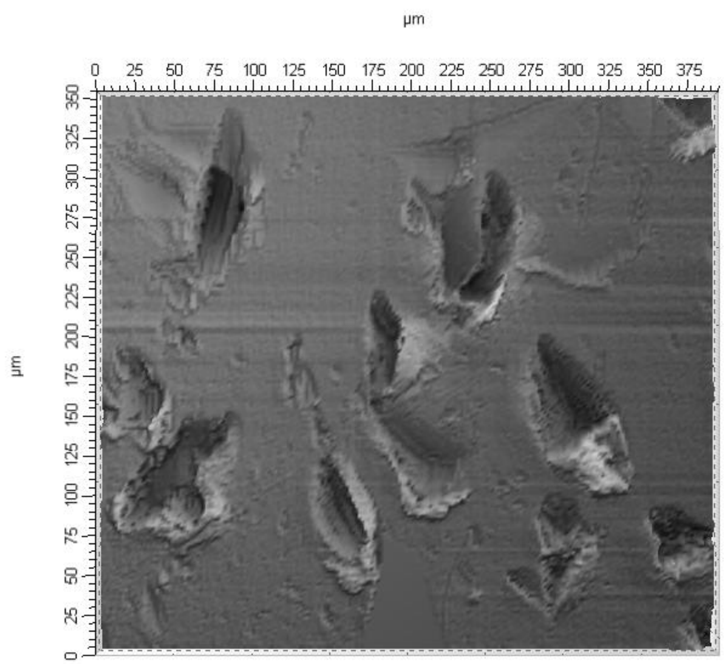

(b)

Fig. 5-1. Typical 3D optical profilometer scans of surface features after blasting Al6061-T6 with 150 µm alumina particles at 117 m/s at an impact angle of 30° : (a) Isometric view showing craters and pile-ups (b) Top view showing spacing of craters.

5.3 Modeling

A numerical model utilizing a smoothed particle hydrodynamics (SPH) representation of the target and FE particles was developed using LS-DYNA 971 (Livermore Software Technology Corporation, Livermore, CA, USA) and used to simulate the impact of a sample of the alumina particles on an Al6061-T6 target.

5.3.1 Implementation of representative particles in a FE/SPH model

The representative model of alumina particles was created using the methodology explained in **Chapter 4**. The CAD model of the particles were then constructed and implemented in the numerical model as single finite elements using an ANSYS Parametric Design Language (APDL) code presented in **Appendix A.2**. The number of particles developed in this manner, was N = 124, determined based on the average number of impacts visually counted in the 1.5 × 1.5 mm area described in **Section 5.2.1**. To ensure that the particle generation strategy was repeatable, three different sets of particle samples were generated, and their impact at 117 m/s was simulated in the FE/SPH model. The average crater volumes per launched particle which resulted from the simulation of the impact of these three sets of particles were within 6% of each other. This was taken as a strong indicator of the repeatability of the methodology, and that the 124 particles were sufficient to provide a meaningful representation of the particle distribution.

When implemented in the FE/SPH model (**Fig. 5-2**) that simulated their impact on the target, the particles were spaced randomly above the target and the distance between them was adjusted not to cause any interaction between the craters formed on the target. The same measured initial velocity presented in **Section 5.2.2** was assigned to the particles and all of them were launched simultaneously. No contact between the particles was defined. Each particle was meshed with only one finite element and considered to be non-deforming, since the hardness of aluminum oxide (1800 *Hv* [44]) is much higher than that of the aluminum alloy (118 *Hv* [103]). The density of alumina was defined as 3800 kg/m^3.

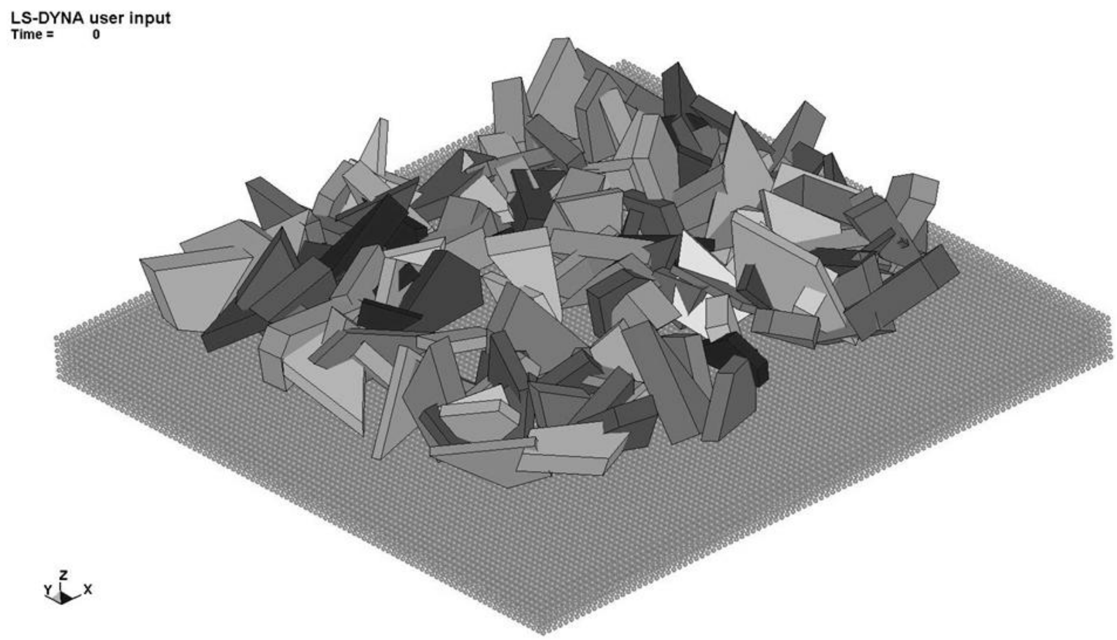

Fig. 5-2. Simulated particles meshed, each using a single finite element, impacting Al6061-T6 target simulated using SPH.

5.3.2 Target Modeling

The target Al6061-T6 material undergoes large deformations when impacted by angular particles. Therefore the target was modeled using SPH, a mesh-free method which uses particles without fixed connectivity in order to discretize the target (**Fig. 5-2)**. The default SPH formulation in LS-DYNA was utilized to develop the present model.

It has been previously recommended that uniform particle spacing be used in SPH modeling [78], rather than a biased SPH model which is finer at the impact site. The spacing between the SPH particles was set at 5 μm to compromise between the computational time, and the solution accuracy. The minimum spacing was largely determined by the pile-up dimensions formed at the edge of craters. For example, the average difference between the average pile-up height per crater when the particle spacing was reduced from 10 μm to 5 μm was 36%, whereas for crater depth, the average difference was only 8%. However, the computational time was around 20 times longer for a model with 5 μm particle spacing compared to a model with 10 μm particle spacing. It was found that a scaling factor of 0.2 applied to the initial time step computed by the code ensure that the plasticity algorithm for the material model converged in all cases. The constitutive equation and the failure model of the target material that were utilized in these simulations were the same as those described in **Sections 3.4.3**, **3.4.4** and **3.4.5**.

A plot of the total energy balance, i.e. the summation of the kinetic, internal and sliding energy (including friction) within the system was used to verify that significant artificial and numerical energy was not generated due to numerical instabilities. As explained in **Section 3.2**, these instabilities might occur when SPH particles are under tensile loadings. **Fig. 5-3** shows that the system energy typically decreased by only 3%, indicating that the SPH model was reliable enough for the present application.

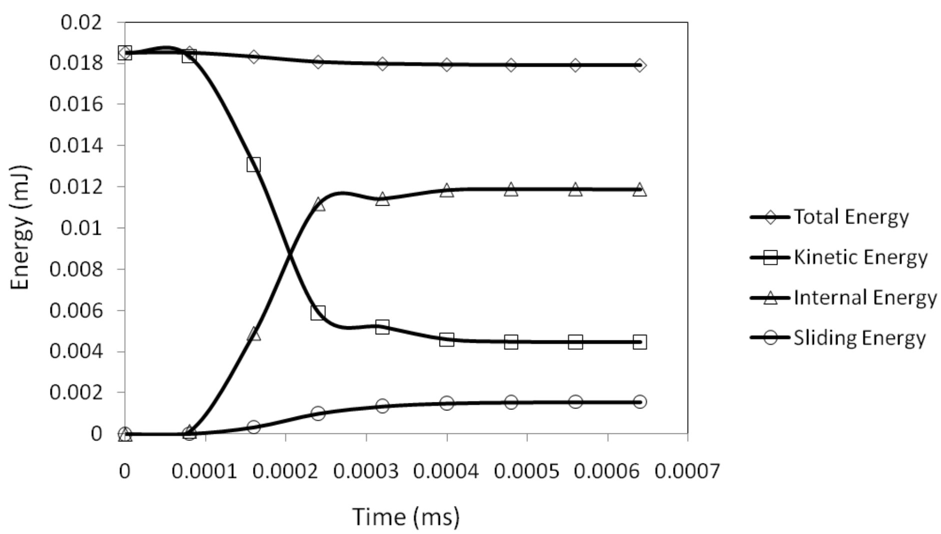

Fig. 5-3. Total, internal and kinetic energies during the simulation of the impact of a sample of 150-μm nominal diameter particles at 117 m/s incident normal to the surface.

5.4 Results and discussion

5.4.1 Crater and pile-up size distributions

Typical craters formed in the experiments and from the simulations are shown in **Fig. 5-4**. The simulated craters had similar shapes and sizes compared to the experimental findings. These triangular shape craters were also observed in the experimental work of Bellman and Levy [104] when aluminum alloys were blasted by angular silicon carbide particles. **Fig. 5-4b** shows that the numerical model was able to simulate the formation of pile-ups and lips at the edge of experimental craters (**Fig. 5-4a**).

The validity of the developed model for the generation of realistic particle geometries was studied by comparing the distribution of crater and pile-up sizes from the experiments and simulations. A code was written to extract the coordinates of the SPH particles that represented the deformed target surface at the impact sites. The coordinates were then imported into the same Professional 3D software that was used in **Section 5.2.4** to analyze the experimentally obtained surface, and the simulated crater and pile-up dimensions were extracted in the same manner.

5.4.2 Normal Incidence

Fig. 5-5 compares the measured and predicted crater and pile-up size distributions obtained from simulating three different modeled samples of alumina particles, each containing 124 particles, and three experimental repeats of the particles impacting normal to the surface at a velocity of 117 m/s (345 total individual impacts). The experimental and predicted distributions of all four measured parameters show the same general shape, although there are some discrepancies at some size intervals. **Fig. 5-6** shows that the averages of the experimental and predicted crater and pile-up dimensions were in very good agreement. Specifically, the differences between the average experimental and predicted crater volume, pile-up volume, crater depth, and pile-up height were 6%, 15%, 17% and 17%, respectively. These differences were all found to be statistically insignificant (t-test, $P > 0.05$).

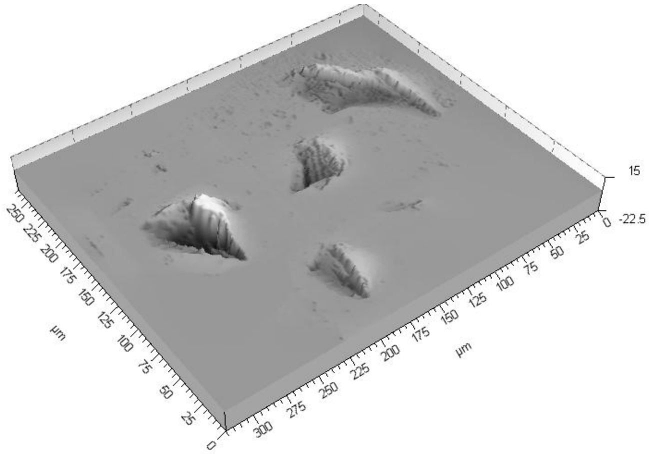

(a)

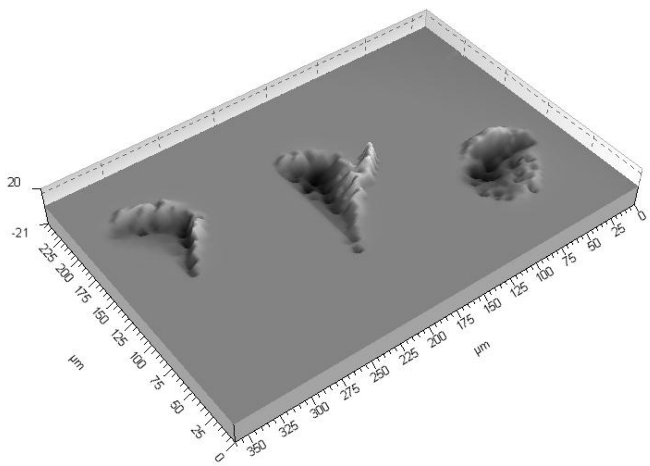

(b)

Fig. 5-4. Typical craters and pile-ups formed on the surface resulting from impacts at $\alpha = 30^{\circ}$ and $V = 117$ m/s: (a) experiment, (b) simulation.

Fig. 5-6a shows that the crater volume was much higher than the pile-up volume. As discussed by Sundararajan [37], [105], the impact energy of the particles leads to both bulk deformation underneath the crater and a localized plastically deformed volume at the crater edges which is significantly smaller than the crater volume. Therefore, most of the crater volume is generated by the bulk deformation rather than shear deformation near the surface. In addition, the low strain rate encountered during the final stages of the impact results in more bulk than localized deformation.

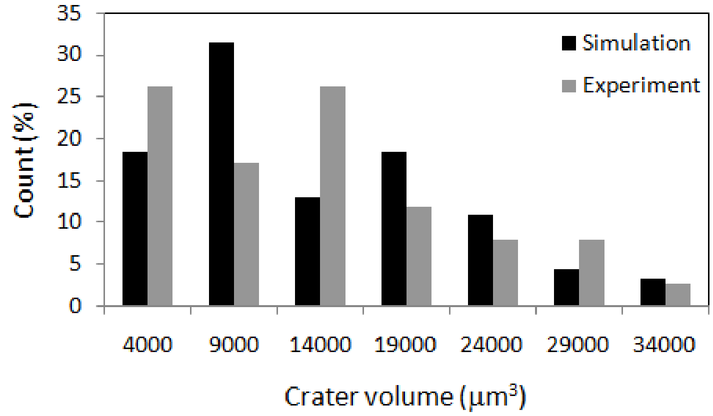
Count (%)
Simulation
Experiment
Crater volume (μm³)

(a)

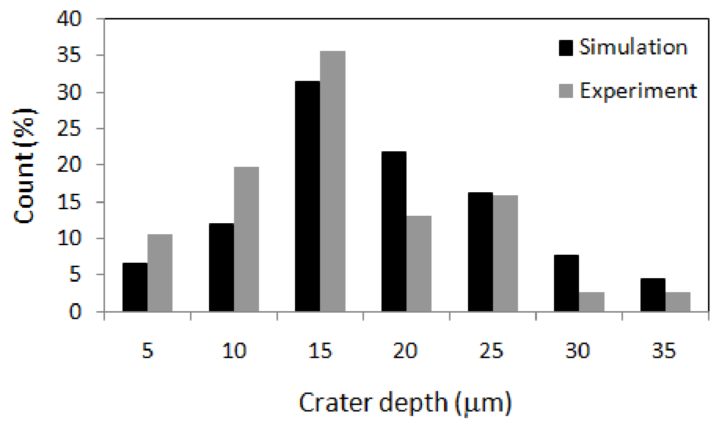
Count (%)
Simulation
Experiment
Crater depth (μm)

(b)

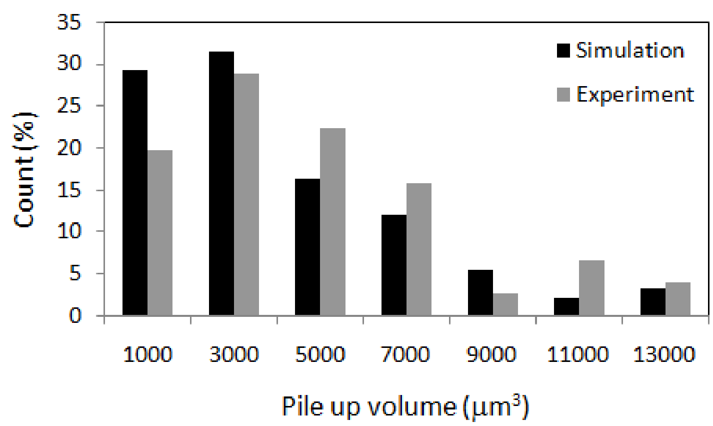
Count (%)
Simulation
Experiment
Pile up volume (μm³)

(c)

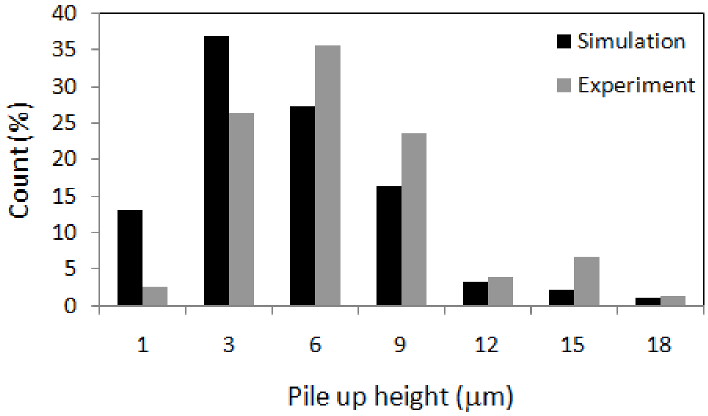

(d)

Fig. 5-5. Measured and simulated size distributions of surface features resulting from particle impacts perpendicular to the surface at 117 m/s: (a) crater volume, (b) crater depth, (c) pile-up volume, and (d) pile-up height.

5.4.3 Oblique Incidence

The effectiveness of the model in simulating surface features resulting from oblique impacts was investigated at an impact angle, $\alpha_i = 30^{\circ}$, so chosen because it is near the angle at which maximum erosion rate for Al6061-T6 occurred. **Fig. 5-7** shows that, similar to the normal incidence case, the measured and predicted crater and pile-up size distributions compare well. **Fig. 5-8** shows very good agreement between simulated and measured average crater and pile-up dimensions, with statistically insignificant differences (t-test, $P > 0.05$) of 2%, 16%, 4% and 12% for crater volume, pile-up volume, crater depth and pile-up height, respectively. It can thus be concluded that the present methodology generates particles that can represent the impact behavior of actual particles both at normal and oblique impact reasonably well. It can also be concluded that the material constitutive equation implemented in the numerical model was a good representative of the target material behavior under realistic impact conditions.

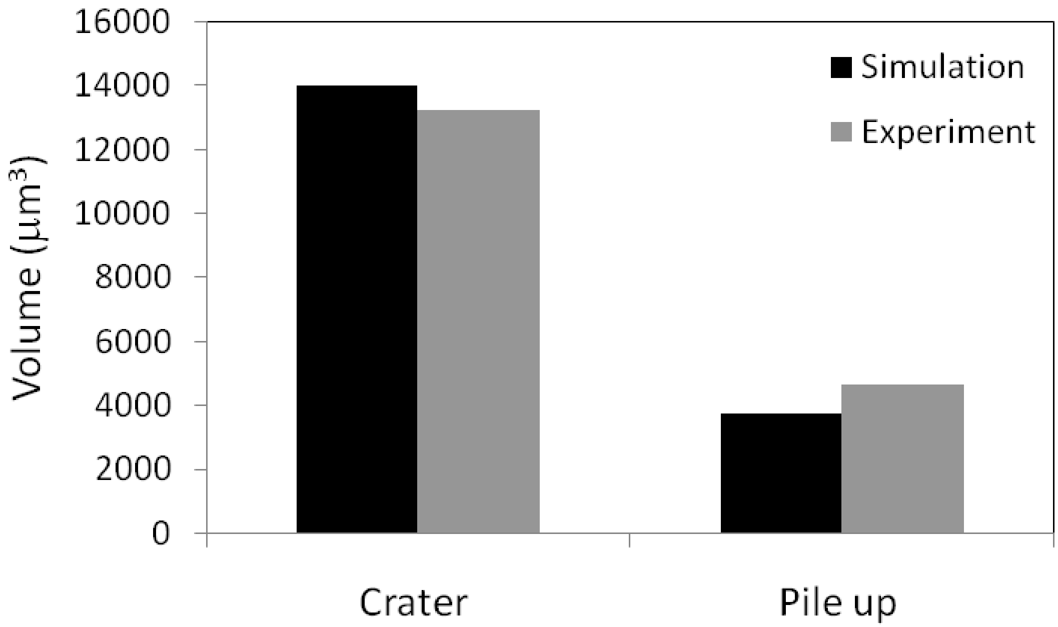

(a)

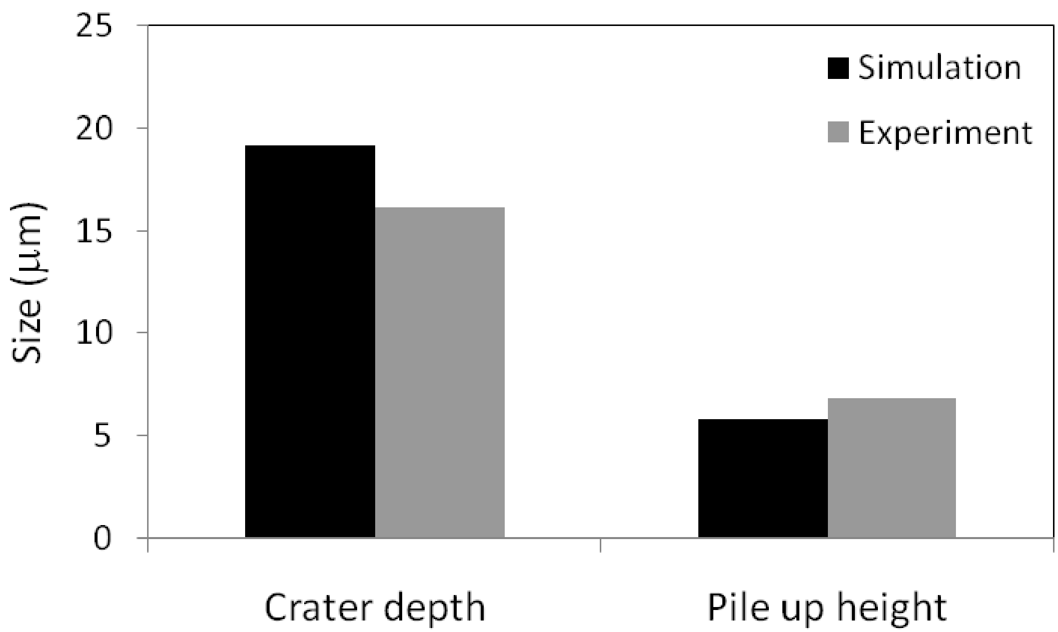

(b)

Fig. 5-6. Measured and predicted average dimensions of surface features resulting from impacts perpendicular to the surface at 117 m/s. (a) crater and pile-up volume, (b) crater depth and pile-up height.

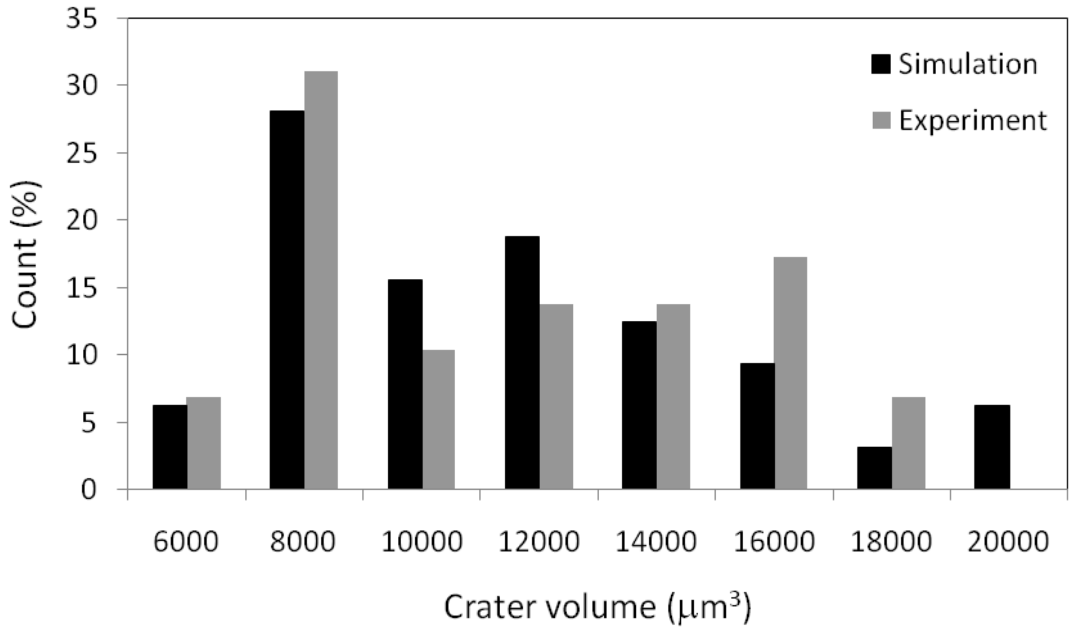
35
30
25
20
15
10
5
0
Count (%)
Simulation
Experiment
6000
8000
10000
12000
14000
16000
18000
20000
Crater volume (μm³)

(a)

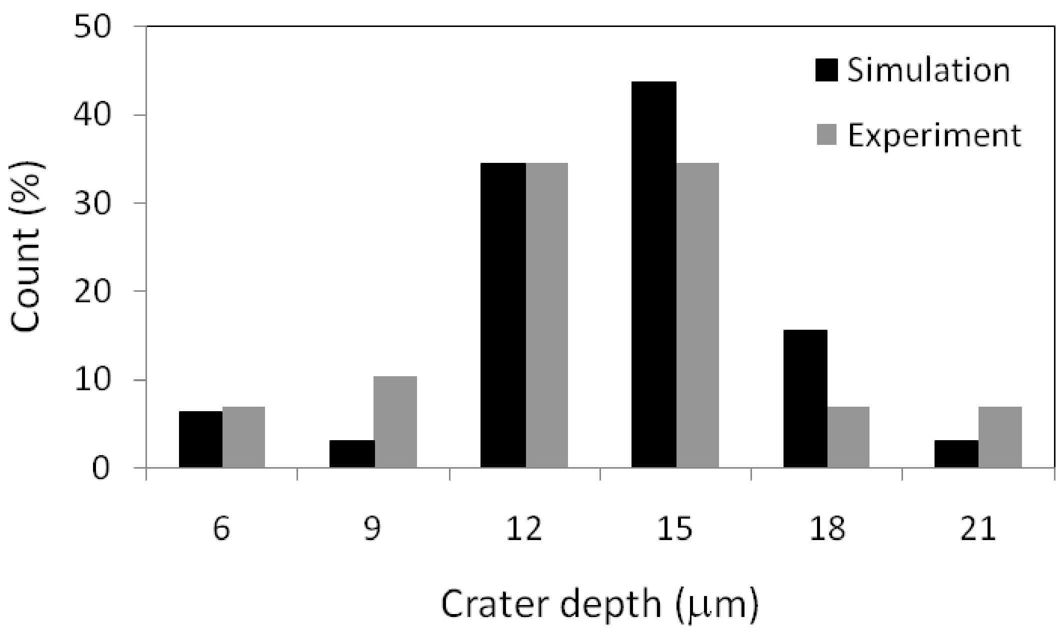
50
40
30
20
10
0
Count (%)
Simulation
Experiment
6
9
12
15
18
21
Crater depth (μm)

(b)

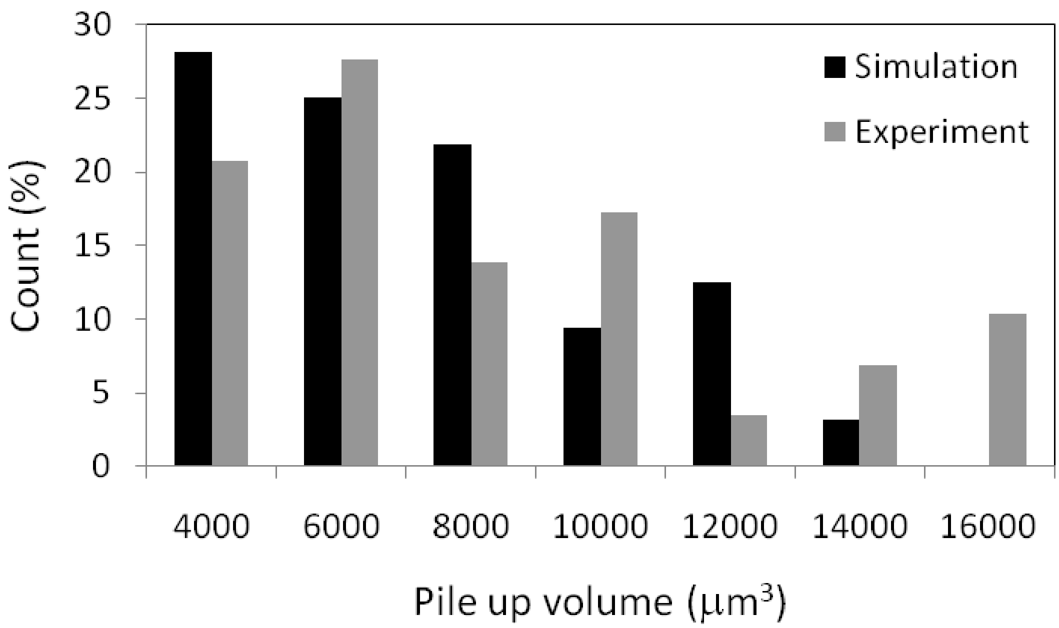

(c)

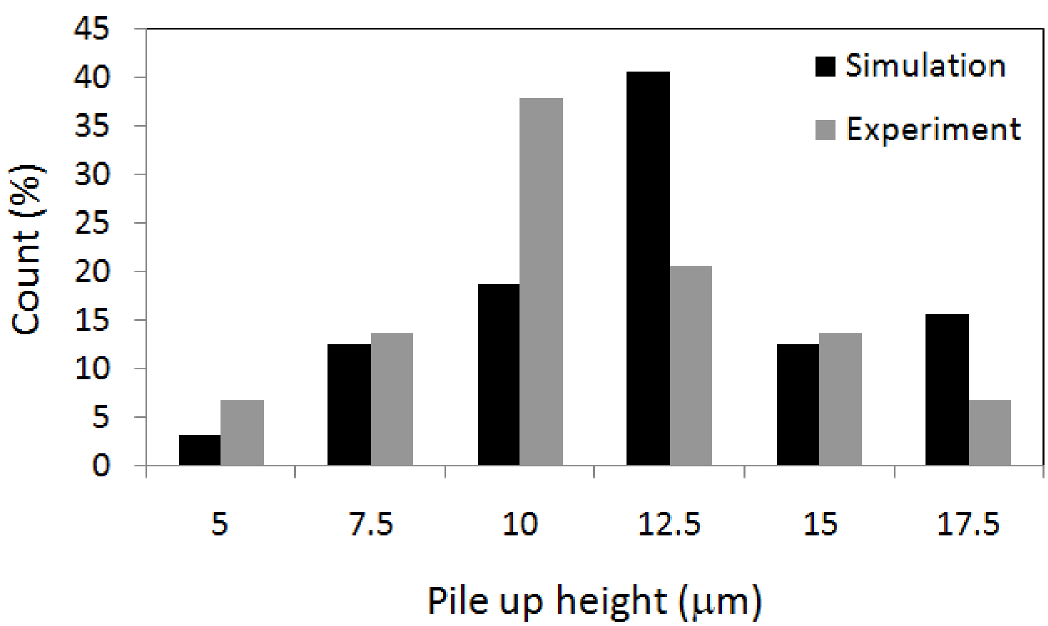

(d)

Fig. 5-7. Measured and simulated size distributions of surface features resulting from particle impacts at 117 m/s incident at 30° to the surface: (a) crater volume, (b) crater depth, (c) pile-up volume, and (d) pile-up height.

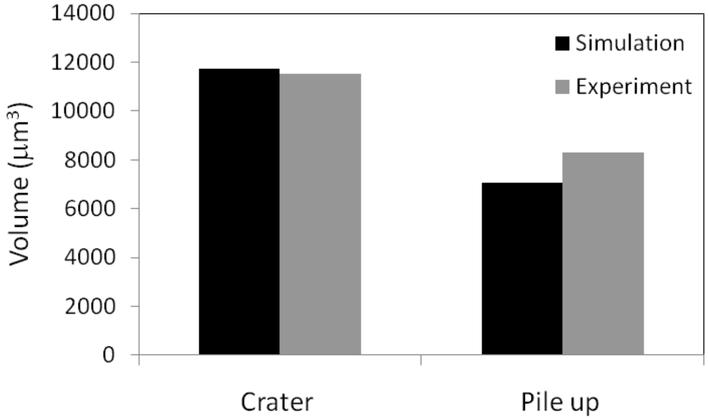

(a)

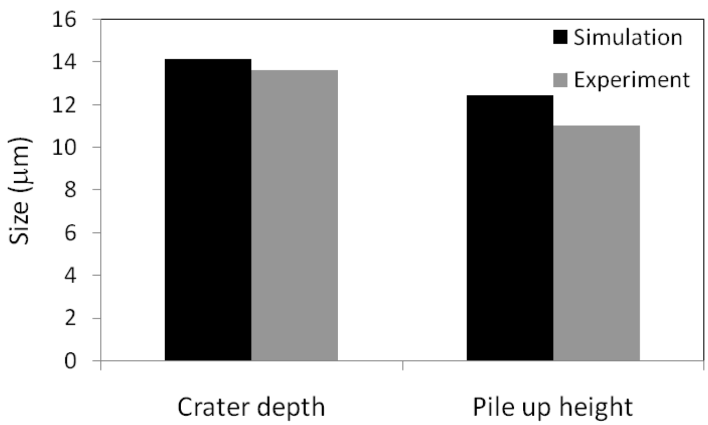

(b)

Fig. 5-8. Measured and simulated average dimensions of surface features resulting from impacts of particles at 117 m/s incident at 30° to the surface (a) crater and pile-up volume, (b) crater depth and pile-up height.

5.4.4 Material removal mechanisms

Depending on their shape, orientation with respect to the target, impact angle, and velocity, impacting particles may result in different erosion mechanisms. In the pioneering work of Hutchings [25] on single impact of square particles, he distinguished two general types of impact mechanisms: forward impact and backward impact. Forward rotating particles result in target material being pushed to the edge of deep and short triangular craters, and backward rotating particles involve the cutting of a smooth crater as the particle sweeps along the surface.

Forward tumbling particle impacts at 30° and 117 m/s are shown in **Fig. 5-9**. The craters formed by the impact of particles numbered 1 and 3 are similar to the typical ones shown in **Fig. 5-4b**. The profiles on the plane passing the point of maximum depth, in the direction of impact incidence are depicted in **Fig. 5-10**. The shape of these profiles are in accordance with the previously reported craters for forward rotating 2D particles, having triangular shaped crater profiles with raised material at their edges [30]. The impact of particle number 2 led to the formation of a slender crater. These kinds of craters with material pile-ups at their edges were also observed in the experiment as shown in **Fig. 5-11**. The formation of these craters can be attributed to the impact of particle edges on the surface as can be observed for particle 2 in **Fig. 5-9**. These types of craters were also observed during experimental studies of silicon carbide particle erosion of aluminum alloys [104], and were characterized as smearing craters. Consistent with this previous study, the present analysis also showed that the formation of these smearing craters was more dominant at oblique incidence. An analysis of the impact trajectory of all the particles in the simulation led to the conclusion that almost 96% of the particles underwent forward tumbling at an incident angle of 30° to the surface.

Both the experimental and simulated craters shown in **Fig. 5-4** had a large pile-up at their edges indicating that most probably the same impact mechanism was dominant in both the experiment and the simulation. Study of single impacts on different aluminum alloys in [53] showed how low strain hardening can result in localized deformation which contributes to the removal of the material from the surface. As already shown in **Chapter 3**, for a material like Al6061-T6 which shows very little strain hardening [106], the localized deformation exhibited itself as a considerable pile-up for both normal and oblique impacts. Particle number 3 in **Fig. 5-9** tumbled forward, leading to the formation of raised material, circled in **Fig. 5-9d**, which was loosely attached to the surface. This behavior is similar to the material removal mechanism proposed by Sheldon and Kanhere [35]. They argued that the metal removed had flowed around the sides of the advancing particle until it was strained sufficiently to break off. In addition, Sundararajan [37] attributed one of the mechanisms for material removal under single particle impact to crater lip fracture due to the inertial tensile stresses.

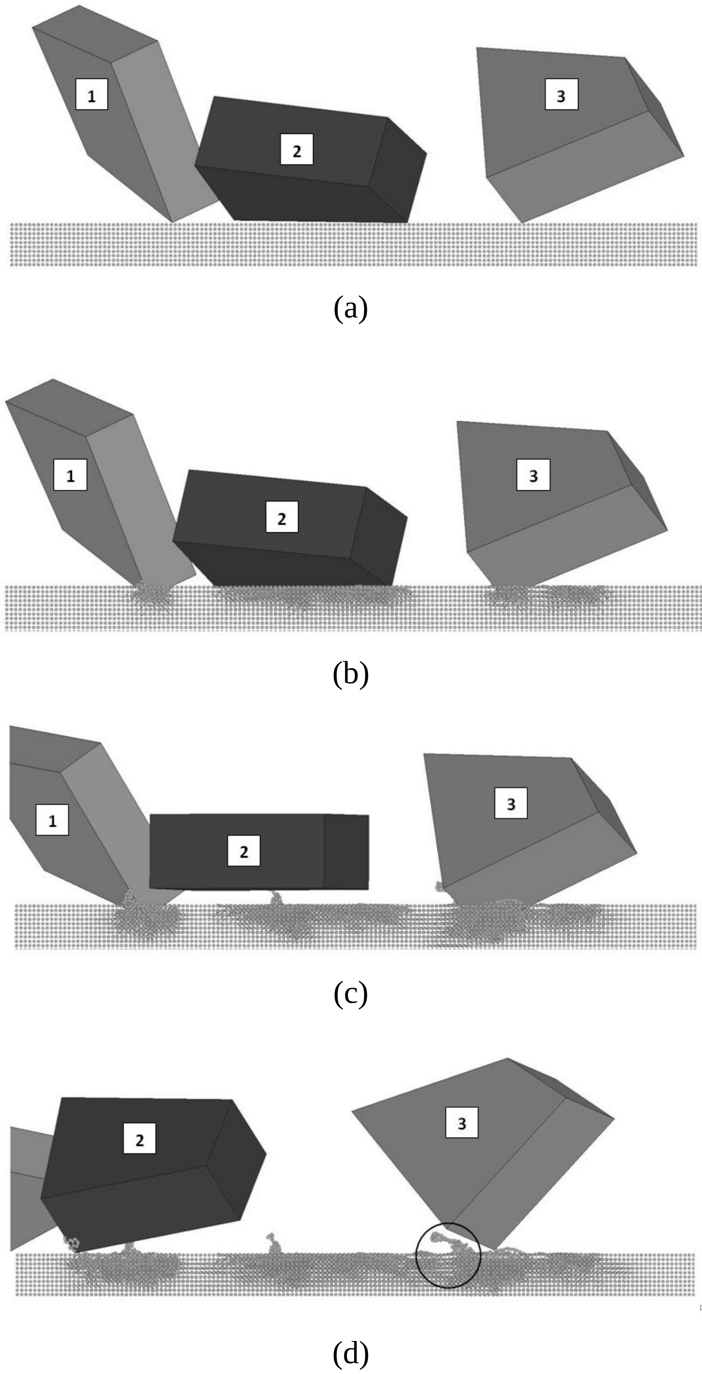

Fig. 5-9. Simulation of a number of particles from the modeled sample of aluminum oxide particles impacting at V = 117 m/s and $\alpha = 30^{\circ}$. The particles are incident from right to left and are shown at four instants: (a) The initial orientation of the particles with respect to the target; (b) Formation of craters. Note that the extra crater below particle 3 is due to the impact of another particle which is not shown in the figure; (c) Rebound of particles from the surface; (d) Impact of particle 2 on a previously formed pile-up by particle 1. Loosely attached pile-up formed by particle 3 is circled.

Pile-up material also plays an important role in material removal from the surface of ductile materials during erosion tests [31], [36], [107]. For example, Levy [64] proposed that a mechanism in which raised or pile-up material might be forged, loosened and knocked off by subsequent impacts is responsible for material loss at all impact angles. The knocking off of crater lips has been previously assumed to occur by the initial contact of the subsequently impacting particle. However, multiple impacts of a forward tumbling particle may also contribute to this material removal mechanism. For example, following the trajectory of particle number 2 in **Fig. 5-9**, it can be seen that its secondary impact shown in **Fig. 5-9d** removed the crater lip formed by the impact of particle number 1. Therefore, the role of the secondary impacts, which have comparable velocity to the first impacts, appears to be important when considering material removal mechanisms. The occurrence of these secondary impacts for forward rotating 2D particles was also observed in the experimental work of Dhar et al. [30].

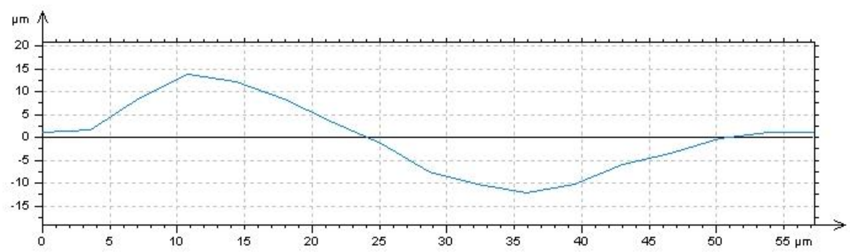

(a)

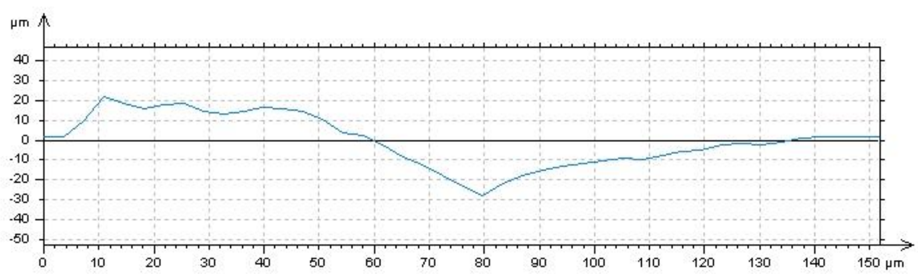

(b)

Fig. 5-10. The profiles on the plane passing the point of maximum depth, in the direction of impact incidence of the craters resulting from the impact of: (a) particle 1; and (b) particle 3 in **Fig. 5-9.**

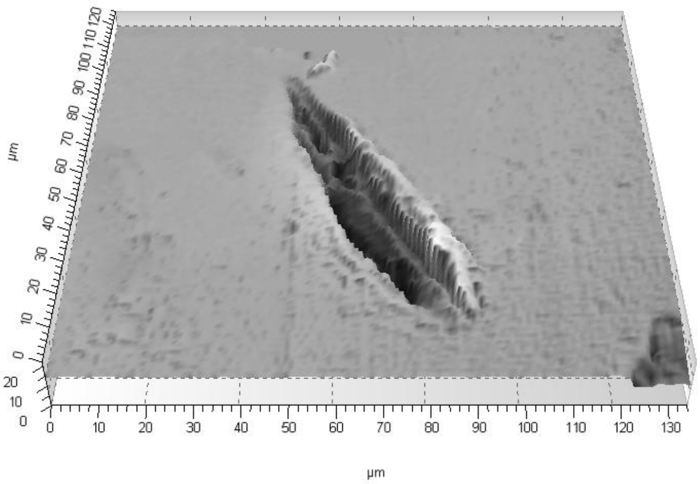

Fig. 5-11. A typical slender crater resulting from the impact of a particle edge such as, e.g. particle number 2 in **Fig. 5-9.**

As shown in **Chapter 2** and **3** and noted by a number of authors [24], [26], [29], [30], [62], [73], single particle impacts can also directly machine and separate a chip of material from the surface through backwards rotation. Two different mechanisms of this type were previously observed to occur for sharp 2D rhomboid particles. The backward rotation of a particle might either result in chip detachment from the surface through a pure machining, as reported in [25], [30] or a tunneling mechanism, as reported in [30]. The former involves cutting a smooth crater as the particles sweeps along the surface. Interestingly, this type of pure machining was not observed during the present simulation, consistent with previous reports that it should occur only over a very limited range of incident conditions [24], [26]. Moreover, the experiments in [91], [94] were limited to two dimensions, i.e., particles were perfectly flat and made to impact such that there were no out of plane rotations, and the cutting edge remained parallel to the surface. In the present work, the particles were made to impact at random orientations, so that the leading edge of the particle was not parallel to the surface, and out of plane rotations did occur. This made the perfect machining action observed in previous studies of 2D single impacts [30] even less probable.

Material removal through a mechanism in which the leading cutting edge tunneled below the surface and a chip was pried from the surface and ejected was, however, observed in the present simulation, as shown in **Fig. 5-12**.

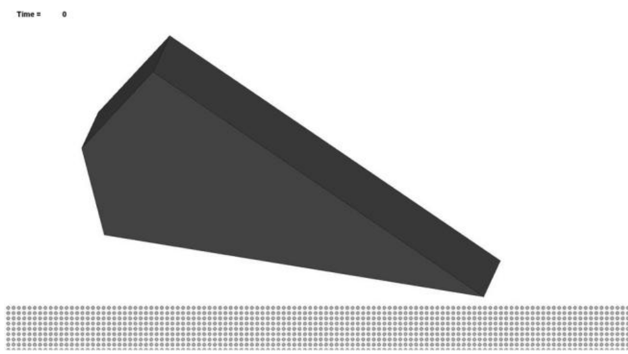

(a)

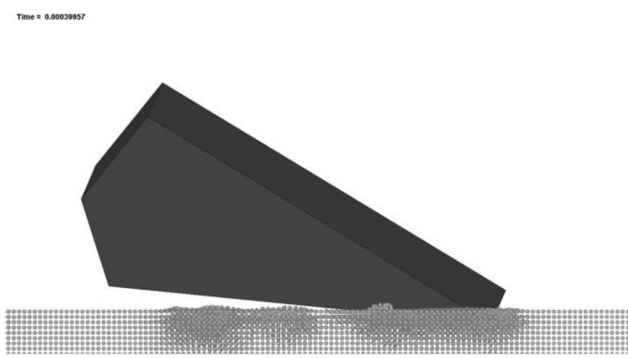

(b)

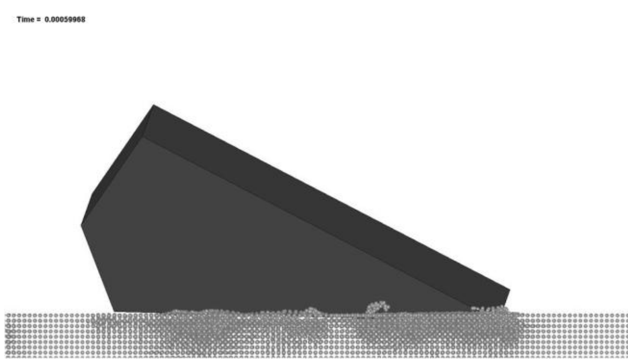

(c)

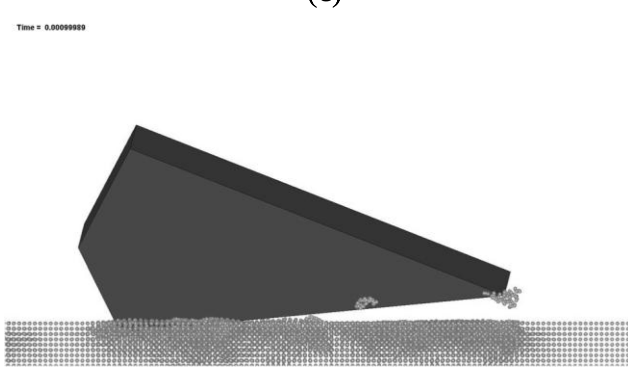

(d)

Fig. 5-12. A simulated tunneling mechanism of material removal for a particle incident at $a = 90^{\circ}$ and 117 m/s.

5.5 Summary and conclusions

A methodology for generating the geometries of angular 3D particles based on measured samples of actual erodent was presented. Samples of generated particles, modeled with finite elements, were used to simulate their high speed impact on an aluminum alloy (Al6061-T6) which was modeled using SPH particles and a Johnson-Cook/Cowper Symonds constitutive relationship. Comparisons were made between the simulated and measured geometries of the resulting impact craters. The conclusions can be summarized as follows:

(a) The numerical simulations produced craters and crater lips that had similar size distributions to those measured for both perpendicular and oblique incidence. The differences between the average measured and simulated crater volumes, pile-up volumes, crater depths and pile-up heights were statistically insignificant (P-value > 0.05). Therefore, it can be concluded that the present particle generation methodology can be used to accurately represent samples of abrasive powder.

(b) The model captured several previously noted material removal and crater formation mechanisms. The pure machining of surface, previously observed for 2D particles was found to be less probable for the presently considered 3D irregularly shaped particles, which were not constrained to a 2D impact. On the other hand, material removal was found to occur with the 3D particles through a tunneling mechanism, consistent with previous observations for highly angular 2D particles. It was also found that secondary impacts of particles may contribute to material removal by removing a lip of material that was previously formed.

(c) Consistent with the results of **Chapter 3**, SPH was a fairly robust methodology to simulate large deformation under particle impact. It also allowed the simulation of the large degree of crater lip pile-up that occurs for Al6061-T6 due to its low degree strain hardening. This is beneficial for simulating multiple particle impacts in which the crater lip plays an important role in material loss through the cooperative effect of multiple particle impacts. This will be considered in **Chapter 6**.

Chapter 6 Numerical Simulation of Multiple Overlapping Impact of Alumina Particles on Al6061-T6

6.1 Introduction

As explained in **Section 1.3.3**, previous studies demonstrated the potential of numerical modeling of erosion phenomena. However, they were limited to impacts of uniformly sized idealized spherical particles. The models were not utilized to identify actual material removal mechanisms. Most particle erosion processes involve the impact of irregularly shaped particles of various sizes, a much more complex situation that may involve any number of different erosion micro-mechanisms. **Chapter 5** presented a methodology for generating realistic 3D angular solid particles that have size and shape distributions that match actual samples of erodent. When coupled to an SPH model with appropriate target constitutive properties, the resulting model was shown to accurately simulate material damage arising from the impact of a large number of single non-overlapping impacts on an Al6061-T6 target. In this chapter it will be demonstrated that the model can also be used to predict the accumulation of surface damage and material removal arising from multiple interacting (overlapping) impacts of irregular particles, and thus the resulting volumetric erosion rate.

6.2 Experiments

The experiments were performed using the same equipment and methodology described in **Chapter 5**, but for much longer blasting times. Briefly, Al6061-T6 samples were blasted with 150 μm nominal diameter granular aluminum oxide particles at 300 kPa, resulting in an average particle mass flow rate and velocity of 1.5 g/min and of 117 m/s, respectively. Experiments were performed at impact angles of 15°, 30°, 45° and 60° with blasting times varying between 1 and 60 s, controlled using an electronic shutter.

6.3 Model Description

The SPH model for the target and the particle generation technique are explained in detail in **Chapter 5**. To approximate conditions at the surface in a small region close to where the jet centerline intersected the surface, the impacts of a total of 105 particles incident at 117 m/s and at impact angles of 15°, 30°, 45° and 60° were simulated. In all the simulations, the particle centres of mass were randomly placed in a 100 μm × 100 μm area above the simulated 600 μm × 600 μm target area of **Fig. 6-1** No contact between the particles was defined. In order to save computational time, instead of launching the particles one by one, the 105 particles were divided into groups of three. Although **Fig. 6-1** shows that all 105 particles were placed relatively close to the target, the particles in each of the three groups were made to impact at different times using an LS-DYNA restart analysis after each group impact was completed. This approach also facilitated ensuring the convergence of the plasticity algorithm (see **Section 5.3.2** of **Chapter 5**) in a more computationally inexpensive manner because, in the event of a convergence failure, it allowed the adjustment of the time step corresponding to a single restart analysis rather than the entire simulation from the start. The 5 μm spacing between the SPH particles was the same as the model presented **Chapter 5**. For a computer having four Intel 2.80 GHz processors and 8 GB of RAM, typical simulation runtimes were on the order of 17 hours.

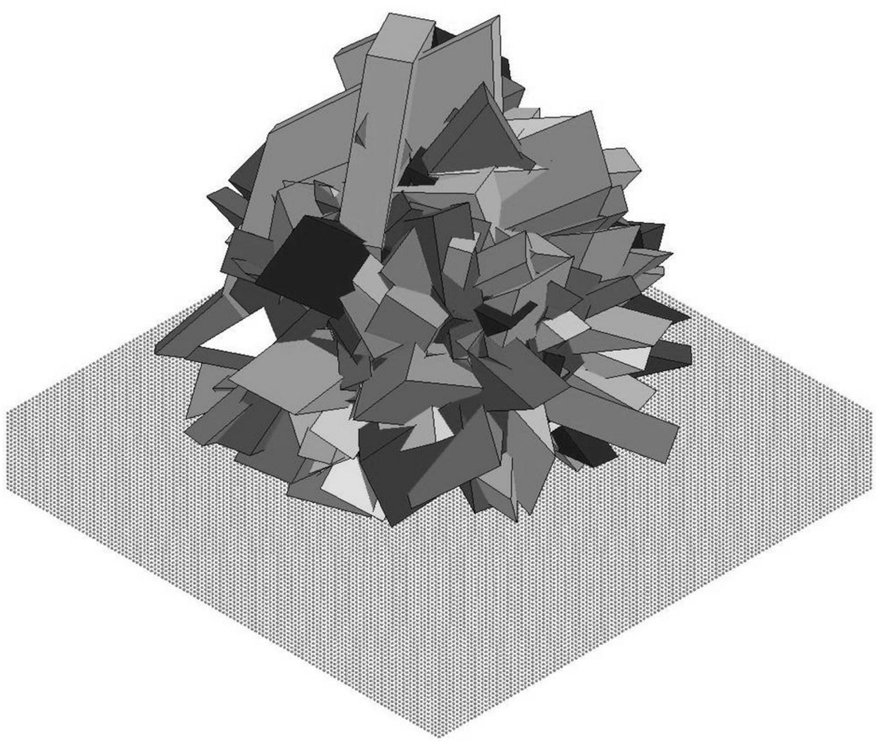

Fig. 6-1. FE modeled particles randomly placed above the SPH modeled target.

6.4 Analysis of simulated and experimental eroded surfaces

As in **Chapter 5**, the blasted target surface profiles were scanned using an optical profilometer (Nanovea ST400, Micro Photonics Inc., Allentown, PA, USA), and analyzed using Professional 3D software (Micro Photonics Inc., Allentown, PA, USA) to obtain the area and volume of the erosion scar formed on the surface. The coordinates of the surface SPH particles for each simulation were imported into the same software for analysis. The simulated erosion scar areas resulting from the 105 particle impacts were approximately 34×10^{-3} mm^2, 31×10^{-3} mm^2, 28×10^{-3} mm^2, and 27×10^{-3} mm^2, for impact angles of 15°, 30°, 45° and 60°, respectively. The experimental erosion scar volumes were measured over these same areas, which were centered in the much larger blast scars at the point where the jet centerline intersected the surface.

Since the rate at which the particles were launched in the simulation was chosen on the basis on minimizing execution time, it did not correspond to actual impact frequencies seen in the experiments. Therefore, a comparison of the experimental and numerical volumetric erosion rates required the simulation time to be correlated to the real time. By comparing the measured and predicted scar volumes at a 60° impact angle, it was found that the impact of 105 particles in the simulation corresponded to an experimental blasting duration of approximately 38 s. Using the measured mass flow rate and the average mass of a particle mentioned in **Chapter 5**, and assuming a uniform distribution of the particles over the approximately 5 mm diameter scar area, the total number of particles impacting a 100 μm × 100 μm area during 38 s of blasting was calculated to be 93 particles, which compares well with the 105 which was assumed. This was taken as a strong indication that the calculated time scaling correlation was realistic, and it was thus also used to compare the experimental and numerical results at the other impact angles.

6.5 Results and discussion

6.5.1 Blasted surface topography

Multiple impacts of the modeled particles resulted in deformation and removal of the Al6061-T6 target material. **Fig. 6-2** shows a topography evolution for a numerically blasted surface after the impact of 21, 63, 84 and 105 particles at an impact angle of 30°. After the impact of 21 particles, **Fig. 6-2b** shows evidence of macroscopic roughening, with individual craters and lips of raised materials still distinguishable. **Figs. 6-2c** and **d** show that after 63 impacts, individual impact craters are more difficult to distinguish, with a larger single crater appearing on the surface. This may correspond to the development of a wave or ripple pattern on the surface, as been noted to occur when the surfaces of ductile metals are blasted at oblique angles [108] [109]. Ballout et al. [110] attributed the formation of these patterns to the accumulation of raised crater lips from individual impacts. After coverage of the surface with individual impacts, the downstream advancement of material displacement and removal leads to the coherence of the individual craters and lips and gradual formation of a ripple pattern. The formation of a wave of raised material on the target surface can be seen as a white band ahead of the erosion scar in **Fig. 6-3,** which is a top view of the blasted surface shown in **Fig. 6-2d**.

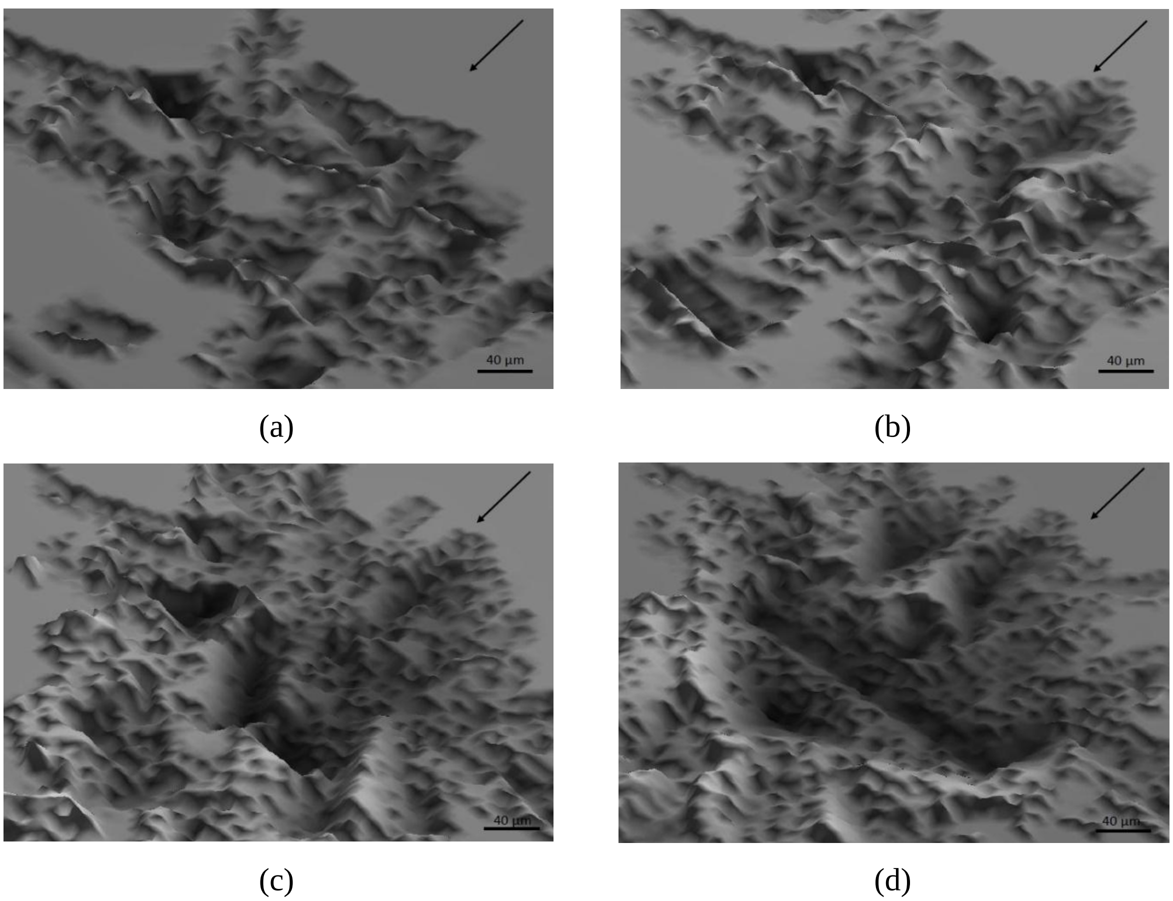

Fig. 6-2. The evolution of simulated surface topography during erosion at V = 117 m/s and $\alpha = 30^{\circ}$. The impact direction is shown with a black arrow. Scattered craters can be observed in (a). Macroscopic roughening of the surface is distinguishable in (b). A larger crater appears in (c) and (d).

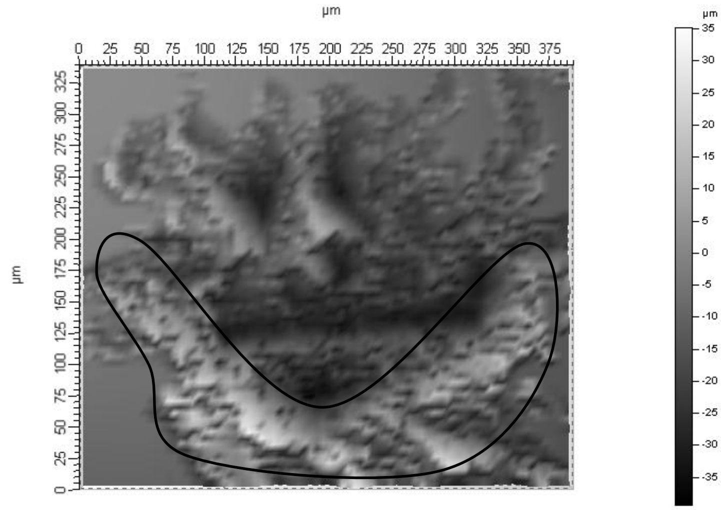

Fig. 6-3. Top view of eroded surface of **Fig. 6-2d**. The black lasso identifies the formation of a wave of raised material on the surface. Particles are incident from top to bottom.

6.5.2 Predicted erosion at various angles of attack

The dependence of the simulated and measured scar volumes on the mass of impacting particles at the various impact angles are shown to be in very good agreement in **Fig. 6-4**. The results are also in accordance with the common observation that the erosion rate (volume of material removed per mass of particle blasted) initially increases with increasing particle mass dose, before reaching a steady state [111], indicated by the linear portions of the curves in **Fig. 6-4**. As will be discussed in **Section 6.3.3**, the erosion rate is initially low on the initially smooth surface, but increases once a soft layer containing craters and raised materials has been fully established.

Fig. 6-5 shows that the simulated and measured volumetric erosion rates at the different angles (the slope of the lines in **Fig. 6-4**) are in good agreement, both indicating the angle of maximum erosion as 30°. The average difference between the predicted and measured erosion rates was 7%, with a maximum difference of 13% occurring at an angle of incidence of 15°.

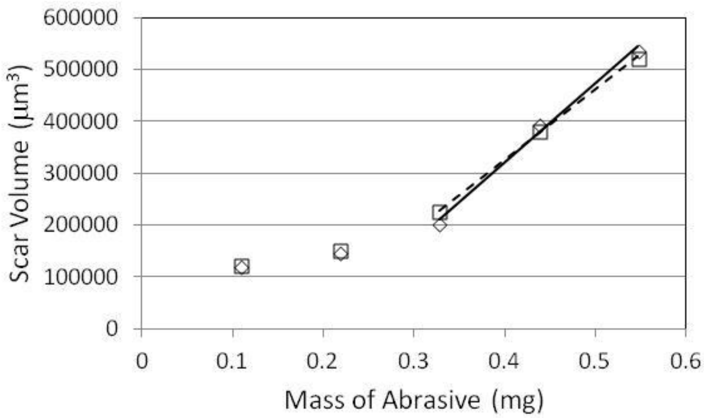
Scar Volume (μm³)
Mass of Abrasive (mg)
0
100000
200000
300000
400000
500000
600000
0
0.1
0.2
0.3
0.4
0.5
0.6

(a)

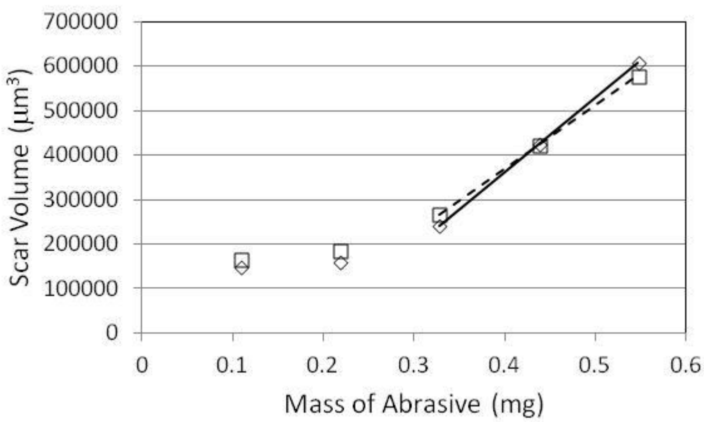
Scar Volume (μm³)
Mass of Abrasive (mg)
0
100000
200000
300000
400000
500000
600000
700000
0
0.1
0.2
0.3
0.4
0.5
0.6

(b)

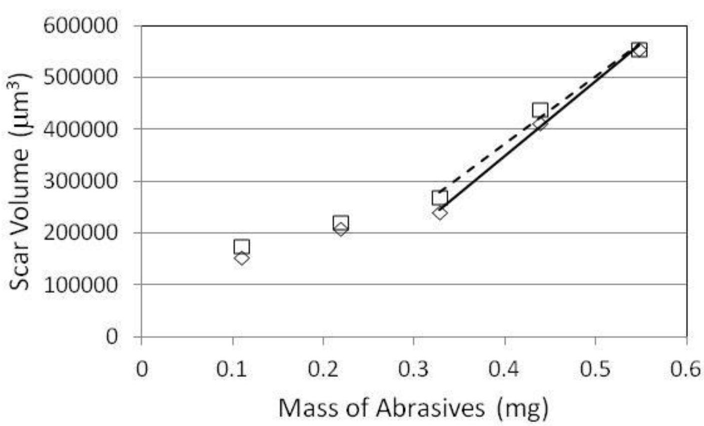
Scar Volume (μm³)
Mass of Abrasives (mg)
0
100000
200000
300000
400000
500000
600000
0
0.1
0.2
0.3
0.4
0.5
0.6

(c)

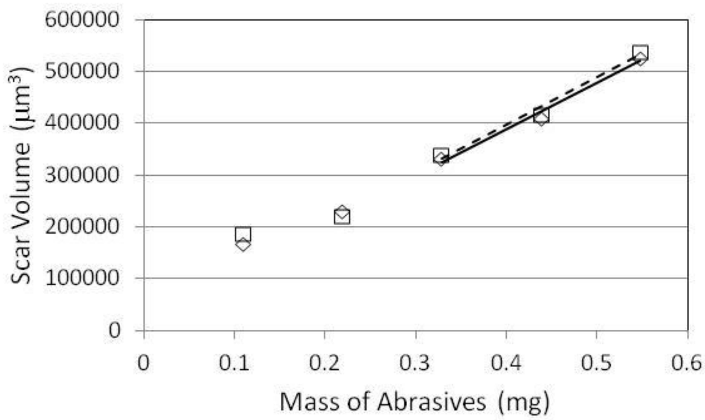

(d)

Fig. 6-4. Variations of volumetric erosion rate at impact angles of (a) 15°, (b) 30°, (c) 45° and 60° for ◇ experiment and □ simulation. The solid and dashed lines indicate the least squares best linear fit of the steady state erosion portion of the experimental and simulated results, respectively.

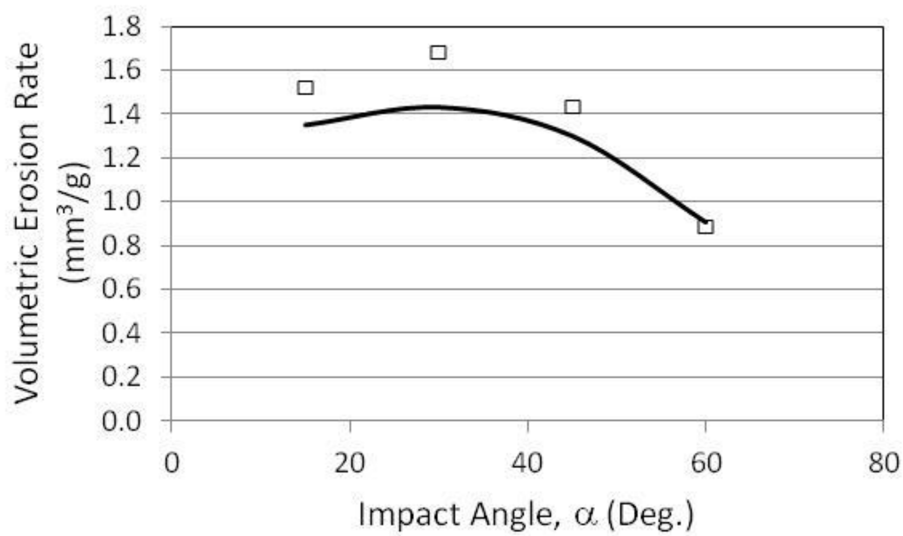

Fig. 6-5. Predicted and measured variation of volumetric erosion rate with impact angle, i.e. the slope of the linear portions of **Fig. 6-4**. (□ experiment, **—** simulation).

6.5.3 Simulated erosion mechanisms

The numerical simulation of the particle impacts allowed the tracking of individual particles to identify several previously cited material removal mechanisms involving the cooperative effect of multiple impacts.

6.5.3.1 Crater pile-up creation and forging mechanisms

The particle shown in **Fig. 6-6,** which was located in the first group of particles, impacted the intact surface at an angle of 30° and velocity of 117 m/s. The effects of other particles striking are also shown in **Fig. 6-6**, although the particles themselves are not shown. The particle exhibited four interactions with the target surface which combined to result in material loss.

The initial impact due to the particle shown in **Fig. 6-6a** plowed the surface and formed a lip of material, which has been circled in **Fig. 6-6b**, straining the material to a maximum value of 1 mm/mm, in accordance with the extrusion effect described by Bellman and Levy [104] in their studies of the erosion mechanisms of low and high strength aluminum alloys. Takaffoli and Papini [73] also noted a large amount of raised crater lip material for single impacts of angular particles on Al6061-T6. While these lips remained attached to the surface in most of the cases identified in Takaffoli and Papini [73] and in the present work, the experimental study of Winter and Hutchings [52] indicated that the lip material was more likely to eject for harder target materials such as Ti-6Al-4V. They concluded that for multiple particle impacts, Ti-6Al-4V eroded more readily than materials that exhibited overhanging lips such as mild steel or aluminum alloys when subjected to single particle impacts. Visual tracking of particles in the present simulations also confirmed that significant interactions between the impacting particles and the raised crater lips occurred. These served to reduce the role of subsequent impacting particles in generating new piled up material on the surface.

In **Fig. 6-6c**, the particle is shown rebounding, and, in **Fig. 6-6d**, striking at 96 m/s the crater lip (dash-circled in **Fig. 6-6c**) that had just been formed by another impacting particle (not shown), in the time between **Fig. 6-6b** and **6c**. This resulted in "forging" [104] or "smearing out" [109] of the raised material. The particle then impacted another crater lip that had been formed in the time interval between **Fig. 6-6b** and **6c** (solid-circled in **Fig. 6-6c**) at a velocity of 85 m/s, causing two ridges (dash-circled in **Fig. 6-6e**) to form on the elevated material, as observed by Bellman and Levy [104] during their SEM studies of a fixed location on the blasted surface at different blasting times. From these observations, Bellman and Levy postulated that forging deformation of crater lip material by impacting particles could lead to formation of platelets whose detachment from the surface was the major mechanism of material loss in ductile metals. The present simulations showed that due to the wide range of particle shapes and initial orientations with respect to the target, the process of material detachment was not straightforward and easily distinguishable. Besides forging, the impacting particles also can push the raised material down to the bottom of craters that make tracking the material deformation more difficult. The SPH modeling of the target provided an advantage for simulating these features, since it inherently allowed self-contact of the target materials. As noted by Cousens and Hutchings [112], and Brown et al. [113], this pushing down can finally lead to material removal through a flaking mechanism.

Finally, **Fig. 6-6e** (note inset rear view) shows that the particle slid along the surface and stretched the elevated material circled in **Fig. 6-6d**, making it more vulnerable to removal by subsequent impacts.

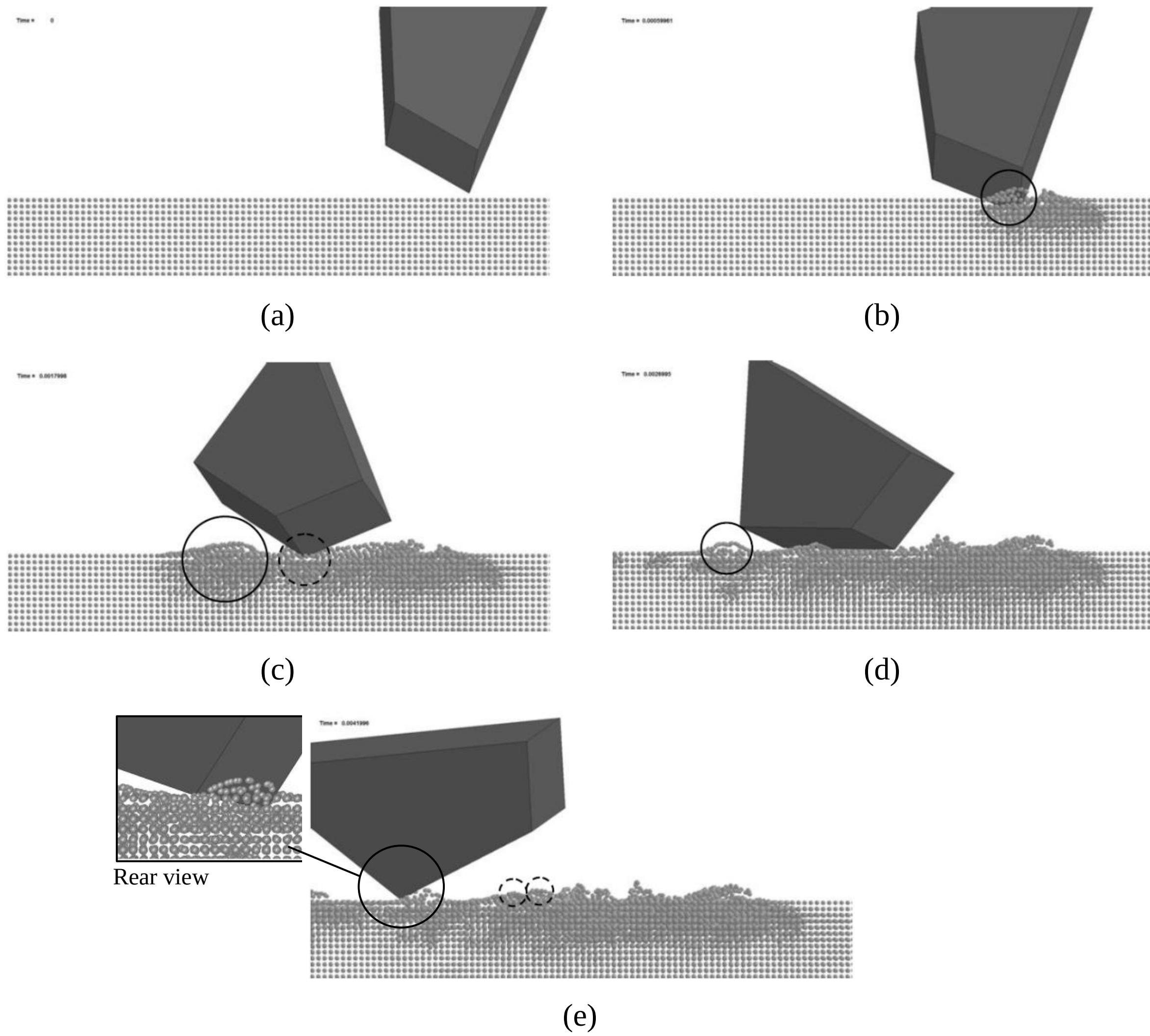

Fig. 6-6. A sequence of multiple impacts for one of the particles in the model showing four interactions with the surface. The impact incidence is from right to left at an angle of 30° with the horizontal. The particle impacts in (a), and forms raised crater lips circled in (b). It then strikes a crater lip dash-circled in (c) and after that in (d) it impacts another lip (solid-circle in (c)). The inset on (e) shows the circled material in (d) being stretched by the impacting particle, using a view from the rear looking towards the reader.

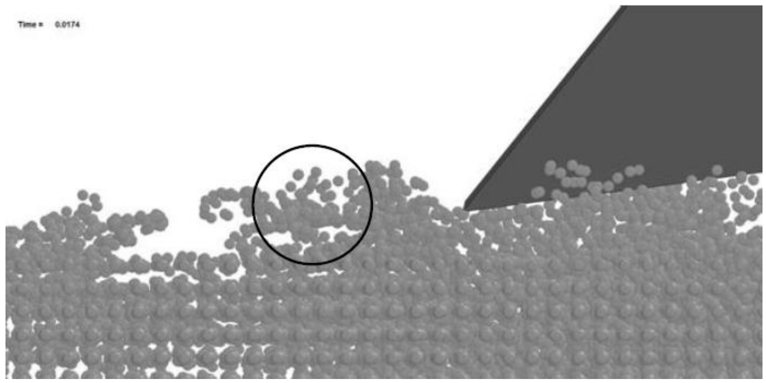

(a)

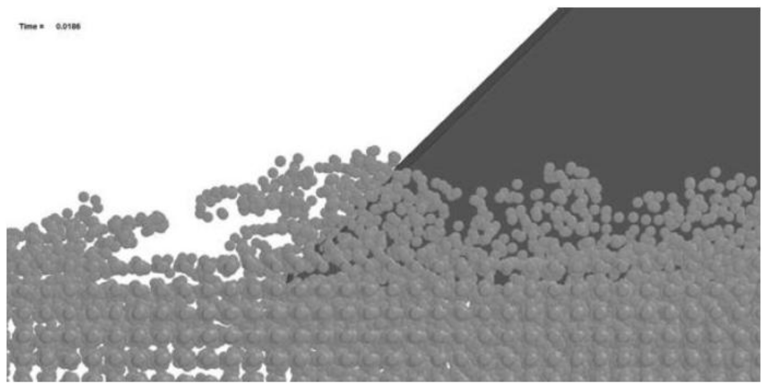

(b)

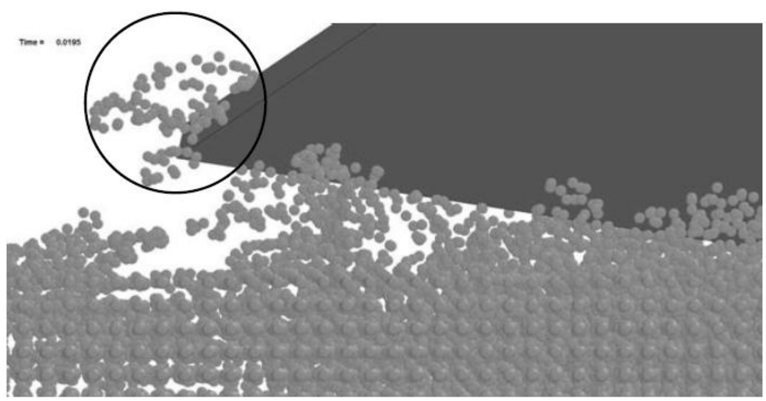

(c)

Fig. 6-7. Machining of a previously formed raised crater lip (location marked by circle in (a)) by a particle impacting the surface at an impact angle of 60° with respect to the horizon. The particle is incident from right to left and ultimately machines away the material shown circled in (c).

6.5.3.2 Material removal by particle impact on crater lips

The removal of raised crater lips by impacting particles reported in [104] was also observed in the present simulation. **Fig. 6-7** shows a particle incident at 60° micromachining the crater lip (circled in **Fig. 6-7a**) that was previously formed by another impacting particle. The particle underwent backward rotation and left the surface at a velocity of 27 m/s with an out-of-plane rotation.

6.5.3.3. Development of steady state erosion rate due to cooperative effects of multiple particle impacts

The simulation can be used to explain the commonly observed phenomenon [111] that the erosion rate initially increases with particle dose, before reaching steady state. For example, **Fig. 6-8** shows the same particle in **Fig. 6-7,** but made to impact an uneroded flat surface at the same incident velocity, angle, and orientation. In this case, the particle exhibited a pure machining impact mechanism similar to those observed for 2D single angular particles in [25], [26], [73], but removed a piece of material circled in **Fig. 6-8c** which was almost four times smaller compared to the one circled in **Fig. 6-7c** that was removed from the already eroded surface. The effect of previous impacts on the surface thus increased its micromachining efficiency, resulting in more material removal. Another such example is shown in **Figs. 6-9 and 6-10** for the impact of a particle at an angle of 60° on an intact and eroded surface, respectively. When the particle impacted the intact surface, it caused only plastic deformation, smearing the surface as shown in **Fig. 6-9**. However, when impacting the previously eroded material, it resulted in the detachment of the piece of material circled in **Fig. 6-10c**. These examples provide evidence that the formation of lips on the surface at high angles of attack might favor a micromachining mechanism for a particle whose shape and orientation did not exhibit a cutting mechanism when impacting an intact surface. The results are consistent with the conclusions of Brown and Edington [114], who claimed that the cutting erosion mechanism should be considered even at high angles of attack.

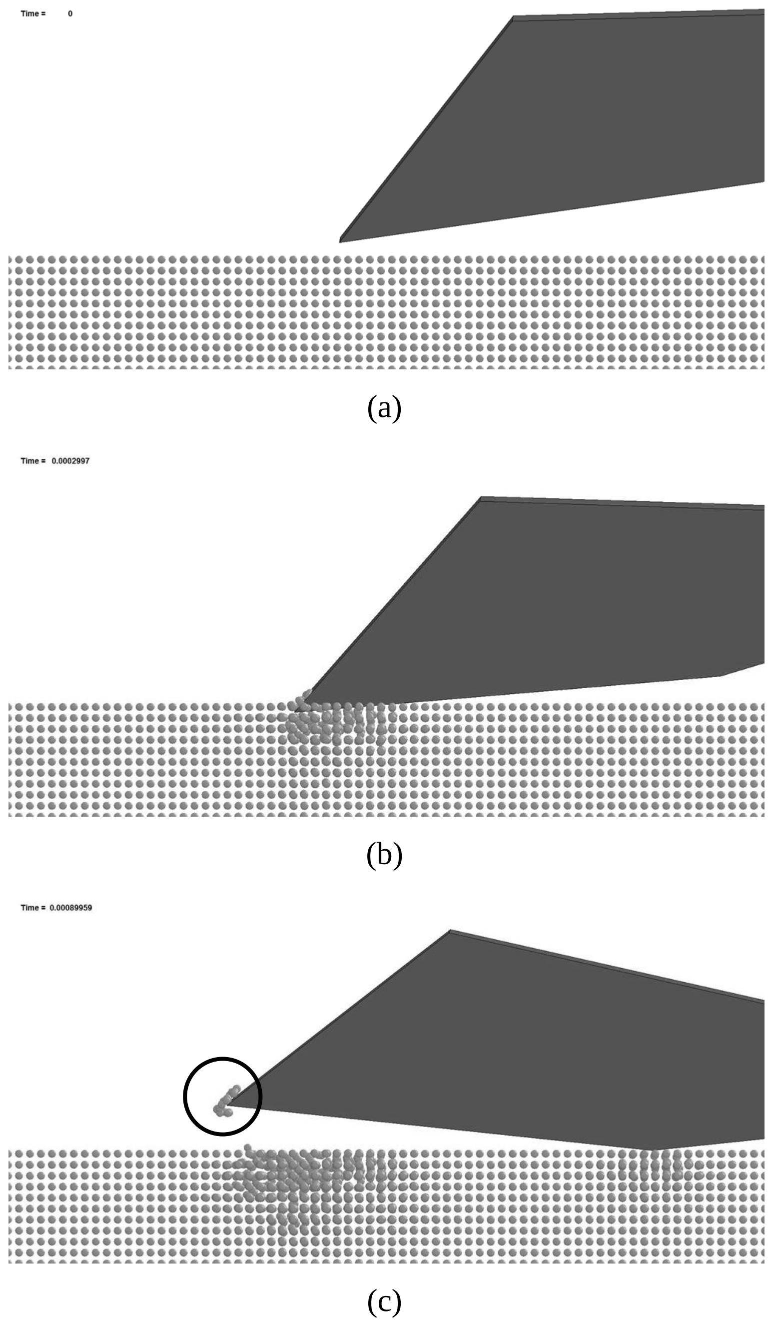

Fig. 6-8. The impact of the particle shown in **Fig. 6-7** on an uneroded surface. The particle is incident from right to left.

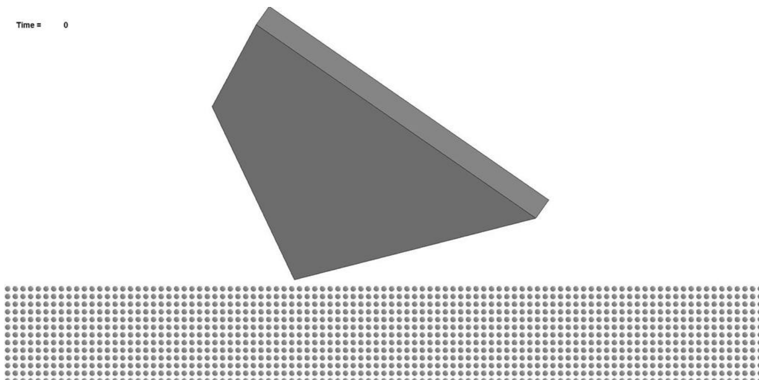

(a)

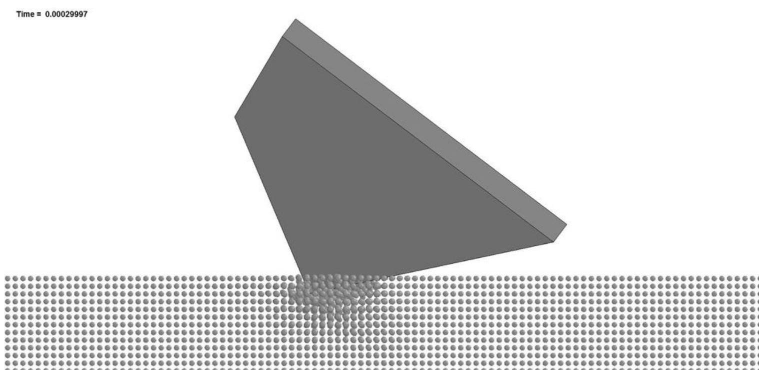

(b)

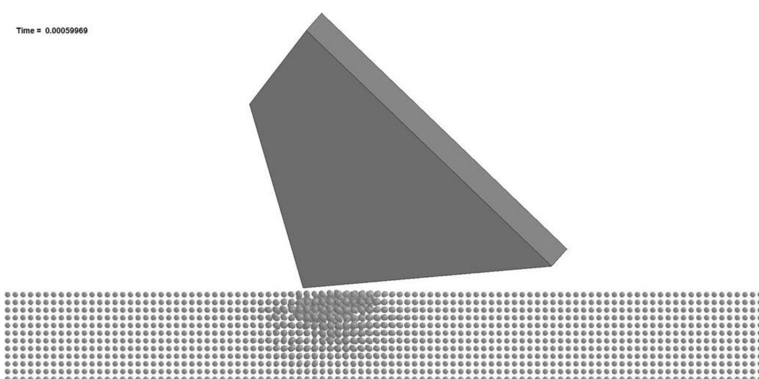

(c)

Fig. 6-9. Single impact of a particle on an uneroded surface. The particle is incident from left to right with an angle of 60° to the horizon.

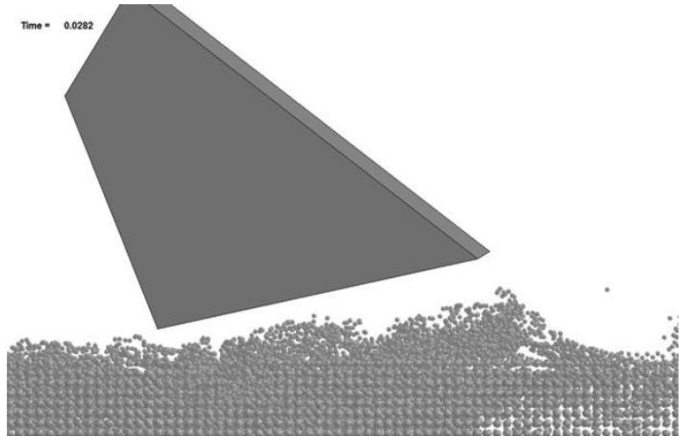

(a)

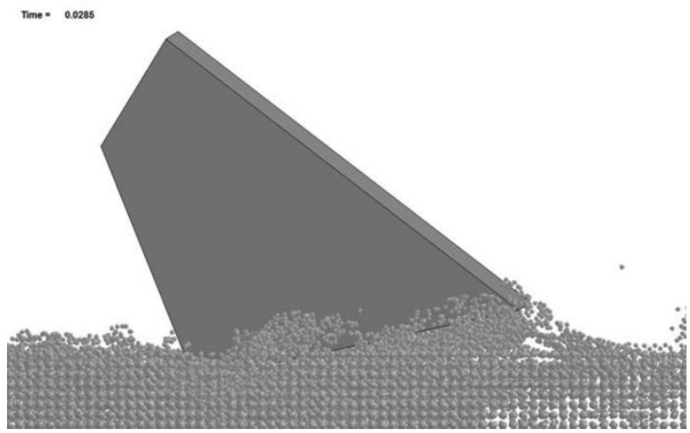

(b)

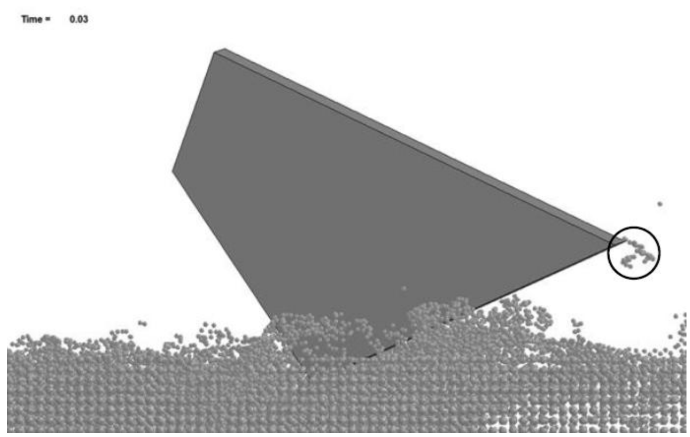

(c)

Fig. 6-10. The removal of a material piece on an eroded surface by the same impacting particle shown in **Fig. 6-9**. The particle is incident from left to right.

6.5.4 The effect of thermal softening on material removal

Despite a general agreement on the existence of a significant temperature increase during the solid particle erosion of metals, its role on material loss has been a subject of debate [105]. In the solid particle erosion of aluminum alloys, Bellman and Levy [104] found evidence that some of the target material was welded to the particles after they had impacted, but nevertheless concluded that the material loss by local melting was insignificant. Based on their erosion testing of several steels, aluminum, copper, and titanium alloys, Jennings et al. [115], however, postulated that melting played an important role in target material removal. However, the relative contribution of thermal and mechanical mechanisms to material removal was not determined. While the current model could not be used to simulate melting, the effect of temperature increase on the erosion was investigated by comparing the simulated results considering thermal softening, to those neglecting it, i.e. with the m and D_5 parameters in the Johnson-Cook constitutive and damage equations (see eq. 3-11) set equal to 0. For an impact angle of 30°, it was found that including the effect of thermal softening during impact resulted in a four times larger material removal mass than when this effect was ignored. This was in accordance with the findings of Bellman and Levy [104], who postulated that when a soft layer is formed near the surface, the harder material beneath it acts as an anvil, enhancing the localization of material and formation of crater pile lips at the surface.

6.6 Summary and Conclusions

Multiple overlapping particle impacts of a sample of 150-μm alumina particles modeled using the technique of the accompanying paper [116] on an Al6061-T6 target were simulated using an SPH model with a Johnson-Cook/Cowper Symonds constitutive relationship for the target material. The impact of 105 particles on the surface at different impact angles led to the formation of an erosion scar whose volume was compared with that measured in experiments. The conclusions of the current study can be summarized as follows:

(a) The impact angle at which the maximum volumetric erosion rate occurred was predicted to be approximately 30°, in agreement with the experimental results from the erosion tests. The predicted erosion rates were on average within 7% of those measured.

(b) The simulation produced a surface topography which qualitatively agreed with previous observations of the blasted surfaces of ductile metals. The previously reported formation of a wave surface pattern in the erosion scar was also observed in the simulation.

(c) Interactions between the impacting particles and the crater lips such as forging, stretching and knocking off of the raised material that have been previously speculated to occur by other investigators were identified in the simulations.

(d) The cooperative effects of multiple impacts on material loss were identified in the simulations by comparing the impact mechanisms of typical particles on an uneroded surface with their impact on an eroded surface. It was found that the lip formation from previous impacts greatly increased the material removal efficiency of subsequently impacting particles. This also provided a possible explanation for the commonly noted initial increase of erosion rate with particle dose before reaching the steady state.

(e) SPH based simulations are promising techniques for the modeling of the large target material deformations and material removal mechanisms arising from the solid particle erosion of ductile metals.

Chapter 7 Summary and Conclusions

7.1 Summary

A gas gun was designed and built to accelerate single idealized angular rhomboid particles to perform impact tests on ductile materials. The experimental results were used to verify numerical models of single particle impacts. In the Lagrangian FE modeling of the impacts, the problem of element distortion due to the large deformations of the ductile materials was addressed using two different techniques: element deletion and remeshing. Both predicted the measured dimensions of the impact craters and adjacent material pile-up well. However, both methods suffered from some deficiencies, including their dependency on a nonphysical parameter and some numerical instabilities (**Chapter 2**). Therefore, in **Chapter 3**, the single impacts of the rhomboid particles were modeled using SPH which better accommodates large deformations due to its meshless formulation. Comparison of the predicted results with the measured demonstrated that SPH was effective in modeling the large deformations resulting from the impact of single angular particles of well-defined shape. A more sophisticated numerical model of solid particle erosion required replacing the well-defined 2D rhomboid particles that were used in **Chapters 2** and **3** with more realistic irregular 3D particles that represented actual abrasive samples. A methodology to generate such particles was developed in **Chapter 4**. It took as input the measured size and shape distributions of an alumina powder, and outputted CAD models of particles that followed the measured size and shape distributions. In **Chapter 5,** the generated particles were implemented in a FE/SPH coupled model that simulated their high speed non-overlapping impact on an aluminum alloy target. The model predicted distributions of the sizes of the resulting craters and piled up crater lips were found to match those measured from particle impact tests well. The model allowed various impact mechanisms to be identified by tracking of the individual particle impact trajectories.

Finally, in **Chapter 6**, for the first time, a numerical model of multiple overlapping impacts of angular particles was developed and used to predict the erosion rate of an aluminum alloy. The simulation was also used to identify various material removal mechanisms that have been postulated to exist from observations in the literature. The model predicted the angle of maximum erosion rate fairly well. The steady state volumetric erosion rates predicted by the simulation for various impact angles were in good agreement with the measured findings.

7.2 Conclusions

The main conclusions of this dissertation are:

i. Element deletion at a critical strain in order to remove distorted elements from FE models of particle impact could be used to model both ploughing mechanisms and machined chip separation in erosion processes. However, the model required the use of a nonphysical critical strain criterion for removing the distorted elements which results in significant errors in calculated eroded mass.

ii. Remeshing can be useful in modeling crater formation and pile-up due to particle impact. However, combining this method with a failure criterion to model chip separation from the surface proved to be impossible due to the occurrence of numerical instabilities.

iii. SPH proved to be a promising tool in modeling the very large deformations of ductile materials that result from the particle impact process. It can also simulate a wide variety of impact mechanisms that occur in solid particle erosion, due to variations in particle size, shape, impact angle, and initial particle orientation with respect to target.

iv. Measured particle size and shape distributions can be used together with a developed methodology in order to generate representative 3D models of actual irregularly shaped abrasive particles. This represents a significant improvement on previous models which were based on single sized spherical or idealized 2D particles.

v. Comparing the simulated and measured average crater and pile-up dimensions in normal non-overlapping impact of alumina particles showed a very good agreement, with statistically insignificant differences (t-test, $P > 0.05$) of 6%, 15%, 17% and 17% for crater volume, pile-up volume, crater depth and pile-up height, respectively. For oblique impact, the differences between the average experimental and predicted crater volume, pile-up volume, crater depth, and pile-up height were 6%, 15%, 17% and 17%, respectively. These differences were also found to be statistically insignificant (t-test, $P > 0.05$).

vi. Numerical simulations of the type presented in this dissertation that utilize overlapping impacts of realistic 3D particles can be used to identify commonly observed material removal mechanisms, and to accurately predict the erosion rate of ductile materials. The predicted erosion rates were on average within 7% of those measured. Moreover, the impact angle at which the maximum volumetric erosion rate occurred was predicted to be approximately 30°, in agreement with the experimental results from the erosion tests.

7.3 Contributions

The novel contributions of this dissertation can be summarized as:

i. Design and construction of a gas gun apparatus which allowed high speed impact tests of 2D particles to be performed with well-controlled initial particle orientation and impact angle.

ii. Investigation of the applicability of different FE techniques in modeling the large deformations and the chip machining phenomena that occur during angular particle impact. All previous models had been for spherical particles.

iii. Development of SPH models for the impact of angular particles on ductile materials which enabled simulation of various impact mechanisms such as lip formations and chip separation. All previous models had been for spherical particles.

iv. Identification of the Cowper Symonds strain rate dependency relation with the Johnson-Cook constitutive equation as the most appropriate to to simulate conditions arising during high-speed impact by angular particles on Al6061-T6.

v. Development and verification of a novel methodology for generating 3D representative models of erodent powders based on their size and shape parameter distributions.

vi. Simulation of multiple overlapping impacts of irregularly shaped non-uniform sized 3D angular particles which enabled direct correlation between the erosion rate in simulations and experiments. Only simulations of spherical particles had been previously performed.

.

vii. Identification, using the model of (vi) of the cooperating effect of multiple particle impacts and the confirmation of previously hypothesized material removal mechanisms from the solid particle erosion literature.

7.4 Recommendations for Future Work

A number of interesting extensions to the present work could be made in the future. These are listed below:

i. The present work only considered numerical modeling of the solid particle erosion of ductile materials, and did not consider brittle materials, which fail by crack propagation. Remeshing is most likely not necessary for brittle materials because they generally fail at much lower deformations than ductile materials, and thus are not likely to suffer from element distortion problems. However, one can speculate that element deletion and SPH might be used to model material fracture, if a suitable criterion is used to define material cleavage. For example, the Johnson-Holmquist (J-H) constitutive and failure model [117] might be used in simulations of the erosion of brittle materials. These models have been already used in spherical particle impact simulations of a ceramic material using the element deletion technique [55] and in the SPH simulation of the perforation of brittle targets by steel spheres. However, its applicability in modeling single and multiple impacts of angular particles on brittle materials needs to be investigated.

ii. The impact of small particles on a ductile surface leads to a very high strain rate deformation (higher than 10^4 s^{-1}). There are not many devices that can be used to measure the material behavior at such high strain rates. Therefore, it would be of interest to explore the use of experimental results in conjunction with numerical models similar to those developed in the current dissertation in order to determine the high strain rate behavior of materials. Such a procedure has been suggested by Hutchings in [88], but has never been attempted. This could be done by utilizing an inverse approach that minimizes the difference between the experimental and simulated geometry of craters and pile-ups at various impact velocities and impact angles through optimization of the material parameters. In order to distinguish between constitutive and failure parameters, the optimization procedure could be first applied to impact mechanisms which only cause plowing to identify an appropriate constitutive material model. Then, the model could be used for simulating impact mechanisms which involve chip separation, in order to optimize the failure model parameters. Such an inverse approach has been already used to identify dynamic properties of materials from Hopkinson pressure bar [118] or in cutting simulations [119].

iii. The developed FE/SPH coupled model was only applied to a soft ductile metal which exhibited a large amount of raised crater lip material during particle erosion. The impact of angular particles on hard ductile materials could also be investigated using the proposed methodology. Good candidate materials for such a study would be those in which the formation of shear bands has been proposed as a contributing mechanism to material loss in particle erosion, e.g. Ti-6Al-4V, 7075-T6 aluminum alloy and 301 stainless steel [37], [52].

iv. The effect of particle shape on erosion could be studied using the developed models by simulating the impact of erodent samples having identical average sizes, but with different shape parameters. Such a study would be virtually impossible to perform experimentally due to the difficulty in finding abrasive powders having the desired shape and size distributions.

v. The analyses from this dissertation were focused on particle erosion processes in which the erodent was much harder than the target material. Therefore, a rigid model was defined for the particle. However, the relative hardness of particles and the target sample and the possibility of particle fragmentation are important in some particle erosion applications, especially involving brittle targets [120]. Modifying the models developed in the current analysis by SPH modeling of particles in conjunction with a damage model might provide an appropriate tool to model particle fragmentation during impact.

vi. Grit blasting is commonly used for preparation of surfaces for plasma spraying [121] or adhesive bonding [122]. Models that allow the prediction of surface roughness in ductile target materials as a function of particle and process parameters would be extremely useful, but nevertheless do not currently exist. The models developed in this dissertation for multiple overlapping impacts could be utilized to predict roughness in grit blasting processes. However, this would require significant computational resources since a relatively large sample length is required in order to meet current roughness measurement standards.

Appendices

A.1 A MATLAB Code to Generate a Representative Model of Erodent Powders

% This code generates a sample of modeled particles develops based on the algorithm

% presented in **Section 4.3** which. These particles have the same size and shape distribution

% as actual particles shown in **Fig. 4-1**.

```
mean_outerdiameter=266.8;
StdDev_outerdiameter=73.7;
perimeter=[];
roundness=[];
rotation=[];
area=[];
x=[];
y=[];
j=1;
i=1;
k=1;
n=1;
count_01_02=0;
count_02_03=0;
count_03_04=0;
count_04_05=0;
count_05_06=0;
count_06_07=0;
count_07_08=0;
count_08_09=0;
count_09_1=0;
count_0_01=0;
%
% Roundness Distribution
%
num_0_01=0;
num_01_02=0;
num_02_03=0;
num_03_04=5;
num_04_05=17;
num_05_06=49;
num_06_07=89;
num_07_08=27;
```

```
num_08_09=0;
num_09_1=0;
Particle_Count=188;
v=[1,Particle_Count];
thickness=[];
impactsite_length=1500;   %micron
positionx=[];
positiony=[];
positionz=[];
particle_dis=[];
%
% Area Distribution
%
for j=1:4
area(j)=0+7500*rand;
end
for j=5:7
area(j)=7500+7500*rand;
end
for j=8:28
area(j)=15000+7500*rand;
end
for j=29:94
area(j)=22500+7500*rand;
end
for j=95:154
area(j)=30000+7500*rand;
end
for j=155:174
area(j)=37500+7500*rand;
end
for j=175:179
area(j)=45000+7500*rand;
end
for j=180:182
area(j)=52500+7500*rand;
end
for j=183:185
area(j)=60000+7500*rand;
end
for j=186:188
area(j)=67500+15000*rand;
end
%
% Thickness Distribution
%
```

```
for j=1:5
    thickness(j)=20+20*rand;
end
for j=6:9
    thickness(j)=100+20*rand;
end
for j=10:24
    thickness(j)=120+20*rand;
end
for j=25:63
    thickness(j)=140+20*rand;
end
for j=64:119
    thickness(j)=160+20*rand;
end
for j=120:162
    thickness(j)=180+20*rand;
end
for j=163:179
    thickness(j)=200+20*rand;
end
for j=180:184
    thickness(j)=220+20*rand;
end
for j=185:188
    thickness(j)=240+60*rand;
end
for j=1:Particle_Count
    i=1;
    m=1;
    n=1;
%
% Creating Vertices of Particles
%
while i<6
outerdiameter=mean_outerdiameter+StdDev_outerdiameter*randn;
randnumx=(outerdiameter/2)*randn;
randnumy=(outerdiameter/2)*randn;
distance=sqrt(randnumx^2+randnumy^2);
if distance<=(outerdiameter/2)
    x(j,i)=randnumx;
    y(j,i)=randnumy;
    i=i+1;
if i==4
    y(j,i)=(outerdiameter/2)*randn;
    x(j,i)=(2*area(j)-(x(j,3)-x(j,1))*(y(j,4)-y(j,2))-(x(j,2)*(y(j,3)-y(j,1))))/(y(j,1)-y(j,3));
```

```
    i=5;
end
if i==5
    xintersectionv1v4_v2v3=(((y(j,3)-y(j,2))/(x(j,3)-x(j,2)))*x(j,2)-y(j,2)-((y(j,4)-y(j,1))/(x(j,4)-
x(j,1)))*x(j,1)+y(j,1))/((y(j,3)-y(j,2))/(x(j,3)-x(j,2))-(y(j,4)-y(j,1))/(x(j,4)-x(j,1)));
    xintersectionv3v4_v1v2=(((y(j,4)-y(j,3))/(x(j,4)-x(j,3)))*x(j,3)-y(j,3)-((y(j,2)-y(j,1))/(x(j,2)-
x(j,1)))*x(j,1)+y(j,1))/((y(j,4)-y(j,3))/(x(j,4)-x(j,3))-(y(j,2)-y(j,1))/(x(j,2)-x(j,1)));
    if (xintersectionv1v4_v2v3<=max(x(j,:)) & xintersectionv1v4_v2v3>=min(x(j,:))) |
(xintersectionv3v4_v1v2<=max(x(j,:)) & xintersectionv3v4_v1v2>=min(x(j,:)))
        i=1;
    end
end
if i==5
   perimeter(j)=sqrt((x(j,2)-x(j,1))^2+(y(j,2)-y(j,1))^2)+sqrt((x(j,3)-x(j,2))^2+(y(j,3)-
y(j,2))^2)+sqrt((x(j,4)-x(j,3))^2+(y(j,4)-y(j,3))^2)+sqrt((x(j,4)-x(j,1))^2+(y(j,4)-y(j,1))^2);
   roundness(j)=4*pi*area(j)/perimeter(j)^2;
if count_0_01<num_0_01
    if (roundness(j)>0) && (roundness(j)<0.1)
        count_0_01=count_0_01+1;
        m=2;
    end
end
%
% Filling the Bins Based on the Roundness Distribution of Particles
%
if count_01_02<num_01_02
    if (roundness(j)>0.1) && (roundness(j)<0.2)
        count_01_02=count_01_02+1;
        m=2;
    end
end
if count_02_03<num_02_03
    if (roundness(j)>0.2) && (roundness(j)<0.3)
        count_02_03=count_02_03+1;
        m=2;
    end
end
if count_03_04<num_03_04
    if (roundness(j)>0.3) && (roundness(j)<0.4)
        count_03_04=count_03_04+1;
        m=2;
    end
end
if count_04_05<num_04_05
    if (roundness(j)>0.4) && (roundness(j)<0.5)
        count_04_05=count_04_05+1;
```

```
        m=2;
    end
end
if count_05_06<num_05_06
    if (roundness(j)>0.5) && (roundness(j)<0.6)
        count_05_06=count_05_06+1;
        m=2;
    end
end
if count_06_07<num_06_07
   if (roundness(j)>0.6) && (roundness(j)<0.7)
  count_06_07=(count_06_07)+1;
  m=2;
    end
end
if count_07_08<num_07_08
    if (roundness(j)>0.7) && (roundness(j)<0.9)
        count_07_08=count_07_08+1;
        m=2;
    end
end
if count_09_1<num_09_1
    if (roundness(j)>0.9) && (roundness(j)<1)
        count_09_1=count_09_1+1;
        m=2;
    end
end
if m==1
    i=1;
end
end
end
end
%
% Assigning a Random Orientation to the Generate Particles
%
rotation(j,1)=360*rand;
rotation(j,2)=360*rand;
rotation(j,3)=360*rand;
x(j,5)=x(j,1);
y(j,5)=y(j,1);
figure(1);
plot(x(j,:),y(j,:));
hold all;
end
```

A.2 An ANSYS Parametric Design Language (APDL) Code to Construct FE Model of a Sample of Representative Particles

```
!
! This code develops an FE model of generated particles in A.1
!
*DIM,x,,200,4
*DIM,y,,200,4
*DIM,particle_number,,1
*DIM,particle_thickness,,200
*DIM,x_centroid,,200
*DIM,y_centroid,,200
*DIM,z_centroid,,200
*DIM,incx,,200
*DIM,incy,,200
*DIM,incz,,200
*DIM,x_rotation,,200
*DIM,y_rotation,,200
*DIM,z_rotation,,200
*DIM,position_x,,200
*DIM,position_y,,200
*DIM,x_position,,200
*DIM,y_position,,200
*Ask,particle_number(1),number of particles
!
! Coordinates of Particles' Vertices
!
x(1,1)=-35.6,35.7,20.7,-87.3,-6.4,-10.0,72.1,-128.0
x(9,1)=32.7,52.3,90.3,-19.6,-17.9,25.3,-99.0,-71.8
x(17,1)=138.1,17.1,41.8,26.5,49.0,-66.3,57.3,-33.7
x(25,1)=-26.3,5.8,-15.8,31.5,-11.7,-71.1,17.8,52.3
x(33,1)=91.4,26.3,-45.0,-79.6,-69.1,49.6,-144.1,4.2
x(41,1)=-31.3,-30.3,6.8,18.2,-22.7,-41.4,-44.0,31.8
x(49,1)=-30.6,-93.0,-101.6,3.2,115.0,-77.9,130.0,-89.1
x(57,1)=-53.8,17.1,44.1,109.9,80.4,-9.6,-60.8,-111.8
x(65,1)=65.1,19.9,-105.9,-60.0,55.1,8.2,106.6,-93.3
x(73,1)=57.5,-81.7,19.2,50.8,-66.3,117.3,-20.6,-46.4
x(81,1)=34.2,-22.4,-42.8,0.9,-184.2,-114.7,33.7,-40.5
x(89,1)=150.5,-56.2,9.0,15.5,29.5,36.2,-56.5,51.0
x(97,1)=-17.5,22.6,17.6,-57.2,2.3,2.8,-23.1,-135.0
x(105,1)=-154.3,-14.8,14.6,88.0,43.3,16.4,84.4,98.3
x(113,1)=57.8,166.2,133.3,-41.5,-102.7,42.6,-60.9,-70.5
x(121,1)=44.2,73.5,-95.3,145.0,-82.1,-69.9,-35.9,13.6
x(129,1)=-32.3,-143.4,64.6,15.6,-19.3,90.5,-33.0,4.7
x(137,1)=-89.9,83.9,-83.2,-196.7,-13.6,-80.1,10.3,-59.9
```

x(145,1)=-74.6,-104.1,52.8,-6.6,25.7,99.5,46.2,-132.6
x(153,1)=52.2,-112.6,-39.4,-87.2,135.9,-73.8,-41.3,-113.6
x(161,1)=-104.5,-81.1,45.2,-22.2,13.6,55.2,60.4,109.5
x(169,1)=-43.5,109.4,-11.6,62.9,87.7,55.5,-53.9,-32.8
x(177,1)=2.5,-82.3,21.4,24.6,-75.6,36.2,-54.1,48.4
x(185,1)=-98.7,-8.7,-28.2,46.9,0.0,0.0,0.0,0.0
x(1,2)=10.1,-23.6,36.4,93.1,-17.0,-145.4,-28.0,48.6
x(9,2)=33.6,12.9,-81.9,32.7,15.3,9.7,-113.0,123.1
x(17,2)=-36.8,68.9,0.3,-15.8,89.6,-7.6,67.0,76.4
x(25,2)=61.7,43.3,-41.5,47.1,67.9,-100.6,6.4,79.8
x(33,2)=-56.9,75.7,-75.5,42.5,53.0,-90.7,121.8,26.0
x(41,2)=24.5,126.9,-56.1,-3.1,89.8,95.7,22.8,98.7
x(49,2)=-82.0,-132.2,-124.0,50.1,-66.2,-120.5,-10.0,64.0
x(57,2)=-91.8,74.4,-13.4,12.1,-88.9,101.9,-83.5,69.7
x(65,2)=-51.3,-123.5,40.6,28.7,-17.7,-71.6,-79.1,9.1
x(73,2)=86.4,-104.2,147.4,-6.9,22.2,-16.3,62.5,57.4
x(81,2)=-22.9,-61.8,84.4,41.3,-34.9,5.6,84.4,-66.1
x(89,2)=16.9,-98.4,73.2,64.5,55.1,-60.6,-20.6,-82.9
x(97,2)=86.9,-20.0,61.4,81.7,-56.3,49.5,7.3,96.6
x(105,2)=94.8,91.7,-51.9,-37.7,113.6,85.0,-76.4,-117.1
x(113,2)=20.8,138.8,-78.0,-60.8,15.7,-38.5,52.1,104.3
x(121,2)=130.6,89.3,149.4,-35.9,135.2,73.7,-136.1,-101.5
x(129,2)=-112.1,36.4,123.9,81.8,61.1,-104.7,83.5,69.5
x(137,2)=97.0,-40.2,69.4,54.8,113.1,105.9,-62.1,62.1
x(145,2)=33.3,-98.1,-56.4,138.6,67.8,-88.6,43.4,-1.6
x(153,2)=-14.0,-32.7,134.8,73.4,60.2,-123.3,59.1,20.4
x(161,2)=69.9,94.5,122.1,2.9,-3.0,-81.2,86.2,-54.8
x(169,2)=-70.3,-76.7,23.2,2.3,-94.6,-87.8,71.5,-63.1
x(177,2)=38.5,28.6,43.1,-74.2,87.0,-66.1,111.8,-117.5
x(185,2)=-9.0,-168.9,63.4,-52.9,0.0,0.0,0.0,0.0
x(1,3)=18.4,-55.2,32.7,-79.7,62.2,-98.3,52.4,-63.4
x(9,3)=1.0,106.4,-6.6,-77.1,152.9,73.4,54.9,31.2
x(17,3)=8.0,43.2,35.3,10.5,-83.5,102.3,-64.0,-38.9
x(25,3)=-32.5,-62.2,105.9,-70.9,-111.8,-43.8,-194.2,-18.5
x(33,3)=5.6,-9.6,-61.8,-70.7,-31.6,-128.7,60.8,-28.8
x(41,3)=-18.2,10.7,2.6,124.1,-62.0,-24.5,10.3,47.8
x(49,3)=-65.5,12.2,17.3,-56.6,53.8,1.0,-77.1,48.8
x(57,3)=45.2,40.4,38.7,49.5,4.6,188.0,21.2,-45.9
x(65,3)=-22.4,26.1,38.3,-36.2,61.5,15.2,-12.3,78.8
x(73,3)=20.9,120.8,-28.7,158.4,13.4,49.3,2.9,-70.1
x(81,3)=10.2,-53.3,40.8,-23.0,67.9,-0.3,-56.6,41.5
x(89,3)=-101.8,7.2,46.7,52.9,21.9,34.9,-138.2,23.2
x(97,3)=-65.6,25.0,-16.9,-101.2,11.3,-77.9,-3.7,23.4
x(105,3)=-46.9,-32.2,87.3,23.3,66.3,-95.7,60.6,93.1
x(113,3)=-126.3,-57.7,23.8,110.3,129.7,35.3,-57.2,23.7
x(121,3)=11.8,25.9,-81.5,-35.2,7.0,-58.8,-2.2,33.8

x(129,3)=-29.6,78.7,62.1,-23.1,-35.2,-19.6,-38.9,-73.6
x(137,3)=3.9,-119.2,-34.2,68.1,-32.1,-54.6,53.8,10.2
x(145,3)=-56.8,140.3,13.3,43.5,-72.9,16.3,-156.6,-4.7
x(153,3)=29.2,102.6,-18.7,4.5,-136.1,69.0,-14.2,140.5
x(161,3)=-45.6,-94.4,-19.8,-49.1,61.9,-44.1,-93.4,18.3
x(169,3)=73.2,27.4,-12.0,-155.0,-74.9,38.1,-19.3,-25.3
x(177,3)=-33.4,-78.9,-111.5,5.0,-10.8,110.1,-20.9,133.3
x(185,3)=-52.9,135.0,-80.4,-3.5,0.0,0.0,0.0,0.0
x(1,4)=-33.7,-41.2,-29.9,-95.6,84.9,12.3,243.3,-340.3
x(9,4)=-223.6,295.1,120.5,-265.3,102.0,242.1,166.9,-305.3
x(17,4)=150.5,-173.7,205.0,313.7,-158.0,-3.5,-121.9,-137.6
x(25,4)=-269.7,-284.0,245.3,-94.9,-182.4,171.4,-44.5,-193.1
x(33,4)=309.9,-175.7,327.4,-267.8,-325.9,-35.8,-269.6,-339.0
x(41,4)=-307.2,-266.5,252.7,278.0,-85.0,-267.5,-299.9,-168.7
x(49,4)=234.7,252.0,178.6,-282.1,192.4,227.0,1.2,-254.6
x(57,4)=196.6,-225.2,316.5,340.8,265.8,137.8,286.3,-149.6
x(65,4)=120.9,83.0,-253.1,-286.5,318.4,179.6,321.6,71.6
x(73,4)=-148.3,184.5,-164.6,187.0,-242.4,231.0,-265.9,-191.6
x(81,4)=246.3,263.1,-70.8,-293.0,-128.7,-301.1,-127.3,246.7
x(89,4)=128.7,81.7,-242.8,-193.6,-199.1,170.6,-345.1,209.5
x(97,4)=-341.7,384.8,-242.5,-267.5,221.5,-305.9,-273.5,-259.9
x(105,4)=-164.8,-168.0,285.1,324.3,-173.8,-249.0,230.8,213.7
x(113,4)=-21.6,-50.5,172.5,182.9,79.1,294.8,-148.4,-225.8
x(121,4)=-229.6,-217.4,-168.0,185.8,-176.4,-264.6,173.8,114.0
x(129,4)=207.5,-51.6,-235.5,-220.1,-263.6,235.1,-220.8,-192.4
x(137,4)=-276.4,-16.5,-285.2,-106.4,-202.1,-253.5,279.9,-210.8
x(145,4)=-284.9,5.5,219.8,-196.2,-260.4,217.5,-111.0,-248.2
x(153,4)=303.7,21.3,-204.2,-198.8,135.3,255.3,-260.4,-98.1
x(161,4)=-325.3,-296.2,-237.5,-339.2,276.9,106.0,-129.9,303.1
x(169,4)=189.1,179.8,-329.5,-149.0,201.3,265.3,-313.7,259.2
x(177,4)=-265.7,-350.9,-255.6,368.5,-348.6,385.7,-394.2,305.4
x(185,4)=-461.9,300.0,-415.6,-1954.8,0.0,0.0,0.0,0.0
y(1,1)=-36.4,15.6,-32.5,17.2,60.5,107.0,83.4,-99.5
y(9,1)=-48.2,-25.4,93.4,-83.2,-6.1,53.0,35.4,-67.9
y(17,1)=73.2,-34.6,84.2,41.7,-73.0,94.5,-50.2,-6.1
y(25,1)=-116.0,-38.6,42.6,-136.9,-90.9,109.1,-48.5,-74.8
y(33,1)=17.8,-105.2,56.7,-151.5,-131.2,-78.5,-49.3,-125.5
y(41,1)=-61.0,11.4,131.8,77.7,-123.7,-19.1,-64.6,-111.4
y(49,1)=134.1,27.4,81.2,-18.7,117.9,95.5,-79.9,-22.1
y(57,1)=57.3,-28.7,144.4,109.2,91.1,125.6,21.8,-115.7
y(65,1)=44.6,122.1,-15.3,-63.3,114.0,146.2,84.0,-50.0
y(73,1)=-110.0,50.1,-78.6,159.4,-40.4,149.1,-101.4,-119.9
y(81,1)=65.9,95.3,-122.3,-14.6,5.8,-95.7,-111.5,154.3
y(89,1)=42.1,48.8,-31.4,-123.8,-115.5,69.8,-122.8,127.9
y(97,1)=-115.4,83.3,-128.6,-86.5,118.2,-80.8,-143.4,-69.2
y(105,1)=-118.3,-110.3,86.5,112.3,-159.8,-73.5,83.6,71.5

y(113,1)=-54.9,-99.7,108.8,126.6,121.4,109.4,-210.9,-90.1
y(121,1)=-107.7,-140.5,-94.3,82.3,-52.3,-135.8,139.3,130.9
y(129,1)=136.8,-48.7,-67.9,-41.6,-114.0,111.9,-139.0,-62.4
y(137,1)=-90.6,-70.7,-144.4,15.5,-118.1,-126.4,92.5,-92.2
y(145,1)=-134.3,-51.1,121.2,-56.4,-161.7,86.2,-101.0,-85.9
y(153,1)=95.5,154.5,-197.3,-84.9,29.5,108.3,-161.0,47.1
y(161,1)=-110.0,-81.3,-141.8,-103.8,125.6,127.0,-137.7,90.4
y(169,1)=112.9,149.3,-114.5,-65.3,125.5,140.0,-121.2,113.3
y(177,1)=-196.1,-119.5,-111.1,153.0,-123.8,179.7,-115.0,144.7
y(185,1)=-117.2,143.5,-160.9,-38.9,0.0,0.0,0.0,0.0
y(1,2)=30.3,19.4,22.3,-32.9,-46.4,70.4,13.4,18.6
y(9,2)=101.3,-73.3,17.5,-33.3,-97.9,10.5,-7.0,-69.3
y(17,2)=130.0,3.7,-34.7,-0.1,-2.0,-35.6,24.5,64.5
y(25,2)=4.2,-39.3,44.4,-67.3,27.5,-3.8,63.8,5.1
y(33,2)=7.0,-29.0,-36.6,33.9,-14.4,120.6,-51.0,-60.6
y(41,2)=83.1,86.9,-49.1,39.7,114.1,8.9,53.9,1.4
y(49,2)=-33.9,-45.4,26.1,4.6,92.5,83.2,90.2,-65.5
y(57,2)=18.2,-14.7,49.8,1.9,-72.8,-82.9,-108.0,88.6
y(65,2)=146.9,74.5,-26.9,15.9,45.7,-77.9,52.0,-145.1
y(73,2)=71.6,24.2,-20.7,79.1,-90.2,24.7,58.5,1.7
y(81,2)=-34.9,41.4,-93.8,46.8,-39.9,-93.3,-56.6,-29.8
y(89,2)=14.1,17.3,99.7,-117.8,-56.4,53.2,-10.9,-25.5
y(97,2)=-50.2,-17.2,33.1,61.7,-48.0,105.4,-97.3,-54.4
y(105,2)=8.6,43.9,-25.9,83.7,-18.0,73.8,-10.5,-58.4
y(113,2)=123.7,55.6,-5.6,-51.2,-139.5,79.6,-26.4,58.8
y(121,2)=-33.1,-44.9,41.0,-77.4,-31.7,-55.4,77.4,-61.9
y(129,2)=10.6,-94.2,22.8,161.0,-10.4,7.5,-87.0,55.4
y(137,2)=-40.3,86.9,24.9,67.0,12.3,23.4,-6.2,-92.2
y(145,2)=6.3,-71.0,1.9,17.1,4.6,-13.9,-49.5,38.7
y(153,2)=4.1,-104.4,-8.2,9.0,86.7,-49.8,-3.2,-84.6
y(161,2)=60.9,62.8,69.5,83.5,-110.0,29.3,131.3,-102.6
y(169,2)=-8.0,11.0,-39.1,113.2,11.3,-2.2,62.7,-39.5
y(177,2)=-6.4,-13.0,-59.6,42.7,22.5,11.9,-2.1,-3.4
y(185,2)=30.9,-62.5,42.1,80.4,0.0,0.0,0.0,0.0
y(1,3)=117.8,-153.1,71.9,74.1,-84.1,-86.4,-29.1,14.9
y(9,3)=94.6,-135.6,-86.9,42.7,-34.8,-111.3,-90.3,20.3
y(17,3)=-41.7,125.5,-87.0,-70.6,23.6,-56.3,95.8,161.8
y(25,3)=8.6,124.2,-111.0,2.5,41.0,-45.9,93.3,151.8
y(33,3)=-86.7,118.8,-82.1,27.0,17.1,62.6,52.0,26.9
y(41,3)=84.6,155.2,-45.6,-82.2,108.8,122.6,112.2,92.3
y(49,3)=-49.2,-98.0,-97.8,134.5,-78.4,-94.0,143.1,96.1
y(57,3)=-103.3,123.3,-8.3,-35.1,-88.9,-10.1,-79.1,168.4
y(65,3)=-90.4,-139.4,157.6,90.0,-20.4,-78.6,-43.1,8.3
y(73,3)=116.3,-103.2,101.3,-23.9,97.4,-37.3,79.9,53.9
y(81,3)=-108.7,-64.2,82.5,140.1,-9.6,32.9,44.0,12.9
y(89,3)=-78.4,-156.6,117.1,67.7,84.4,-149.9,120.2,-113.9

```
y(97,3)=56.7,-96.2,87.9,86.7,-97.0,80.1,101.8,86.3
y(105,3)=152.4,142.1,-100.1,-75.6,91.0,93.6,-127.2,-155.1
y(113,3)=82.7,115.7,-84.2,-77.1,-4.6,-98.7,97.1,155.8
y(121,3)=90.8,89.3,103.6,-134.5,118.0,60.1,-108.2,-186.4
y(129,3)=-85.3,17.8,132.9,159.3,81.8,-85.6,102.4,115.2
y(137,3)=76.6,21.1,73.3,103.9,111.9,68.4,-125.2,127.9
y(145,3)=67.9,17.0,-115.0,156.7,40.2,-122.0,101.9,109.8
y(153,3)=-118.5,-75.7,33.2,138.5,-45.8,-52.8,82.3,120.3
y(161,3)=113.1,114.9,56.1,126.0,-145.9,-148.4,64.3,-135.4
y(169,3)=-115.4,-111.3,115.3,37.8,-91.1,-84.5,146.8,-172.3
y(177,3)=93.9,139.5,133.9,-105.7,129.3,-54.9,138.5,-108.4
y(185,3)=154.2,-117.6,154.7,33.9,0.0,0.0,0.0,0.0
y(1,4)=39.7,-169.5,2.0,37.2,148.1,102.4,197.3,-125.0
y(9,4)=-51.3,140.9,-35.4,9.6,126.2,93.5,39.2,-16.6
y(17,4)=-22.0,-133.9,55.2,-109.1,-155.7,146.5,-74.8,118.3
y(25,4)=-28.7,137.9,-16.6,-244.0,-242.0,152.8,-176.5,136.0
y(33,4)=-241.5,29.8,-103.4,-51.2,-61.8,-223.0,1.7,-186.3
y(41,4)=10.9,27.3,-28.3,115.6,-188.0,17.7,-44.1,-147.7
y(49,4)=-76.4,42.0,74.5,59.7,126.5,-39.5,-189.4,72.2
y(57,4)=111.6,163.9,-11.4,-59.4,31.2,147.3,34.4,-23.1
y(65,4)=-207.8,-71.3,16.1,111.0,103.4,198.8,34.9,161.9
y(73,4)=-24.5,68.1,24.0,274.5,74.2,-2.8,-6.6,-177.4
y(81,4)=35.0,63.7,66.5,69.6,201.6,33.3,-229.4,102.8
y(89,4)=-141.0,146.7,158.1,30.2,113.8,14.0,76.3,37.6
y(97,4)=-1.8,-29.8,-169.4,33.2,36.0,5.9,98.5,24.5
y(105,4)=26.8,-121.1,91.9,14.0,-69.6,-93.5,-50.9,10.4
y(113,4)=-174.7,-82.2,-115.3,41.4,110.0,20.5,7.3,-36.8
y(121,4)=10.0,-14.0,8.1,-182.8,56.1,62.4,-33.3,-190.1
y(129,4)=46.9,213.8,30.5,-7.6,-91.3,-18.4,67.2,-142.0
y(137,4)=93.2,-255.1,-44.2,293.9,-52.4,33.2,-15.4,19.0
y(145,4)=-1.4,242.0,17.2,-9.6,-80.8,-21.5,-228.9,217.5
y(153,4)=51.1,184.3,6.1,184.9,-169.9,101.2,-41.2,211.8
y(161,4)=14.6,15.2,-117.1,49.0,142.8,-215.4,-95.0,-152.8
y(169,4)=159.1,-118.4,4.3,-224.1,-132.5,-111.5,-6.4,8.1
y(177,4)=-153.9,176.4,-237.4,-51.6,157.8,109.4,-24.6,178.7
y(185,4)=50.2,185.4,-39.1,70.9,0.0,0.0,0.0,0.0
*Do,j,1,particle_number(1),1
x(j,1)=0.001*x(j,1)
x(j,2)=0.001*x(j,2)
x(j,3)=0.001*x(j,3)
x(j,4)=0.001*x(j,4)
y(j,1)=0.001*y(j,1)
y(j,2)=0.001*y(j,2)
y(j,3)=0.001*y(j,3)
y(j,4)=0.001*y(j,4)
*enddo
```

```
!
! Thickness of Particles
!
particle_thickness(1)=66.60,33.11,44.89,60.60,89.83,33.51,31.95,25.11
particle_thickness(9)=47.30,96.69,45.79,33.01,34.09,90.33,40.99,27.95
particle_thickness(17)=20.81,66.49,54.80,45.47,40.38,58.59,103.76,91.56
particle_thickness(25)=37.11,44.89,99.82,39.39,60.83,38.76,58.87,44.94
particle_thickness(33)=42.37,43.67,87.38,38.12,65.19,43.35,68.18,94.61
particle_thickness(41)=80.53,49.88,101.91,68.03,91.90,24.87,108.56,33.19
particle_thickness(49)=104.82,65.27,44.59,85.48,68.00,79.52,93.69,83.01
particle_thickness(57)=32.30,69.73,32.08,91.28,49.04,49.63,70.15,54.90
particle_thickness(65)=57.44,38.01,50.60,101.21,34.39,81.78,41.07,98.82
particle_thickness(73)=84.18,39.80,106.45,64.17,47.79,35.87,31.17,59.79
particle_thickness(81)=53.34,89.20,32.58,32.62,34.36,74.90,63.91,27.76
particle_thickness(89)=68.31,31.71,51.83,28.18,39.05,33.79,76.57,61.50
particle_thickness(97)=32.22,85.39,25.09,35.08,36.22,47.15,56.10,36.03
particle_thickness(105)=27.80,71.98,86.67,50.42,46.24,35.33,55.00,51.68
particle_thickness(113)=55.77,61.73,58.91,73.39,89.43,39.23,71.06,35.95
particle_thickness(121)=32.97,30.29,24.47,65.22,60.97,50.29,84.23,34.24
particle_thickness(129)=64.54,46.79,34.71,23.06,32.26,64.32,29.29,47.21
particle_thickness(137)=56.18,76.28,67.22,52.40,59.05,51.98,71.67,63.99
particle_thickness(145)=34.30,41.37,49.29,50.31,47.96,31.11,43.96,42.62
particle_thickness(153)=91.71,45.21,58.05,46.80,86.66,104.28,95.61,79.84
particle_thickness(161)=68.18,82.69,72.92,42.32,73.72,38.44,86.98,30.86
particle_thickness(169)=35.50,57.13,56.82,56.99,48.85,74.32,87.01,68.25
particle_thickness(177)=55.00,46.54,26.44,32.28,32.62,24.36,49.13,54.71
particle_thickness(185)=61.33,31.85,99.99,50.71,0.00,0.00,0.00,0.00
!
! Orientation of Particles
!
x_rotation(1)=358.52,114.25,260.68,159.67,289.40,41.57,48.09,295.18
x_rotation(9)=218.34,320.50,85.31,118.08,191.23,340.86,186.13,31.95
x_rotation(17)=259.54,193.29,61.92,137.43,191.24,17.33,239.64,119.46
x_rotation(25)=171.50,212.43,317.74,186.38,205.58,18.15,235.13,134.35
x_rotation(33)=22.25,38.64,333.78,61.37,51.20,114.66,308.15,358.05
x_rotation(41)=70.71,20.81,119.17,45.91,60.89,309.29,67.67,129.34
x_rotation(49)=41.83,213.57,342.96,256.88,266.50,1.91,58.61,123.82
x_rotation(57)=11.52,48.33,284.21,113.89,37.87,320.10,336.56,18.51
x_rotation(65)=63.80,238.42,33.47,203.45,243.06,220.15,87.26,227.64
x_rotation(73)=43.44,208.02,198.47,134.57,248.57,261.67,269.95,279.67
x_rotation(81)=274.05,205.78,70.29,7.47,56.76,340.15,159.97,188.21
x_rotation(89)=341.75,148.60,356.14,270.14,289.11,117.63,216.45,219.28
x_rotation(97)=43.60,211.55,265.67,153.65,219.71,318.81,43.93,12.79
x_rotation(105)=265.66,44.22,223.35,226.43,281.03,272.65,307.67,183.36
x_rotation(113)=283.75,216.61,141.16,168.48,237.95,127.70,57.95,276.87
x_rotation(121)=225.49,53.98,244.32,44.41,340.41,113.29,4.82,59.56
```

x_rotation(129)=184.49,287.81,194.81,69.98,16.41,236.36,118.44,240.18
x_rotation(137)=46.72,285.66,165.25,245.92,182.08,155.35,336.04,345.73
x_rotation(145)=357.08,223.20,182.59,144.31,54.52,43.05,54.28,343.93
x_rotation(153)=209.93,294.92,145.56,282.49,62.60,163.85,1.47,191.31
x_rotation(161)=234.81,251.35,347.68,160.92,155.37,78.89,316.80,39.68
x_rotation(169)=216.32,288.66,289.28,190.87,173.67,60.57,186.29,275.78
x_rotation(177)=216.75,121.77,106.87,152.21,16.28,234.28,71.30,89.52
x_rotation(185)=345.50,208.71,175.46,210.62,0.00,0.00,0.00,0.00
y_rotation(1)=145.34,343.42,352.99,257.51,2.19,359.15,97.77,349.77
y_rotation(9)=15.10,36.23,245.17,100.66,43.70,328.32,217.01,80.74
y_rotation(17)=198.82,343.55,283.22,100.83,188.42,172.77,134.12,268.15
y_rotation(25)=294.87,86.19,118.29,257.73,192.49,47.37,101.18,145.11
y_rotation(33)=141.81,127.02,180.84,290.83,282.99,26.03,258.56,267.88
y_rotation(41)=345.95,349.64,11.88,323.78,333.02,185.87,218.23,287.11
y_rotation(49)=36.37,33.92,115.21,77.45,235.67,151.50,225.63,203.18
y_rotation(57)=351.76,247.46,153.86,99.31,98.80,260.55,291.74,212.76
y_rotation(65)=117.27,52.71,97.83,237.87,102.95,339.35,321.14,214.47
y_rotation(73)=338.05,22.25,196.07,36.13,48.86,29.83,169.49,142.41
y_rotation(81)=191.90,90.68,188.49,350.23,194.90,260.46,249.23,332.83
y_rotation(89)=45.98,12.92,290.14,129.23,75.29,266.15,263.04,243.85
y_rotation(97)=274.41,120.87,289.34,56.66,176.06,100.04,228.83,106.46
y_rotation(105)=162.81,140.23,267.38,77.86,62.97,162.66,316.39,348.10
y_rotation(113)=345.41,294.86,136.65,20.41,346.82,142.93,282.73,93.03
y_rotation(121)=134.19,24.81,167.53,197.73,64.05,56.30,196.95,345.33
y_rotation(129)=131.72,129.51,345.51,314.44,127.16,327.92,288.40,61.57
y_rotation(137)=54.15,264.62,34.77,298.32,93.24,125.85,127.26,212.51
y_rotation(145)=99.23,19.03,66.57,181.04,115.56,212.55,143.35,261.95
y_rotation(153)=83.18,145.73,207.46,169.27,254.72,279.10,352.22,348.90
y_rotation(161)=244.77,194.93,148.00,39.82,206.57,238.68,46.10,83.43
y_rotation(169)=161.19,189.25,261.70,101.02,276.45,207.05,314.74,249.75
y_rotation(177)=62.83,206.59,243.29,48.96,260.60,171.30,176.85,63.16
y_rotation(185)=183.01,3.03,232.24,333.89,0.00,0.00,0.00,0.00
z_rotation(1)=3.35,189.02,297.40,88.87,288.18,101.82,293.52,23.72
z_rotation(9)=17.88,232.40,141.37,56.70,82.39,275.91,195.03,56.83
z_rotation(17)=198.66,263.74,341.46,29.32,291.19,4.99,169.73,205.96
z_rotation(25)=23.59,222.93,71.58,355.93,44.91,72.94,78.12,342.15
z_rotation(33)=83.15,136.22,37.02,18.12,320.80,33.74,220.48,253.45
z_rotation(41)=192.49,111.21,78.58,248.07,205.45,298.81,3.50,162.83
z_rotation(49)=216.73,195.24,114.22,268.24,228.92,91.49,93.70,254.27
z_rotation(57)=27.65,200.07,290.87,267.40,47.13,194.54,184.46,38.15
z_rotation(65)=83.12,334.29,271.18,340.38,253.75,200.99,88.59,331.06
z_rotation(73)=204.45,220.60,182.06,166.01,117.20,256.43,174.21,176.78
z_rotation(81)=66.43,157.05,163.79,128.53,128.10,283.29,336.86,296.86
z_rotation(89)=317.02,20.81,60.84,318.47,342.28,201.27,33.30,188.26
z_rotation(97)=233.03,321.18,49.67,213.35,240.99,302.85,330.62,354.20
z_rotation(105)=358.21,328.15,343.48,135.38,259.12,2.48,295.36,27.89

z_rotation(113)=114.54,195.27,190.16,147.18,326.09,343.87,102.24,284.23
z_rotation(121)=272.30,324.54,285.30,159.78,68.16,277.93,346.32,73.30
z_rotation(129)=354.71,160.34,137.31,9.16,306.07,295.80,172.24,329.05
z_rotation(137)=183.11,186.95,112.30,348.21,327.75,40.72,149.18,56.89
z_rotation(145)=268.88,30.77,71.09,154.66,281.62,1.93,343.84,86.13
z_rotation(153)=353.81,341.99,37.42,112.54,255.56,0.92,37.86,55.12
z_rotation(161)=223.13,122.85,213.94,2.00,297.62,347.18,115.76,152.12
z_rotation(169)=117.44,108.38,187.91,320.05,89.65,113.38,141.40,284.88
z_rotation(177)=157.85,84.32,65.47,16.26,183.26,114.21,8.32,168.99
z_rotation(185)=16.91,107.83,34.24,30.68,0.00,0.00,0.00,0.00
!
! Position of Particles Over An Area Of 100 μm × 100 μm
!
x_position(1)=8.95074847,-11.53808756,-
24.81938775,11.70908844,32.43762667,23.02487923,8.406933328,40.63081506
x_position(9)=31.77605594,9.435625066,-7.474067979,-33.85152557,-
7.71143109,9.852366876,19.59493133,13.85307583
x_position(17)=-43.11939009,3.086428069,-9.238080296,21.83589432,3.133390657,-
39.43707967,27.88022418,-40.91767142
x_position(25)=-34.63432824,-5.9914861,-4.257563431,1.805210836,13.77090981,-
25.92929645,-21.09354283,19.51404996
x_position(33)=-24.52098434,16.7832727,-
15.55375887,17.53320657,10.21704876,41.59912441,-3.755084076,-3.908363397
x_position(41)=-17.75281928,-2.864284629,-32.41255843,-2.651400703,-15.8875393,-
30.82547445,-25.71504017,-23.09384133
x_position(49)=-31.13380232,-40.88865363,18.33632433,-
7.427115813,14.76176302,13.57867105,-29.10650776,-26.3769423
x_position(57)=10.73039407,-4.127450635,27.02855148,16.20095984,34.19291527,-
24.35590078,8.224916453,36.99410324
x_position(65)=-18.19259245,43.98294703,-
2.053677505,4.471611053,4.3885934,2.249530578,-28.13233676,-39.03025355
x_position(73)=-9.542000414,-13.41838232,12.78963796,43.28535703,-
30.79716506,19.62663371,2.540440386,36.11398114
x_position(81)=-10.65436388,24.12579435,-15.22873287,8.609206723,-45.55459077,-
25.72146422,18.77960851,23.63400743
x_position(89)=18.3415867,-5.769458662,-16.91421198,-
22.97295766,32.1721185,38.77709543,26.91143874,30.85140959
x_position(97)=-12.26044552,29.0407218,-17.24345659,-
6.135501741,26.88542524,36.19804787,1.442345651,8.802605531
x_position(105)=-30.01371771,24.87057182,28.99630299,3.406412737,-
38.82942558,17.86523048,-31.0289594,-35.2391778
x_position(113)=35.07126743,42.96088668,8.279096518,37.90139046,-
49.94776246,11.25664695,2.768006934,30.13476055
x_position(121)=-0.19057088,7.466121913,23.8640292,-25.3265474,-
41.65171864,16.09445579,39.07521163,26.90290853

x_position(129)=42.83130623,-48.30170617,36.27107187,34.48556746,5.229134154,-46.80089842,-13.75885377,-1.043001082
x_position(137)=-37.69162525,-35.34850894,-45.73475891,-21.81331441,19.51630394,3.580105575,-37.60677224,35.29981553
x_position(145)=-22.97056677,6.497957074,-8.297104836,44.79331213,-39.42905734,-33.35395591,7.370976484,43.12013846
x_position(153)=23.78416538,36.0440563,48.43983122,28.55589893,-32.23975395,-36.6068749,43.91417061,-20.44661655
x_position(161)=-3.293181297,-47.47718185,5.903254499,-15.21208057,-44.57605156,16.2808062,39.84861378,48.84179288
x_position(169)=20.69174193,-21.21506552,-3.516005837,31.82040389,-32.18830461,-44.32953109,-16.41510253,-29.1053326
x_position(177)=17.53911773,41.21324742,24.55460737,6.186142528,9.721135034,-36.58770672,39.49416754,-25.75134411
x_position(185)=-5.827794294,39.7191351,-40.66294832,-4.394233316,0,0,0,0
y_position(1)=-27.38123202,8.298638275,-20.95593357,-23.47190902,48.26633997,-15.61229959,-39.22309848,37.96537245
y_position(9)=-23.92720009,-47.74874073,-18.72811132,-32.12338132,-40.57706611,-2.907574364,19.98878499,-46.63961639
y_position(17)=-18.04002648,15.44457078,31.99812228,46.86493302,-17.48543182,11.09586587,-7.654708104,-23.35285092
y_position(25)=-21.89946975,2.714274176,37.53715986,44.36226245,45.76939398,17.61223039,17.18081654,-43.20072315
y_position(33)=-27.59599692,34.43921565,28.05196527,-49.32846857,-11.32288055,-49.88489429,-7.565096018,27.01597286
y_position(41)=28.47392948,-46.42372667,22.17580334,-34.72787996,10.73892138,23.842684,41.7424342,26.55000166
y_position(49)=-21.25018269,7.620938066,4.659311459,14.44427814,17.90167541,44.51741131,20.92817027,-38.06037522
y_position(57)=-4.986230303,16.19447519,-14.97819866,-8.384141003,33.29168191,11.34607368,4.073933712,-23.52209735
y_position(65)=-38.07854589,14.5551875,13.9316961,14.73114803,22.10466206,49.37046241,-39.42017267,-43.6408629
y_position(73)=-5.162708793,26.35046408,27.19803856,47.2740854,-36.11257972,-40.61799732,3.034421839,-1.514666645
y_position(81)=17.14311397,2.005246739,-35.00027462,-23.78546823,25.49332672,-5.7597687,-14.07717896,-10.52925247
y_position(89)=20.40474303,-48.04223764,-7.569050317,-30.29462019,-7.007859062,-10.88170045,-10.3208483,25.5077099
y_position(97)=-28.3981084,44.93039118,17.12643705,33.35005956,-33.27464545,48.98721536,38.42810231,-34.52476513
y_position(105)=-9.304516286,32.55838158,-18.14757546,-41.00493212,-36.37074511,-0.482298091,-0.499417501,-44.50258531

```
y_position(113)=6.055952735,19.66672006,31.53972115,48.89116161,36.5438591,48.9950205
7,-2.047661479,-27.21570643
y_position(121)=40.08524885,34.51781851,8.598703583,16.64162173,12.59597852,22.975185
53,48.23032229,8.144648788
y_position(129)=8.009036576,-37.91404289,-1.570348879,-
29.0594916,12.98833851,11.47134191,-45.0467421,-30.74896039
y_position(137)=-29.45058291,-31.09278255,13.51979169,3.859667805,-0.088398652,-
5.48168347,-0.964270653,37.39274059
y_position(145)=-29.15386412,14.03118252,-29.40244845,-41.79287929,-
35.79588781,12.09586439,-44.79221097,22.86616817
y_position(153)=-43.65954993,43.4405119,35.89388167,1.337741859,-10.14105033,-
46.91104513,-19.86939354,-16.70637182
y_position(161)=14.81984065,34.22066124,35.40999493,-5.397335194,-32.28924662,-
16.91710048,-38.18448016,3.998209904
y_position(169)=49.94916201,-8.547746111,26.39570785,-39.97784598,-
14.03650865,2.188567366,-32.43309703,40.5153559
y_position(177)=-3.15318001,-39.59884252,23.62674556,-31.58059025,-20.00630099,-
28.73984666,-42.85471872,-44.62456078
y_position(185)=-48.67167995,-30.33418086,-19.26331004,-39.83306064,0,0,0,0
*Do,j,1,particle_number(1),1
particle_thickness(j)=particle_thickness(j)*0.001
x_position(j)=x_position(j)*0.001
y_position(j)=y_position(j)*0.001
*enddo
*Do,j,1,particle_number(1),1
/prep7
LOCAL,12,0,0,0,0,x_rotation(j),y_rotation(j),z_rotation(j)
!
! Creating the Geometry of Particles
!
CSYS,12
i=8*(j-1)+1
K,i,x(j,1),y(j,1)
K,i+1,x(j,2),y(j,2)
k,i+2,x(j,3),y(j,3)
k,i+3,x(j,4),y(j,4)
A,i,i+1,i+2,i+3
m=6*(j-1)+1
VEXT,m,,,0,0,particle_thickness(j)
CSYS,0
VSUM,fine
!
! Moving the Particles to the Desired Postition
!
*GET,x_centroid(j),VOLU,j,CENT,x
*GET,y_centroid(j),VOLU,j,CENT,y
```

```
*GET,z_centroid(j),VOLU,j,CENT,z
incx(j)=x_position(j)-x_centroid(j)
incy(j)=y_position(j)-y_centroid(j)
incz(j)=-z_centroid(j)
VGEN,2,j,,,incx(j),incy(j),incz(j),,1,1
!
! Defining the Material Model of Particles
!
ET,1,SOLID164
TYPE,1
EDMP,RIGID,j
MP,EX,j,3.03e5
MP,nuXY,j,0.21
MP,DENS,j,3.8e-3        ! Density (g/mm3)
TB,BISO,j
TBDATA,1,2108
TBDATA,2,0
MAT,j
LESIZE,all,,,1
!
! Meshing the Particles
!
VSWEEP,j
*enddo
*AFUN,DEG
finish
```

A.3 Evidence for the Ability of Thermal Softening to be Implemented into a Structural Analysis Using the Johnson Cook Material Model

A.3.1 LS-DYNA Manual

The following screenshot from the LS-DYNA manual implies that C_p (specific heat) can be used in a non-coupled analysis.

*MAT_JOHNSON_COOK ***MAT_015**

VARIABLE	DESCRIPTION
TR	Room temperature
EPSO	Quasi-static threshold strain rate. Ideally, this value represents the highest strain rate for which no rate adjustment to the flow stress is needed, and is input in units of 1/model time units. For example, if strain rate effects on the flow stress first become apparent at strain rates greater than 1E-02 seconds^{-1} and the system of units for the model input is kg, mm, msec, then EPSO should be set to 1E-05 [msec^{-1}]
CP	Specific heat (superseded by heat capacity in *MAT_THERMAL_*OPTION* if a coupled thermal/structural analysis)
PC	Failure stress or pressure cutoff (p_{min} < 0.0)

The following statements from the LS-DYNA manual (albeit from a section describing a different plasticity model) explains how temperature is calculated when a structural (non-coupled) analysis is run.

The final equation necessary to complete our description of high strain rate deformation is one which allows us to compute the temperature change during the deformation. In the absence of a coupled thermo-mechanical finite element code we assume adiabatic temperature change and follow the empirical assumption that 90 -95% of the plastic work is dissipated as heat. Hence,

$$\dot{T} = \frac{.9}{\rho C_v}\left(\sigma \cdot D^p\right),$$

where ρ is the density of the material and C_v the specific heat.

A.3.2 Evidence from papers in the literature

(i) Statement from [123]

"The J–C model could take into account the thermal softening that is essentially due to heat conversion of plastic work occurring at high strain-rate deformations. For $\dot{\varepsilon} \geq 10^2 s^{-1}$ both thermal conduction and convection can be neglected and thermal softening can be evaluated under adiabatic assumption. Given this last hypothesis and the further assumption of uniform stress, strain and temperature fields, the temperature can be analytically computed as a function of plastic work. **In LS-DYNA the evaluation of the change in temperature due to plastic work conversion is performed by the material routine in case of structural analysis only**. **In case of coupled thermo-structural analysis, the temperature calculation is managed by the thermal solver."**

(ii) Paper on modeling discontinuous chip formation using SPH [60]

They used SPH to simulate discontinuous chip formation **which requires thermal softening to be implemented**. However, there is no statement in the paper mentioning that a coupled thermal-structural analysis has been run for SPH. **In fact, since the paper came out in 2007, well before thermal/structural coupling was possible for SPH, they could not have done such an analysis**. Yet, if you look at the below Table, taken directly from the paper, it is clear that their structural SPH model took into account softening. I can only conclude that the SPH model is capable of simulating thermal softening in a structural analysis for which the temperature is calculated by the J-C model's routine.

Table 1. SPH and classical approach comparison [60]

	Lagrangian FE models	**SPH cutting model**
Large deformation process	Adaptative remeshing algorithm	SPH meshless nature
New free surfaces creation	Continuous remeshing and fracture model	Particles separation
Contact	Friction Coulomb approach	Particles interactions
Heat generation	**Fully thermomechanical coupling**	**Adiabatic**

(iii) Other papers on high speed impact simulation, e.g. [124]

Equation (5) in this paper shows the usual relationship to incorporate thermal softening when the adiabatic heat generation assumption is valid. There is no mention of a coupled thermal/structural analysis anywhere in the paper, nor is there any mention of initial temperatures. There are a number of other papers using LS-DYNA that similarly state implementing thermal softening with no mention of a coupled analysis.

A.3.3 Taylor bar impact FE simulations

Analyses a,b,c and d below are structural only. No initial temperature was prescribed to the elements for these analyses.

Analyses e, f and g are coupled thermal-structural.

a. **The Taylor bar impact was first modeled using Mat_98 (Simplified-Johnson-Cook). This material model does not contain the thermal term and J-C damage model.**

   The material card is below.

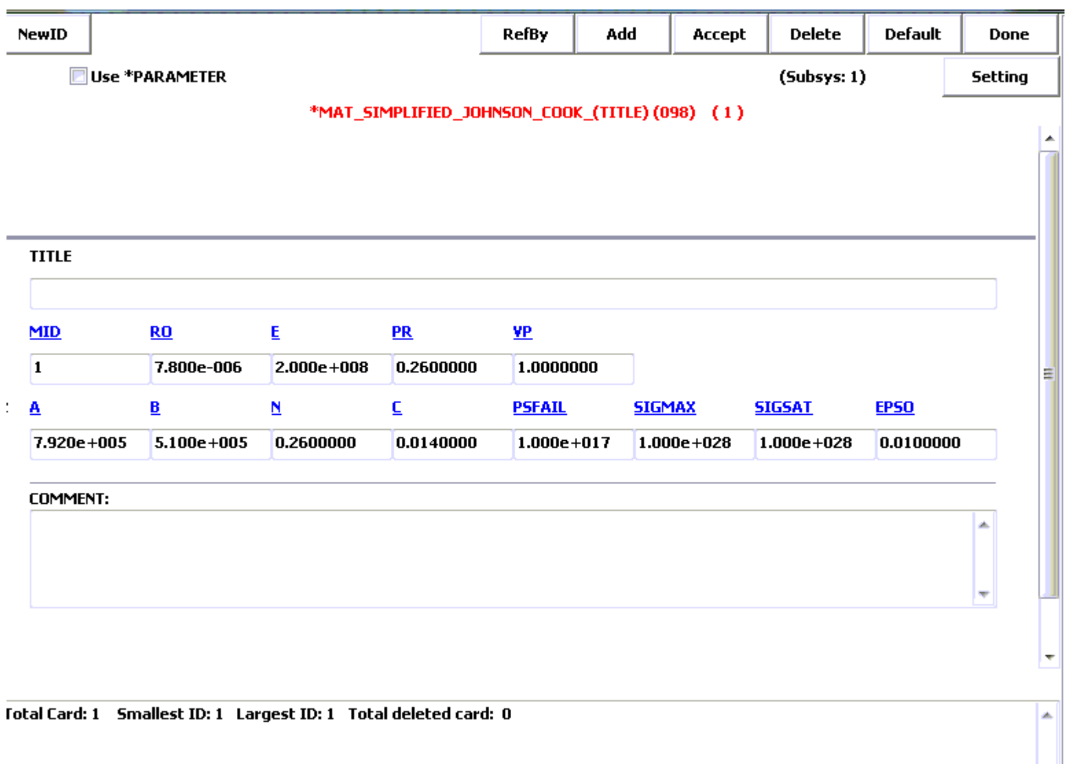

The resulting plastic strain contours are shown below.

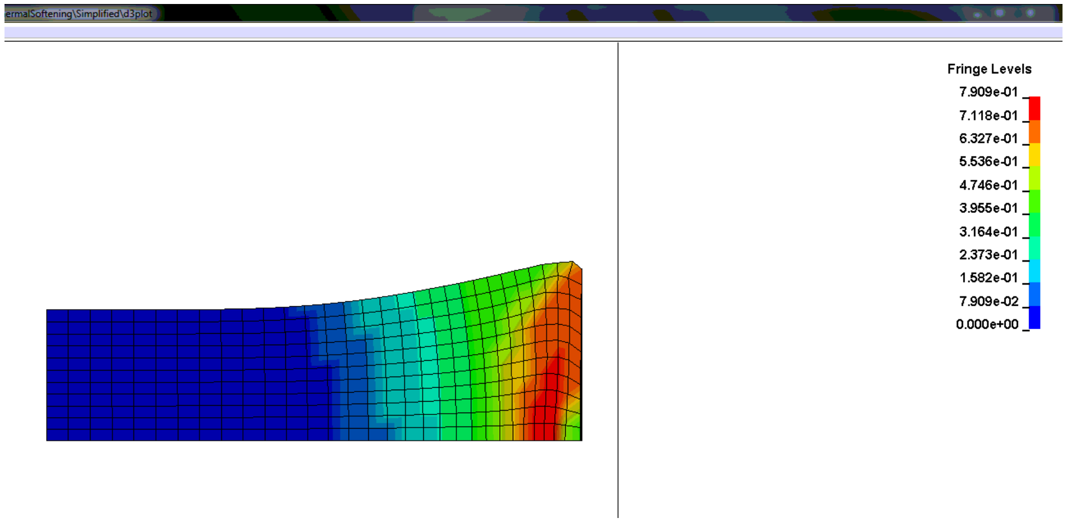

b. The Taylor impact was modeled using Mat_15 (Johnson-Cook). The m (thermal softening exponent) was set to 0 (this turns off softening). The material card is below.

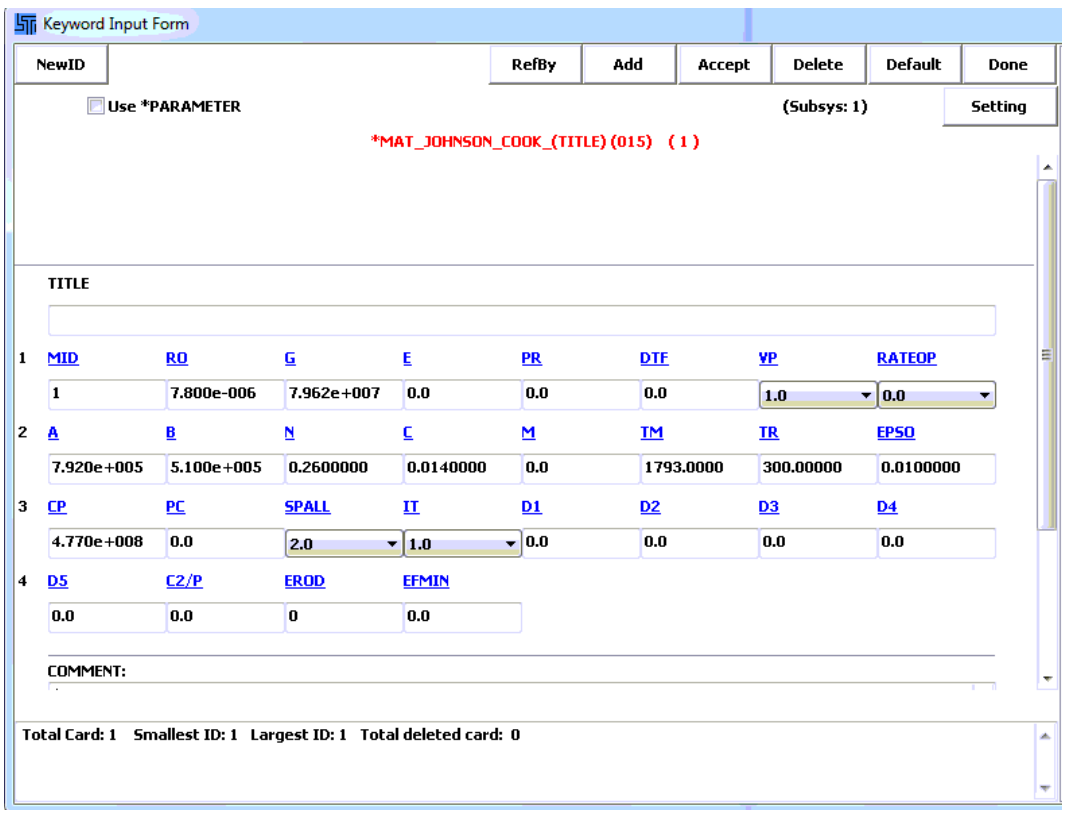

The resulting plastic strain contours are shown below.

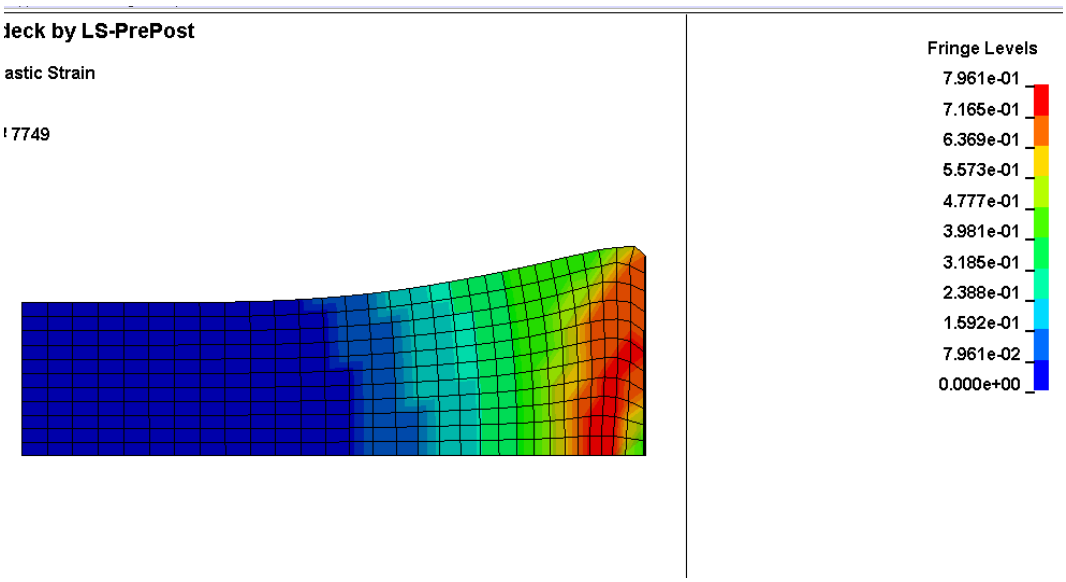

The Johnson-Cook material model (MAT_15) has its own history variables as listed in the link below. These variables are not saved in the output by default and are requested using *Extent-Binary card.

http://www.dynasupport.com/howtos/material/history-variables

The history variable #5 is the temperature change. While the following history plots for some of the elements at different locations along the bar show a temperature rise (T_{ref}=300 K) their effect was not reflected in the J-C equation because m=0.   Thus we get essentially similar deformation results to the previous case, with a small difference due to the hydrostatic stress effect, since the simplified-Johnson-Cook does not accept an Equation of state.

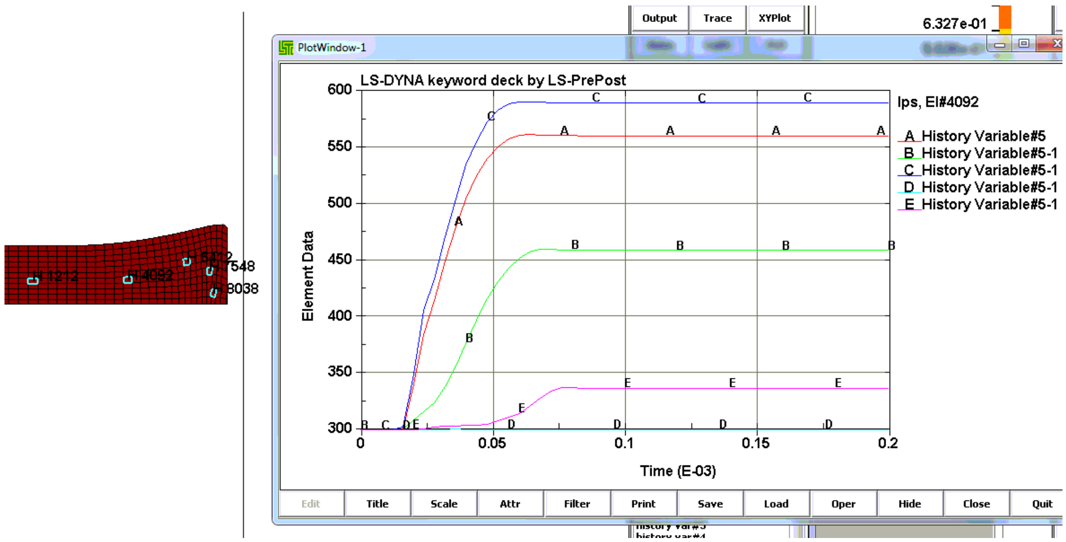

c. **m was set to 1.03 – we have now turned on thermal softening in the structural analysis. The material card is shown below.**

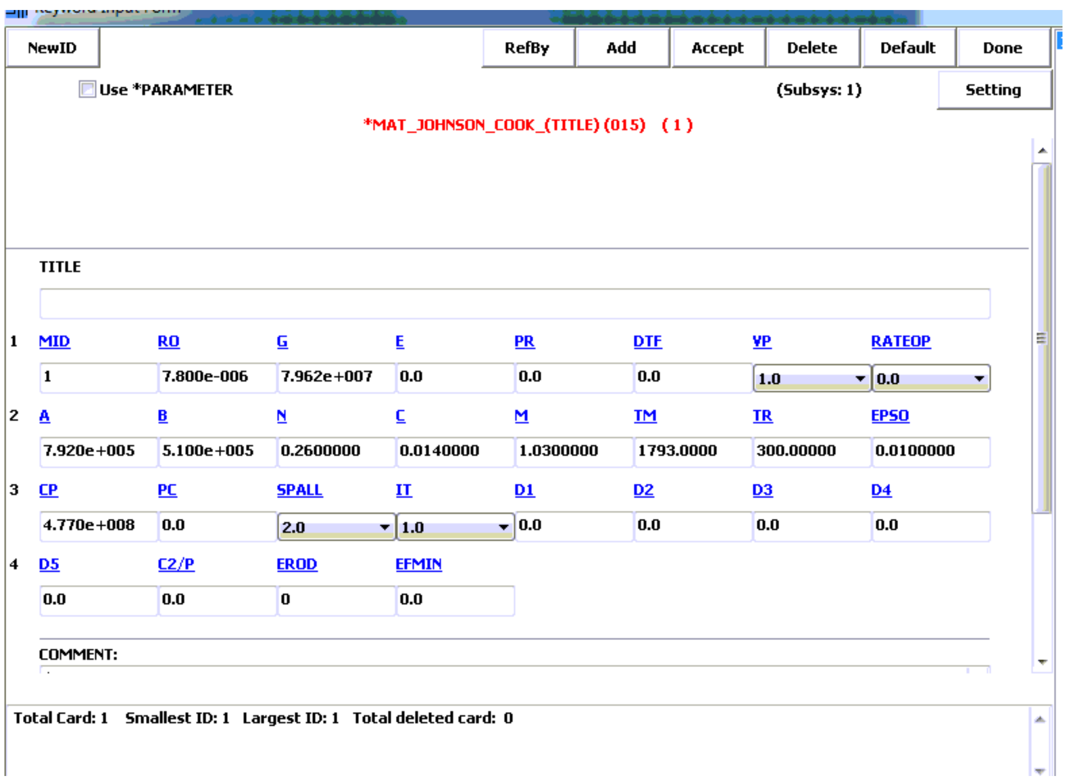

The resulting plastic contour clearly differs from the previous ones. The material softens and the resulting strains are higher. We can only conclude that the temperature has been updated in the J-C equation.

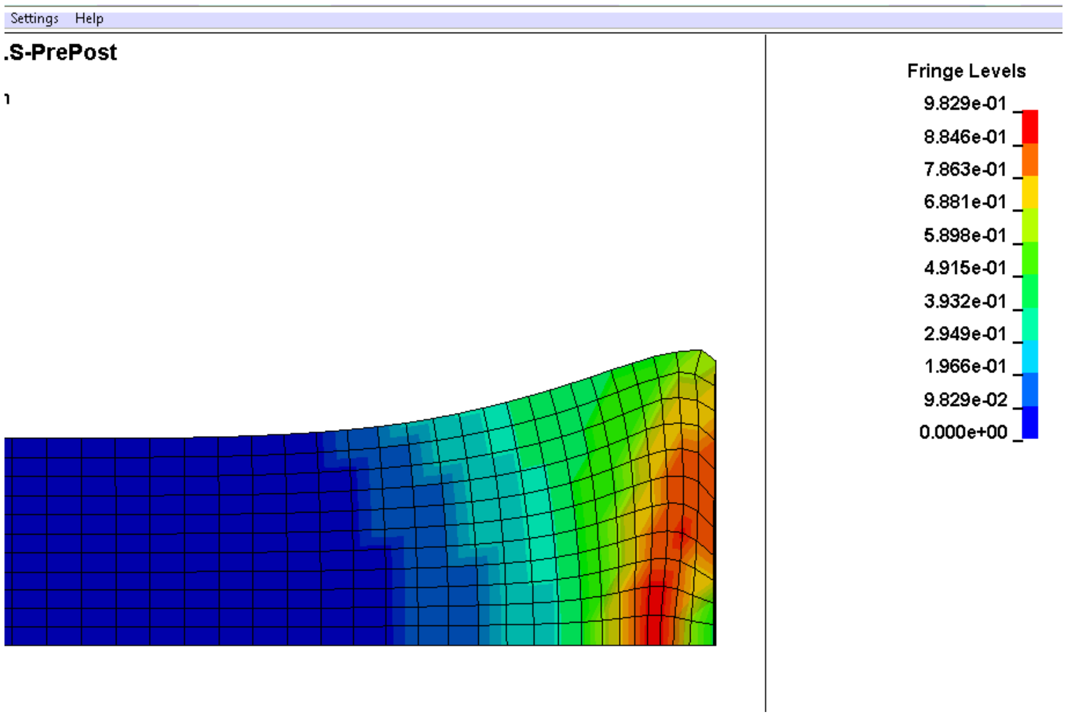

d. C_p (specific heat) was decreased 50% and the thermal softening exponent (m) was kept the same as the previous case. According to plastic conversion equation, this should result in higher temperature rise and a faster softening.

The plastic contour and temperature history are shown below. They agree with expectations. The evidence is even stronger that the elements' temperatures are calculated within the J-C model's routine and updated at each time step for this structural only analysis.

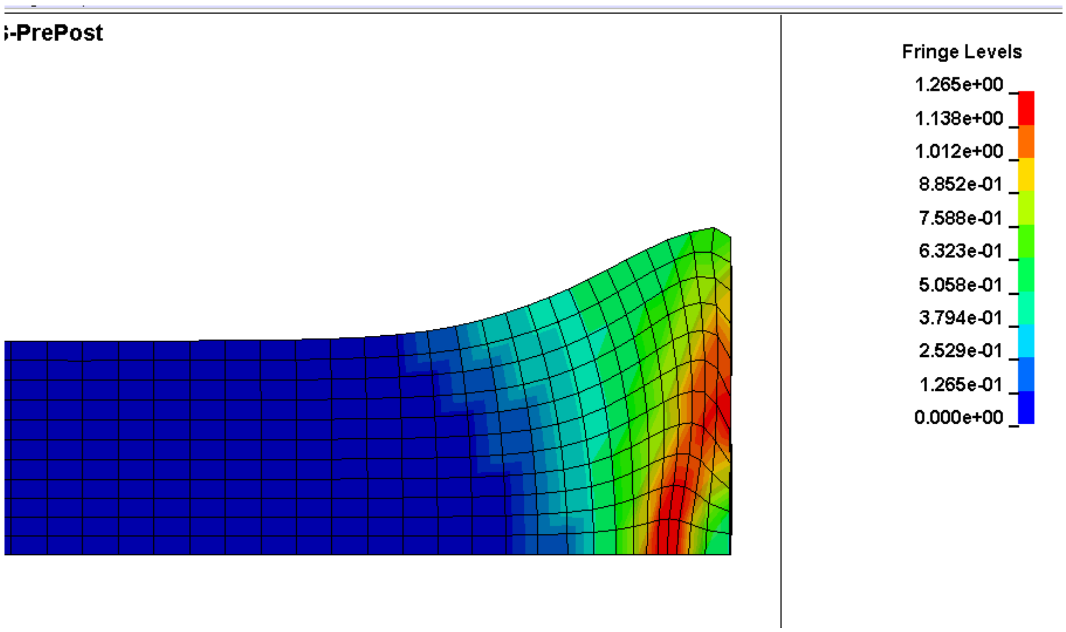

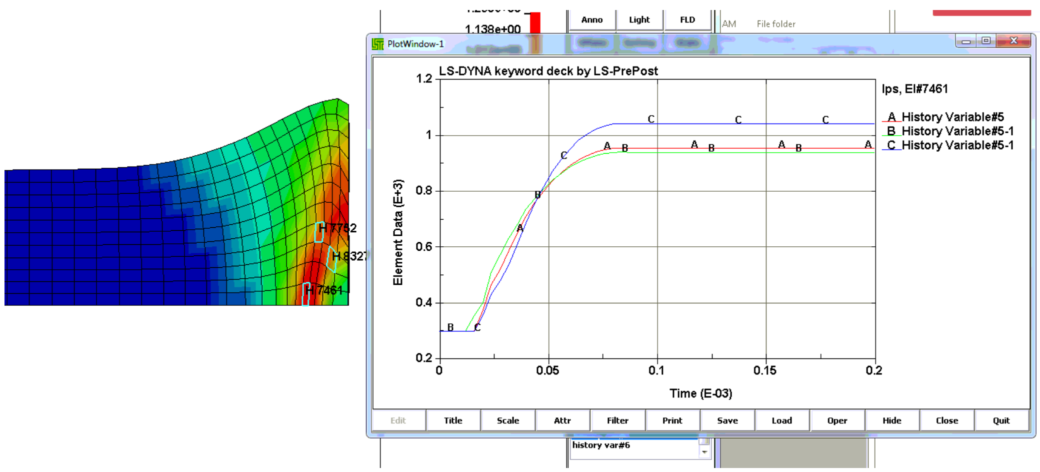

e. Coupled structural-thermal analysis with same J-C parameters as structural run (c) above.

Total analysis time= 2e-4

Structural time step= 1e-7

Thermal time step=1e-6

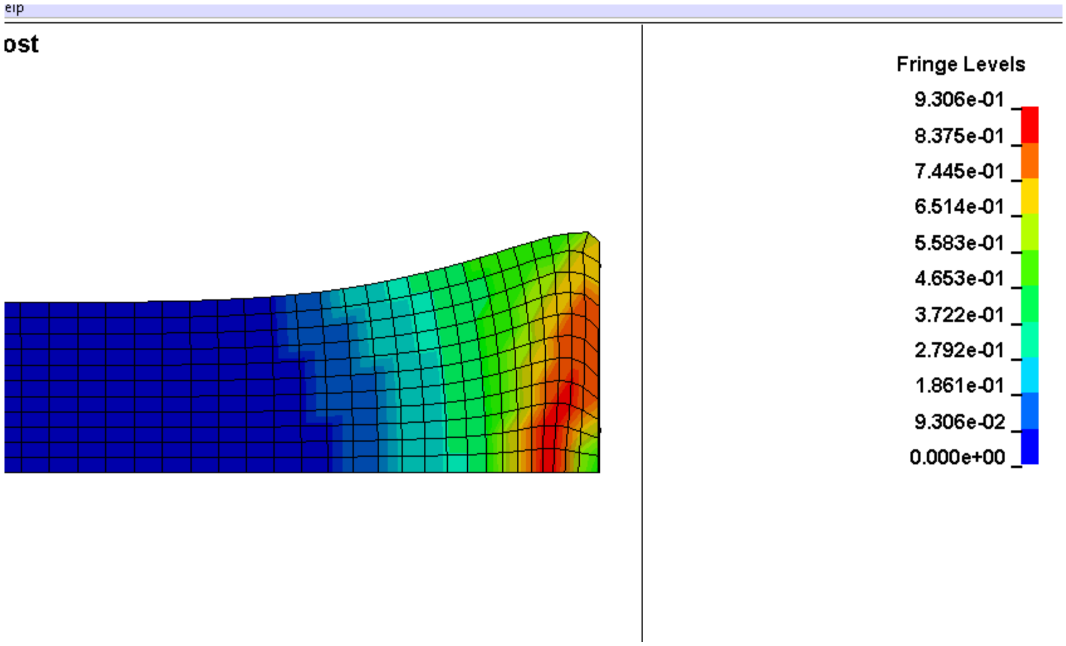

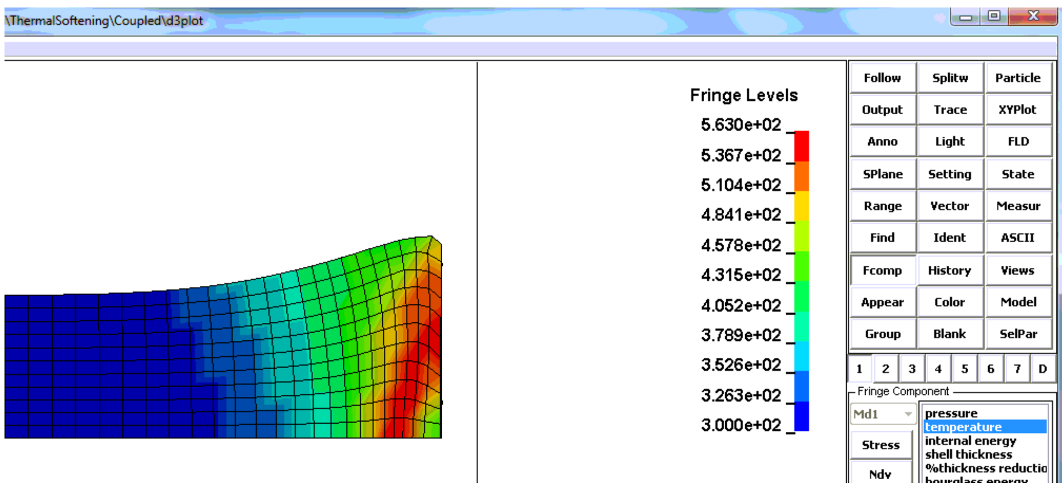

The plastic strain results are similar to the structural analysis (c). The temperature ranges are also the same (see plot in run (b) from above). The small differences are due to the thermal conductivity being considered by the coupled analysis.

f. Coupled analysis with initial temperature of 600K. Otherwise same as run (e)

History variable #5 plot for an element

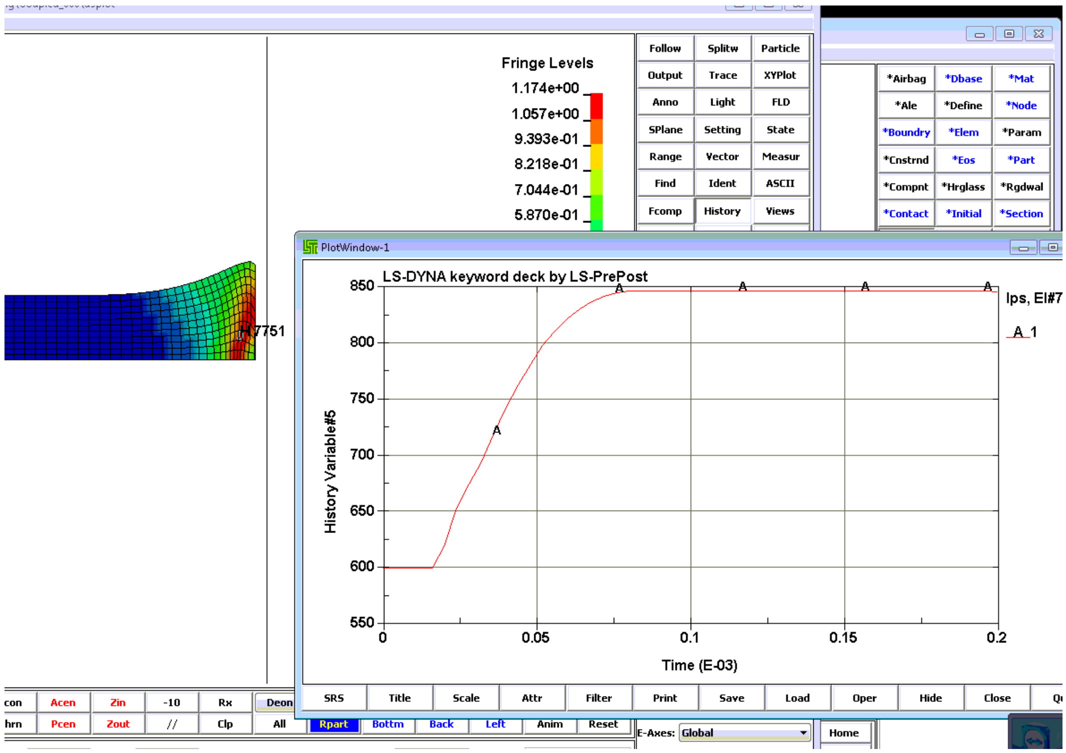

Temperature contour

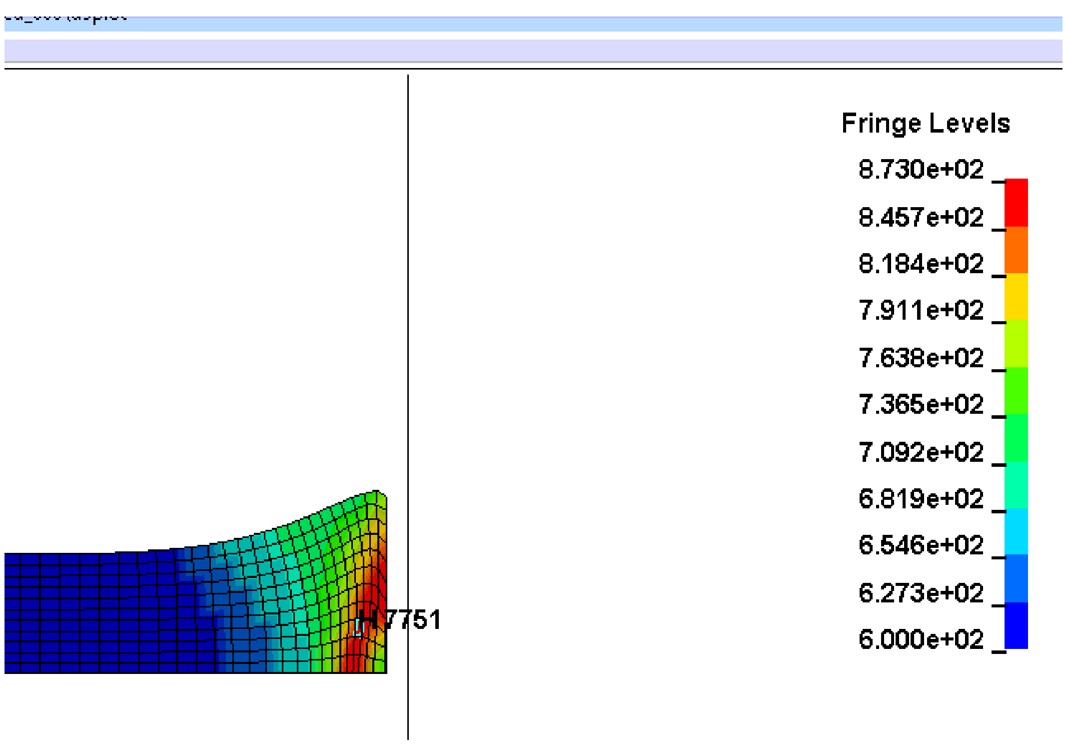

You obviously need a coupled analysis if you want to run at a higher temp than T_{ref}.

A.3.4 Conclusion

In a structural analysis, the elements' temperatures are updated in the J-C algorithm at each time increment using the following equation:

$$T_{\text{inst}} - T_{\text{ref}} = \frac{0.9W_p}{\rho C_p}$$

The instantaneous temperature is then plugged in the J-C equation to determine material softening. Time history of elements' temperature is also stored in the history variable #5 of J-C material model. An initial temperature equal to T_{ref} is assumed.

If simulating a problem at a different initial temperature is required, a coupled-thermal analysis should be run.

References

[1] I. Hutchings and R. Winter, "Particle erosion of ductile metals: a mechanism of material removal," *Wear*, vol. 27, no. 1, pp. 121–128, 1974.
[2] W. Tabakoff and M. Metwally, "Coating effect on particle trajectories and turbine blade erosion," *Journal of Engineering for Gas Turbines and Power*, vol. 114, p. 250, 1992.
[3] B. S. McLaury, J. Wang, S. A. Shirazi, J. R. Shadley, and E. F. Rybicki, "Solid particle erosion in long radius elbows and straight pipes," *Proceedings - SPE Annual Technical Conference and Exhibition*, vol. Pi, pp. 977–986, 1997.
[4] A. Forder, M. Thew, and D. Harrison, "A numerical investigation of solid particle erosion experienced within oilfield control valves," *Wear*, vol. 216, no. 2, pp. 184–193, Apr. 1998.
[5] G. I. Parslow, D. J. Stephenson, J. E. Strutt, and S. Tetlow, "Investigation of solid particle erosion in components of complex geometry," *Wear*, vol. 233–235, pp. 737–745, Dec. 1999.
[6] X. Chen and J. W. Hutchinson, "Particle impact on metal substrates with application to foreign object damage to aircraft engines," *Journal of the Mechanics and Physics of Solids*, vol. 50, no. 12, pp. 2669–2690, Dec. 2002.
[7] X. Chen, "Foreign object damage on the leading edge of a thin blade," *Mechanics of Materials*, vol. 37, no. 4, pp. 447–457, Apr. 2005.
[8] L. Dai, M. Yu, and Y. Dai, "Nozzle passage aerodynamic design to reduce solid particle erosion of a supercritical steam turbine control stage," *Wear*, vol. 262, no. 1–2, pp. 104–111, Jan. 2007.
[9] A. Campos-Amezcua, A. Gallegos-Munoz, C. Alejandro Romero, Z. Mazur-Czerwiec, and R. Campos-Amezcua, "Numerical investigation of the solid particle erosion rate in a steam turbine nozzle," *Applied Thermal Engineering*, vol. 27, no. 14–15, pp. 2394–2403, Oct. 2007.
[10] J. X. Bouillard, R. W. Lyczkowski, S. Folga, D. Gidaspow, and G. F. Berry, "Hydrodynamics of erosion of heat exchanger tubes in fluidized bed combustors," *Canadian Journal of Chemical Engineering*, vol. 67, no. 2, pp. 218–229, 1989.
[11] G. Grant and W. Tabakoff, "Erosion prediction in turbomachinary resulting from environmentally solid particles," *Journal of Aircraft*, vol. 12, no. 5, pp. 471–478, 1975.
[12] A. Holmes, "Solid particle erosion: a european OEM's experience." ALSTOM Power Turbo-Systems, 2003.
[13] P. Tangestanian, M. Papini, and J. K. Spelt, "Starch media blast cleaning of artificially aged paint films," *Wear*, vol. 248, no. 1–2, pp. 128–139, Mar. 2001.
[14] A. Raykowski, M. Hader, B. Maragno, and J. K. Spelt, "Blast cleaning of gas turbine components: deposit removal and substrate deformation," *Wear*, vol. 249, no. 1–2, pp. 126–131, 2001.
[15] M. Ramulu and D. Arola, "Water jet and abrasive water jet cutting of unidirectional graphite/epoxy composite," *Composites*, vol. 24, no. 4, pp. 299–308, 1993.
[16] R. Balasubramaniam, J. Krishnan, and N. Ramakrishnan, "A study on the shape of the surface generated by abrasive jet machining," *Journal of Materials Processing Tech.*, vol. 121, no. 1, pp. 102–106, 2002.
[17] M. Wakuda, Y. Yamauchi, and S. Kanzaki, "Material response to particle impact during abrasive jet machining of alumina ceramics," *Journal of Materials Processing Tech.*, vol. 132, no. 1–3, pp. 177–183, 2003.

[18] D. S. Park, M. W. Cho, H. Lee, and W. S. Cho, "Micro-grooving of glass using micro-abrasive jet machining," *Journal of Materials Processing Tech.*, vol. 146, no. 2, pp. 234–240, 2004.
[19] H. Getu, A. Ghobeity, J. K. Spelt, and M. Papini, "Abrasive jet micromachining of acrylic and polycarbonate polymers at oblique angles of attack," *Wear*, vol. 265, no. 5–6, pp. 888–901, 2008.
[20] D. E. Alman, J. H. Tylczak, J. A. Hawk, and M. G. Hebsur, "Solid particle erosion behavior of an Si3N4-MoSi2 composite at room and elevated temperatures," *Materials Science and Engineering A*, vol. 261, no. 1–2, pp. 245–251, 1999.
[21] Y. I. Oka and K. Nagahashi, "Measurements of plastic strain around indentations caused by the impact of round and angular particles, and the origin of erosion," *Wear*, vol. 254, no. 12, pp. 1267–1275, 2003.
[22] H. M. Hawthorne, Y. Xie, and S. K. Yick, "A study of single particle–target surface interactions along a specimen in the Coriolis slurry erosion tester," *Wear*, vol. 253, no. 3–4, pp. 403–410, 2002.
[23] G. Sundararajan, "A comprehensive model for the solid particle erosion of ductile materials," *Wear*, vol. 149, no. 1–2, pp. 111–127, 1991.
[24] M. Takaffoli and M. Papini, "Finite element analysis of single impacts of angular particles on ductile targets," *Wear*, vol. 267, no. 1–4, pp. 144–151, Jun. 2009.
[25] I. Hutchings, "Deformation of metal surfaces by the oblique impact of square plates," *International Journal of Mechanical Sciences*, vol. 19, pp. 45–52, 1977.
[26] M. Papini and S. Dhar, "Experimental verification of a model of erosion due to the impact of rigid single angular particles on fully plastic targets," *International Journal of Mechanical Sciences*, vol. 48, no. 5, pp. 469–482, 2006.
[27] I. Finnie, "Erosion of surfaces by solid particles," *Wear*, vol. 3, no. 2, pp. 87–103, 1960.
[28] M. Papini and J. K. Spelt, "Impact of rigid angular particles with fully-plastic targets Part I: Analysis," *International Journal of Mechanical Sciences*, vol. 42, no. 5, pp. 991–1006, May 2000.
[29] M. Papini and J. K. Spelt, "Impact of rigid angular particles with fully-plastic targets Part II: Parametric study of erosion phenomena," *International Journal of Mechanical Sciences*, vol. 42, no. 5, pp. 1007–1025, May 2000.
[30] S. Dhar, T. Krajac, D. Ciampini, and M. Papini, "Erosion mechanisms due to impact of single angular particles," *Wear*, vol. 258, no. 1–4, pp. 567–579, 2005.
[31] A. V. Levy, "Platelet mechanism of erosion of ductile metals," *Wear*, vol. 108, pp. 1–21, 1986.
[32] B. L. Boyce, X. Chen, J. W. Hutchinson, and R. O. Ritchie, "The residual stress state due to a spherical hard-body impact," *Mechanics of Materials*, vol. 33, no. 8, pp. 441–454, Aug. 2001.
[33] C.-Y. Wu, L.-Y. Li, and C. Thornton, "Energy dissipation during normal impact of elastic and elastic-plastic spheres," *International Journal of Impact Engineering*, vol. 32, no. 1–4, pp. 593–604, Dec. 2005.
[34] M. Junkar, B. Jurisevic, M. Fajdiga, and M. Grah, "Finite element analysis of single-particle impact in abrasive water jet machining," *International Journal of Impact Engineering*, vol. 32, no. 7, pp. 1095–1112, Jul. 2006.
[35] G. L. Sheldon and A. Kanhere, "An investigation of impingement erosion using single particles," *Wear*, vol. 21, no. 1, pp. 195–209, Aug. 1972.

[36] I. M. Hutchings, “A model for the erosion of metals by spherical particles at normal incidence,” *Wear*, vol. 70, no. 3, pp. 269–81, 1981.
[37] G. Sundararajan, “Analysis of the localization of deformation and weight loss during single-particle normal impact,” *Wear*, vol. 84, pp. 217–35, 1983.
[38] J. G. A. Bitter, “A study of erosion phenomena : Part II,” *Wear*, vol. 6, no. 3, pp. 169–190, 1963.
[39] R. Brown, S. Kosco, and E. J. Jun, “The effect of particle shape and size on erosion of aluminum alloy 1100 at 90° impact angles,” *Wear*, vol. 88, no. 2, pp. 181–93, Jul. 1983.
[40] Y. I. Oka, K. Okamura, and T. Yoshida, “Practical estimation of erosion damage caused by solid particle impact: Part 1: Effects of impact parameters on a predictive equation,” *Wear*, vol. 259, no. 1–6, pp. 95–101, 2005.
[41] T. Deng, M. S. Bingley, and M. S. A. Bradley, “The influence of particle rotation on the solid particle erosion rate of metals,” *Wear*, vol. 256, no. 11–12, pp. 1037–1049, Jun. 2004.
[42] M. Liebhard and A. Levy, “The effect of erodent particle characteristics on the erosion of metals,” *Wear*, vol. 151, no. 2, pp. 381–390, Dec. 1991.
[43] M. Roy, Y. Tirupataiah, and G. Sundararajan, “Effect of particle shape on the erosion of Cu and its alloys,” *Materials Science and Engineering: A*, vol. 165, no. 1, pp. 51–63, Jun. 1993.
[44] G. R. Desale, B. K. Gandhi, and S. C. Jain, “Effect of erodent properties on erosion wear of ductile type materials,” *Wear*, vol. 261, no. 7–8, pp. 914–921, 2006.
[45] C. L. Lin and J. D. Miller, “3D characterization and analysis of particle shape using X-ray microtomography (XMT),” *Powder Technology*, vol. 154, no. 1, pp. 61–9, Jun. 2005.
[46] D. V. De Pellegrin and G. W. Stachowiak, “Simulation of three-dimensional abrasive particles,” *Wear*, vol. 258, pp. 208–216, 2005.
[47] D. Aquaro, “Erosion due to the impact of solid particles of materials resistant at high temperature,” *Meccanica*, vol. 41, no. 5, pp. 539–551, 2006.
[48] J. G. A. Bitter, “A study of erosion phenomena, Part I,” *Wear*, vol. 6, no. 1, pp. 5–21, 1963.
[49] Y.-F. Wang and Z.-G. Yang, “A coupled finite element and meshfree analysis of erosive wear,” *Tribology International*, vol. 42, no. 2, pp. 373–377, Feb. 2009.
[50] M. S. ElTobgy, E. Ng, and M. A. Elbestawi, “Finite element modeling of erosive wear,” *International Journal of Machine Tools and Manufacture*, vol. 45, no. 11, pp. 1337–1346, Sep. 2005.
[51] J. Neilson and A. Gilchrist, “Erosion by a stream of solid particles,” *Wear*, vol. 11, no. 2, pp. 111–122, 1968.
[52] R. E. Winter and I. M. Hutchings, “Role of Adiabatic Shear in Solid-Particle Erosion,” *Wear*, vol. 34, no. 2, pp. 141–148, 1975.
[53] T. Christman and P. G. Shewmon, “Erosion of a strong aluminum alloy,” *Wear*, vol. 52, no. 1, pp. 57–70, Jan. 1979.
[54] P. J. Woytowitz and R. H. Richman, “Modeling of damage from multiple impacts by spherical particles,” *Wear*, vol. 233–235, pp. 120–133, Dec. 1999.
[55] Y.-F. Wang and Z.-G. Yang, “Finite element model of erosive wear on ductile and brittle materials,” *Wear*, vol. 265, no. 5–6, pp. 871–878, Aug. 2008.
[56] S. Yerramareddy and S. Bahadur, “Effect of operational variables, microstructure and mechanical properties on the erosion of Ti-6Al-4V,” *Wear*, vol. 142, no. 2, pp. 253–263, 1991.

[57] Y. B. Guo and D. W. Yen, “A FEM study on mechanisms of discontinuous chip formation in hard machining,” *Journal of Materials Processing Technology*, vol. 155–156, pp. 1350–6, Nov. 2004.
[58] A. Raczy, M. Elmadagli, W. J. Altenhof, and A. T. Alpas, “An Eulerian finite-element model for determination of deformation state of a copper subjected to orthogonal cutting,” *Metallurgical and Materials Transactions A: Physical Metallurgy and Materials Science*, vol. 35 A, no. 8, pp. 2393–2400, 2004.
[59] S. S. Akarca, X. Song, W. J. Altenhof, and A. T. Alpas, “Deformation behaviour of aluminium during machining: modelling by Eulerian and smoothed-particle hydrodynamics methods,” *Proceedings of the Institution of Mechanical Engineers, Part L: Journal of Materials: Design and Applications*, vol. 222, no. 3, pp. 209–221, 2008.
[60] J. Limido, C. Espinosa, M. Salaun, and J. L. Lacome, “SPH method applied to high speed cutting modelling,” *International Journal of Mechanical Sciences*, vol. 49, no. 7, pp. 898–908, Sep. 2007.
[61] M. Heinstein and D. Segalman, “Simulation of orthogonal cutting with smooth particle hydrodynamics,” *Sandia National Laboratories, California*, 1997.
[62] R. E. Winter and I. M. Hutchings, “Solid particle erosion studies using single angular particles,” *Wear*, vol. 29, no. 2, pp. 181–194, Aug. 1974.
[63] T. Christman and P. Shewmon, “Adiabatic shear localization and erosion of strong aluminum alloys,” *Wear*, vol. 54, pp. 145–155, 1979.
[64] A. Levy, *Solid particle erosion and erosion-corrosion of materials*. ASM International, 1995.
[65] I. M. Hutchings, M. C. Rochester, and J. J. Camus, “A rectangular-bore gas gun,” *Journal of Physics E: Scientific Instruments*, vol. 10, pp. 455–457, 1977.
[66] J. A. Zukas and D. R. Scheffler, “Practical aspects of numerical simulations of dynamic events: Effects of meshing,” *International Journal of Impact Engineering*, vol. 24, no. 9, pp. 925–945, 2000.
[67] G. R. Johnson and W. H. Cook, “A constitutive model and data for metals subjected to large strains, high strain rates and high temperatures,” in *Proceedings of the 7th International Symposium on Ballistics*, 1983, pp. 541–547.
[68] G. R. Johnson and W. H. Cook, “Fracture characteristics of three metals subjected to various strains, strain rates, temperatures and pressures,” *Engineering Fracture Mechanics*, vol. 21, no. 1, pp. 31–48, 1985.
[69] R. Kouddane, N. Zouhal, A. Molinari, and G. R. Canova, “Complex loading of viscoplastic materials: micro-macro modelling,” *Materials Science and Engineering A*, vol. A175, no. 1–2, pp. 31–36, 1994.
[70] T. Borvik, O. S. Hopperstad, T. Berstad, and M. Langseth, “Perforation of 12mm thick steel plates by 20mm diameter projectiles with flat, hemispherical and conical noses - Part II: Numerical simulations,” *International Journal of Impact Engineering*, vol. 27, no. 1, pp. 37–64, 2002.
[71] R. Porcaro, A. G. Hanssen, M. Langseth, and A. Aalberg, “Self-piercing riveting process: An experimental and numerical investigation,” *Journal of Materials Processing Technology*, vol. 171, no. 1, pp. 10–20, Jan. 2006.
[72] M. A. Meyers, *Dynamic Behavior of Materials*. Wiley-Interscience, 1994.

[73] M. Takaffoli and M. Papini, “Material deformation and removal due to single particle impacts on ductile materials using smoothed particle hydrodynamics,” *Wear*, vol. 274–275, pp. 50–59, 2012.

[74] L. B. Lucy, “A numerical approach to the testing of the fission hypothesis,” *The Astronomical Journal*, vol. 82, no. 12, pp. 1013–1024, 1977.

[75] R. A. Gingold and J. J. Monaghan, “Smoothed particle hydrodynamics- Theory and application to non-spherical stars,” *Royal Astronomical Society, Monthly Notices*, vol. 181, pp. 375–389, 1977.

[76] S. Li and W. K. Liu, “Meshfree and particle methods and their applications,” *Applied Mechanics Reviews*, vol. 55, no. 1, pp. 1–34, 2002.

[77] G. R. Liu and M. B. Liu, *Smoothed Particle Hydrodynamics: A Meshfree Particle Method*. World Scientific, 2003.

[78] D. J. . Lacome, “Smoothed particle hydrodynamics,” *Livermore Software Technology Corporation, Livermore, CA*, 2001.

[79] C. Espinosa, J. L. Lacome, J. Limido, M. Salaun, R. Mabru, and R. Chieragatti, “Modeling high speed machining with the SPH method,” presented at the 10th international LS-DYNA users conference, Dearborn, Michigan USA, 2008.

[80] P. W. Randles and L. D. Libersky, “Smoothed particle hydrodynamics: some recent improvements and applications,” *Computer Methods in Applied Mechanics and Engineering*, vol. 139, no. 1–4, pp. 375–408, 1996.

[81] J. P. Vila, “SPH renormalized hybrid methods for conservation laws: Application to free surface flows,” *Lecture notes in Computational Science and Engineering*, vol. 43, pp. 207–229.

[82] J. J. Monaghan, “SPH without a tensile instability,” *Journal of Computational Physics*, vol. 159, no. 2, pp. 290–311, Apr. 2000.

[83] T. Belytschko and Shaoping Xiao, “Stability analysis of particle methods with corrected derivatives,” *Computers & Mathematics with Applications*, vol. 43, no. 3–5, pp. 329–50, Feb. 2002.

[84] B. M. Corbett, “Numerical simulations of target hole diameters for hypervelocity impacts into elevated and room temperature bumpers,” *International Journal of Impact Engineering*, vol. 33, no. 1–12, pp. 431–440, 2006.

[85] A. Majumder, W. Altenhof, V. Vijayan, and S. Y. Jin, “Quasi-static axial cutting of AA6061 T4 and T6 round extrusions,” *Proceedings of the Institution of Mechanical Engineers, Part L (Journal of Materials: Design and Applications)*, vol. 222, no. L3, pp. 183–95, Jul. 2008.

[86] L. E. Schwer, K. Hacker, and K. Poe, “Perforation of metal plates: laboratory experiments and numerical simulations,” presented at the 9th international LS-DYNA users conference, Dearborn, Michigan, USA, 2006.

[87] H. Bil, S. E. Kılıç, and A. E. Tekkaya, “A comparison of orthogonal cutting data from experiments with three different finite element models,” *International Journal of Machine Tools and Manufacture*, vol. 44, no. 9, pp. 933–944, 2004.

[88] I. M. Hutchings, “Strain rate effects in microparticle impact,” *J. Phys. D: Appl. Phys*, vol. 10, 1977.

[89] I. M. Hutchings, “Prediction of the resistance of metals to erosion by solid particles,” *Wear*, vol. 35, no. 2, pp. 371–374, 1975.

[90] G. Ravichandran, A. J. Rosakis, J. Hodowany, and P. Rosakis, "On the conversion of plastic work into heat during high-strain-rate deformation," *AIP Conference Proceedings*, no. 620, pp. 557–62, 2002.
[91] G. E. Dieter, *Mechanical Metallurgy*. McGraw-Hill, 1986.
[92] W. Dabboussi and J. A. Nemes, "Modeling of ductile fracture using the dynamic punch test," *International Journal of Mechanical Sciences*, vol. 47, no. 8, pp. 1282–1299, 2005.
[93] J. O. Hallquist, "LS-DYNA. Keyword User's Manual. Version 971," *Livermore Software Technology Corporation,* 2007.
[94] W. K. Rule, "A numerical scheme for extracting strength model coefficients from Taylor test data," *International Journal of Impact Engineering*, vol. 19, no. 9–10, pp. 797–810, 1997.
[95] D. R. Lesuer, G. J. Kay, and M. M. LeBlanc, "Modeling large strain, high rate deformation in metals," in *Modelling the Performance of Engineering Structural Materials II. Proceedings of a Symposium, 4-8 Nov. 2001*, Warrendale, PA, USA, 2001, pp. 75–86.
[96] N. Jones, "Some remarks on the strain-rate sensitive behavior of shells," *Problems of plasticity.(A 75-13527 03-39) Leiden, Noordhoff International Publishing, 1974,*, pp. 403–407, 1974.
[97] G. R. Cowper and P. S. Symonds, "Strain hardening and strain rate effects in the impact loading of cantilever beams," *Brown University Division of Applied Mathematics Report*, vol. 28, 1957.
[98] J. R. Keiser, R. S. Heidersbach, D. L. Dobbs, and W. C. Oliver, "Characteristics of individual impact craters on selected aluminum alloys," *Wear*, vol. 124, no. 1, pp. 105–18, May 1988.
[99] Y. I. Oka, M. Matsumura, and H. Funaki, "Measurements of plastic strain below an indentation and piling-up between two adjacent indentations," *Wear*, vol. 186–187, no. 1, pp. 50–55, 1995.
[100] Y. I. Oka, H. Ohnogi, T. Hosokawa, and M. Matsumura, "The impact angle dependence of erosion damage caused by solid particle impact," *Wear*, vol. 203–204, pp. 573–579, Mar. 1997.
[101] M. F. Da Silva, K. Shimizu, K. Kobayashi, P. Skeldon, G. E. Thompson, and G. C. Wood, "On the nature of the mechanically polished aluminum surface," *Corrosion Science*, vol. 37, no. 9, pp. 1511–14, Sep. 1995.
[102] D. Dehnadfar, J. Friedman, and M. Papini, "Laser shadowgraphy measurements of abrasive particle spatial, size and velocity distributions through micro-masks used in abrasive jet micro-machining," *Journal of Materials Processing Technology*, vol. 212, no. 1, pp. 137–149, 2012.
[103] L. E. Murr, A. Ayala, and C. S. Niou, "Microbands and shear-related microstructural phenomena associated with impact craters in 6061-T6 aluminum," *Materials Science & Engineering A (Structural Materials: Properties, Microstructure and Processing)*, vol. A216, no. 1–2, pp. 69–79, Oct. 1996.
[104] R. Bellman Jr. and A. Levy, "Erosion mechanism in ductile metals," *Wear*, vol. 70, no. 1, pp. 1–27, 1981.
[105] P. Shewmon and G. Sundararajan, "The Erosion of Metals," *Annual Reviews in Materials Science*, vol. 13, no. 1, pp. 301–318, 1983.

[106] B.-M. Kim, C.-J. Lee, and J.-M. Lee, "Estimations of work hardening exponents of engineering metals using residual indentation profiles of nano-indentation," *Journal of Mechanical Science and Technology*, vol. 24, no. 1, pp. 73–76, 2010.
[107] D. G. Rickerby and H. H. Macmillan, "The erosion of aluminum by solid particle impingement at normal incidence," *Wear*, vol. 60, no. 2, pp. 369–382, 1980.
[108] I. Finnie and Y. H. Kabil, "On the formation of surface ripples during erosion," *Wear*, vol. 8, no. 1, pp. 60–69, January.
[109] R. Brown, J. Jun, and J. W. Edington, "Erosion of -Fe by spherical glass particles," *Wear*, vol. 70, no. 3, pp. 347–63, 1981.
[110] Y. A. Ballout, J. A. Mathis, and J. E. Talia, "Effect of particle tangential velocity on erosion ripple formation," *Wear*, vol. 184, no. 1, pp. 17–21, Apr. 1995.
[111] D. R. Andrews, "An analysis of solid particle erosion mechanisms," *Journal of Physics D (Applied Physics)*, vol. 14, no. 11, pp. 1979–91, Nov. 1981.
[112] A. K. Cousens and I. M. Hutchings, "A critical study of the erosion of an aluminum alloy by solid spherical particles at normal impingement," *Wear*, vol. 88, no. 3, pp. 335–48, Jul. 1983.
[113] R. Brown, E.-J. Jun, and J. W. Edington, "Mechanisms of solid particle erosive wear for 90 impact on copper and iron," *Wear*, vol. 74, no. 1, pp. 143–56, Dec. 1981.
[114] R. Brown and J. W. Edington, "Erosion of copper single crystals under conditions of 90 impact," *Wear*, vol. 69, no. 3, pp. 369–82, Jul. 1981.
[115] W. H. Jennings, W. J. Head, and C. R. Manning Jr., "Mechanistic model for the prediction of ductile erosion," *Wear*, vol. 40, no. 1, pp. 93–112, 1976.
[116] M. Takaffoli and M. Papini, "Numerical simulation of solid particle impacts on Al6061-T6 part I: three dimensional representation of angular solid particles," *Under review*.
[117] G. R. Johnson and T. J. Holmquist, "Response of boron carbide subjected to large strains, high strain rates, and high pressures," *Journal of Applied Physics*, vol. 85, no. 12, p. 8060, 1999.
[118] A. Manes, L. Peroni, M. Scapin, and M. Giglio, "Analysis of strain rate behavior of an Al 6061 T6 alloy," in *11th International Conference on the Mechanical Behavior of Materials, ICM11, June 5, 2011 - June 9, 2011*, Como, Italy, 2011, vol. 10, pp. 3477–3482.
[119] A. Shrot, "Determination of Johnson–Cook parameters from machining simulations," *Computational Materials Science*, vol. 52, no. 1, pp. 298–304, Feb. 2012.
[120] S. Srinivasan, "Effect of erodent hardness on erosion of brittle materials," *Wear*, vol. 128, no. 2, pp. 139–152, Dec. 1988.
[121] B. J. Griffiths, "The erosion of steel surfaces by grit-blasting as a preparation for plasma spraying," *Wear*, vol. 194, no. 1–2, pp. 95–102.
[122] E. Uhlmann and A. El Mernissi, "Pre-treatment by dry ice blasting for adhesive bonding," *Production Engineering*, vol. 2, no. 2, pp. 133–138, Apr. 2008.
[123] M. Scapin, L. Peroni, and M. Peroni, "Parameters identification in strain-rate and thermal sensitive visco-plastic material model for an alumina dispersion strengthened copper," vol. 40–41, no. 1, pp. 58–67, 2011.
[124] S. Dey, T. Borvik, X. Teng, T. Wierzbicki, and O. S. Hopperstad, "On the ballistic resistance of double-layered steel plates: an experimental and numerical investigation," *International Journal of Solids and Structures*, vol. 44, no. 20, pp. 6701–23, Oct. 2007.